Formation and Neutralization of Some Reactive Components Relevant to Bayer Alumina Production and Their Application as Adsorbents

Ph.D. dissertation

Eszter Kása

Supervisor:

Prof. Pál Sipos

Consultants:

Dr. Márton Szabados

Dr. Bence Kutus

Doctoral School of Chemistry

Department of Molecular and Analytical Chemistry,

Faculty of Science and Informatics, University of Szeged

Szeged

2025

1. TABLE OF CONTENTS

2. INTRODUCTION

The Bayer process (presented in **Fig. 1**) is the leading industrial method of producing alumina (Al_2O_3) from bauxite ore. It was invented in 1887 and patented in 1894 by Karl Joseph Bayer [1]. It is based on the dissolution of alumina compounds in hot caustic liquor, and their recrystallization in the presence of different inorganic (NaCl, Na_2CO_3, Na_2SO_4, $Ca(OH)_2$) and organic (humic acid, sodium oxalate, carboxylates, polyacrylates and polyacrylamides) reagents [2-6]. To reduce the amount of impurities, present in the bauxite ore, several techniques were introduced to improve the efficiency of the Bayer process. For instance, the presence of kaolinite can cause significant caustic loss and scaling in the heat exchangers, therefore, when the silica content of the bauxite is above 2% a pre-desilication step is introduced before the digestion to reduce the quantity of the kaolinite, and to eliminate it from the further technological process [7].

Although, it is the economically best practice in the alumina industry even nowadays, there are several environmental problems caused by the Bayer process. The greatest challenges are connected to the bauxite residue, or red mud. This is a highly alkaline and mineralogically complex by-product with wide particle size distribution, and varying chemical and physical characteristics, depending on the processing conditions and bauxite source. Bauxite residue (BxR) mainly consists of goethite, hematite, sodalite, silica, tricalcium aluminate hexahydrate, titanium dioxide, and calcite. In addition, there can be various metals found in BxR at trace levels, like gallium, manganese, lead, uranium, and thorium.

Most bauxite residue is maintained in long-term storage facilities (BRDA in **Fig. 1**) using the so-called dry method. Instead of this solution, the industry needs a permanent waste management, utilization, and remediation plan, considering that globally more than 150 Mt bauxite residue is generated annually [8]. To establish a working plan for bauxite residue management it is necessary to think outside the box, to understand, as Alexander von Humboldt believed, the “astounding interconnectedness of the universe” [9], and to consider this technological process not in isolation, but as a chain of causes and effects.

In the present work, the above-mentioned problems were approached from two different directions. First of all, my priority was to minimalize the bauxite residue quantity by reducing the amount of the sodalite in the red mud. To control the solubility and re-crystallization during the pre-desilication step, I focused on the understanding of which characteristics influence the processes and how. On the other hand, the reusability of the by-products had an equally crucial

part of my work. First, the product of the pre-desilication process, sodalite that was used successfully as cationic dye adsorbent, even under simulated industrial conditions. Second, the neutralization mechanism of tricalcium aluminate hexahydrate, one of the most alkaline solids in the bauxite residue, was investigated in detail with hydrochloric acid. This experimental work is the first step to a comprehensive neutralization plan for any bauxite residue produced by the alumina industry.

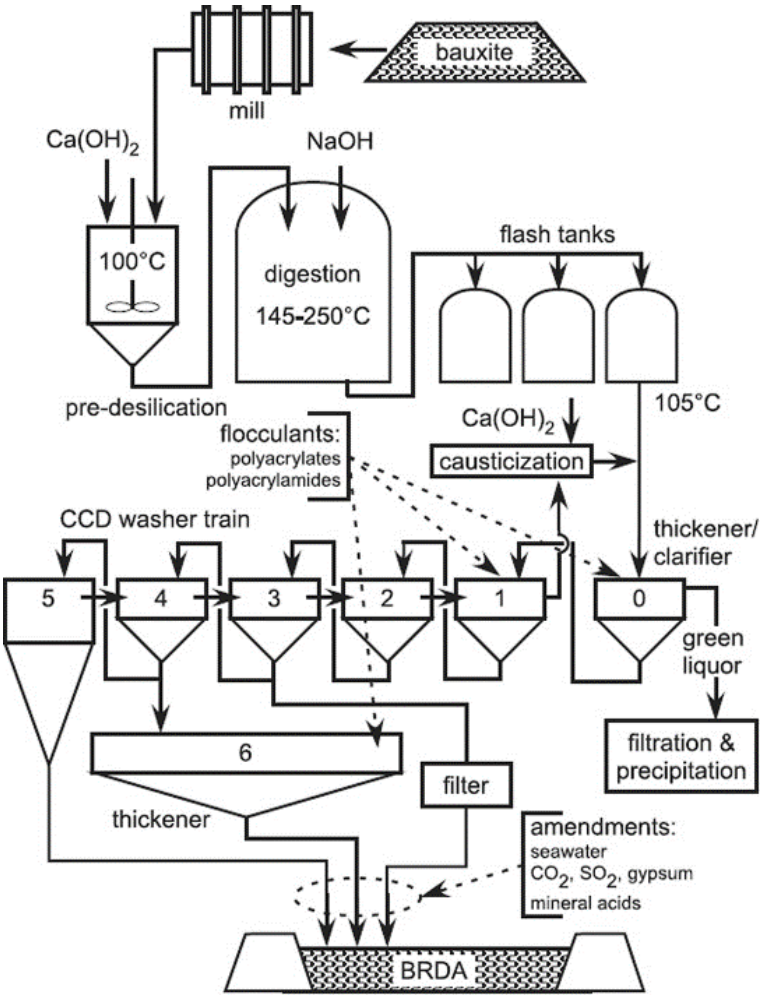

Fig. 1 The most important steps of the Bayer process [10].

3. LITERATURE REVIEW

3.1 Processes during the pre-desilication step

During the pre-desilication step the reactive silica reacts with the recirculated sodium aluminate solution (known as spent liquor in the industry), and the so-called desilication product (DSP) forms, a mix of different solids. The main component of this product is the sodalite, a sodium aluminium silicate hydrate with various anions in its cages.

3.1.1 Kaolinite, the reactive silica source

Kaolinite ($Al_2Si_2O_5(OH)_4$) is a crystalline hydrated aluminium silicate formed during the hydrothermal decomposition of granite rocks, generally in warm, moist climates. This clay mineral consists of tetrahedral silica sheets coordinated to octahedral alumina sheets through oxygen atoms (**Fig. 2**). Each particle consists of about 50 sheets of the above-mentioned twin layers coordinated through hydrogen bonds; however, poorly crystalline kaolinite can have irregular and jagged edges, and the particles appear smaller and thinner than the well-crystallized, hexagonal particles. The crystallinity and other physico-chemical characteristics of the kaolinites are strongly influenced by the properties of the soil during the kaolinization of the bauxite [11-13].

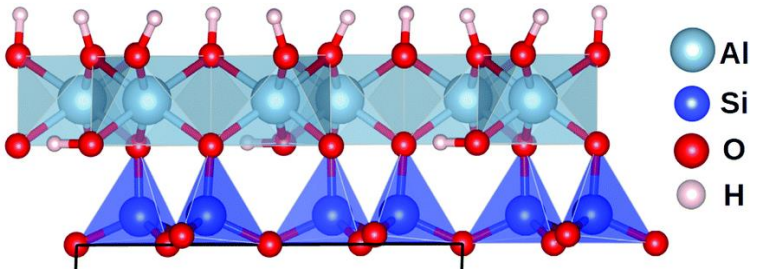

Fig. 2 The structure of one kaolinite layer: one silica sheet coordinated to one alumina sheet, published by Weck et al. [14].

Kaolinite is also an impurity in the bauxite, as one of the main silica sources. While quartz is also known as free or inert silica, kaolinite is called as reactive silica in the alumina industry, because it reacts with the caustic liquor during the digestion step. It can cause scale-up in the heat exchangers, consequently, pressure drop and flow restrictions. Moreover, each tonne of reactive silica consumes approximately 1.18 tonnes of sodium aluminate solution, resulting in valuable loss of alumina and caustic soda. The extent of this unrecoverable loss depends on the silica content of the bauxite. Accordingly, the usage of high-grade bauxite is

necessary, while the so-called marginal bauxites with high reactive silica content (≥ 7 m/m%) are not used for alumina production [15, 16].

To reduce the silica content of the bauxite prior to digestion, several methods are used in the industry. For instance, when kaolinite is present as a fine, discrete phase in the bauxite, crushing and washing out the impurity can effectively reduce its quantity to 50%. On the other hand, the massive, well-crystallized clay minerals cannot be removed by washing, the bauxite is firstly ground for the efficient separation. Although both solutions are sufficiently successful, these techniques need significant extra energy. Fortunately, the drawbacks of the high reactive silica content can also be decreased by modifying the digestion conditions, for instance, by using lower temperature, or shorter digestion time, hence, by introducing the so-called pre-desilication step [17].

3.1.2 Kaolinite dissolution and sodalite formation

During the pre-desilication step, two concurrent processes take place: (1) the dissolution of the kaolinite and (2) the formation of the desilication product [18, 19]. Although DSP is a mix of different solids (cancrinite, zeolite Linde Type A, amorphous aluminate silicate) formed during this process, sodalite is the predominant phase at low temperatures (< 150°C) in the alumina refineries with moderate reaction time [20].

Dissolution:

$$Al_2O_3 \cdot 2SiO_2 \cdot 2H_2O_{(s)} + 6NaOH_{(aq)} + H_2O_{(l)} \leftrightarrow$$

$$\leftrightarrow 2H_2SiO_4^{2-}{}_{(aq)} + 2Al(OH)_4^-{}_{(aq)} + 6Na^+{}_{(aq)} \quad (1)$$

Precipitation:

$$6H_2SiO_4^{2-}{}_{(aq)} + 6Al(OH)_4^-{}_{(aq)} + 6Na^+{}_{(aq)} + 6Na_2X_{(aq)} \leftrightarrow$$

$$\leftrightarrow Na_8(AlSiO_4)_6 \cdot X \cdot yH_2O_{(s)} + (12\text{-}y)H_2O_{(l)} + 12OH^-{}_{(aq)} \quad (2)$$

In equation (2) sodalite (SOD) is precipitated with various anions in the aluminosilicate framework (shown in **Fig. 3**), which may be CO_3^{2-}, SO_4^{2-}, $2OH^-$, $2Al(OH)_4^-$ from the liquor, denoted by X. The removal of these inorganic impurities has a beneficial effect on the purity of the Bayer liquor, therefore on the yield of the whole process [21]. Water molecules can also be present (y may range from 0 to 4) in the hydrated structure.

Next to the inorganic impurities, organic chemical compounds are also present in the Bayer process, from the bauxite source or as flocculants and antifoams added during the process. It is generally believed that the organic matter in bauxite comes from the lignitic clays, mostly in form of humic acids, humates and their oxidation products [22] They may stem from the decomposition products of the vegetation and roots, for example, humus, lignin, cellulose, and protein break down to sodium salts of succinic, oxalic, and acetic acids and carbon dioxide [23]. Based on the literature, these impurities can have different effects on the extraction in the recycled caustic liquor. For instance, although the organic compounds soluble in benzene seem to reduce the rate of dissolution, others, with hydroxyl radicals can promote it [24, 25]. Because of the many factors influencing the dissolution of the bauxite and the precipitation of the products, it is extremely difficult to study the whole processes under industrial conditions and to have a straightforward conclusion regarding all the influencing factors, valid for all real-life scenarios.

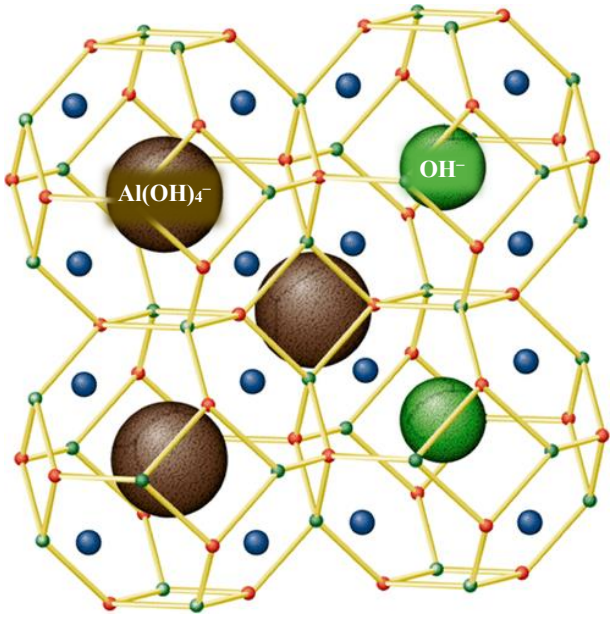

Fig. 3 Structure of sodalite (SOD) cages with various incorporated ions shown in ball-stick format, without oxygen atoms (where little red and green balls represent the aluminium and silicon atoms in the framework, while blue balls symbolize the metal, usually sodium, cations present in the β-cages) [26].

Sodalite is composed of alternating Si–O–Si and Si–O–Al units, constructed from edge-connected $[SiO_4]^{4-}$ and $[AlO_4]^{5-}$ tetrahedra. The formed framework, with all the cages and channels, has well-defined ≈ 2.3 Å diameter cage openings or windows. Not only the above-mentioned anions can clathrate into the β–cages formed from the 6- and 4-membered rings, but

also the charge-balancing metal cations (the four negative charges are usually neutralized through four sodium ions) [19, 27].

3.1.3 Treatment of the kaolinite prior dissolution

There are many chemical and physical methods to facilitate the dissolution of the kaolinite in aqueous solutions [28-31], but in this work we only discuss in detail two methods, namely, the mechanochemical activation and the calcination.

3.1.3.1 Mechanochemical activation

Mechanochemical activation is a process which increases the reaction ability of materials by using mechanical energy to change the different physico-chemical properties of solids [32]. The main effects of the mechanochemical treatment, including wet and dry ball milling, are particle size reduction, increase of specific surface area, modified particle morphology, creating defects in the crystal structure, and thus, increasing the rate of dissolution and the solubility [33, 34]. Based on the work of Baki et al. [35], during dry grinding, first, the crystallinity of the kaolin decreases, and the specific surface area increases, then, a complete delamination occurs through the dehydroxylation. The specific surface area, after reaching a maximum, decreases at further mechanochemical treatment. Makó et al. [36] also studied the results of dry grinding on the physico-chemical characteristics of the kaolinite. The authors reported that the amorphization can be connected to the breakage of the O–H, Si–O, Al–O–Si and Al–OH bonds in the solid, resulting in a water-containing xerogel with random structure. Moreover, there is no detectable intermediate phase during the milling process, the disordered kaolinite phase probably coexists with the relatively unaffected kaolinite phase. The effectiveness of the mechanochemical amorphization and the property of the product seems to be dependent on the crystallinity of the original clay [33, 36].

3.1.3.2 Calcination

Calcination is a heat treatment process used to change some of the physico-chemical properties of the substances by exposing the material to high temperature in controlled environment. During thermal treatment, the solid usually releases volatile compounds (water or other impurities) resulting phase transition, volume shrinkage, and thermal decomposition. The effect of thermal treatment on kaolinite can be described by four consecutive stages. First, the removal of physisorbed water below 450°C, without any structural change, next, the progressive

dehydration of the solid in the temperature range of 500-850°C, when, due to the crystal structure collapse caused by water loss, kaolinite transforms into a highly disordered phase, namely metakaolinite ($Al_2O_3 \cdot 2SiO_2$) [37]. At higher temperatures, at around 900°C, the condensed metakaolinite forms Al–Si spinel ($2Al_2O_3 \cdot 3SiO_2$), probably by the removal of silica from the lattice, and finally, at around 1000°C, the mullite phase ($3Al_2O_3 \cdot 2SiO_2$) appears through further silica loss during an exothermic reaction [38, 39].

3.2 Adsorption

Adsorption in a surface phenomenon where molecules of the fluid (adsorptive) from the bulk accumulate on the surface of the adsorbent as a result of physical forces or chemical bonds, depending on the strength of the interaction. Generally, physisorption takes place when electrostatic interactions happen resulting in weak bonds that can be easily broken, for instance, dipole, van der Waals, or $\pi - \pi$ interactions. Chemisorption, on the other hand, occurs when strong covalent or electrophilic bonds form on the surface. The efficiency of these processes depends on the properties of the adsorptive and of the surface, moreover, the conditions of the environment, such as temperature, pressure, or pH. Important information can be concluded about the adsorption process at equilibrium, when the concentration of the adsorbate on the surface is in dynamic balance with its concentration in the bulk solution [40, 41].

3.2.1 The most common adsorbents

Adsorbents are usually porous solids or materials with large specific surface area. Activated carbon is probably the most prolific adsorbent owing to its versatileness, chemical and mechanical stability, extensive network of internal pores, and huge specific surface area. Since activated carbon can be produced from a variety of raw materials by different methods [42, 43], their properties also differ. For instance, their total surface area varies between 450-1800 m^2/g and pore volume from 0.7 to 1.8 ml/g [44]. Polymers are also distinguished adsorbents because of their wide surface area, exceptional mechanical properties, and adjustable physico-chemical characteristics. Their modification can lead to superior characteristics, for instance, increased number of adsorption sites, hence, improved adsorption capacity, or increased selectivity by inserting different functional groups to the polymeric chain [45].

Another popular and selective adsorbent is the zeolite, which can be regenerated and modulated easily (its properties can be adjusted to its specific application). Zeolites are highly

porous crystalline aluminosilicates, built of silica and alumina tetrahedra connected by O atoms. Various natural and synthetic zeolites are used nowadays in the industry, depending on its features determined by their silicon to aluminium ratio, size of the pore openings, or the number and nature of cations [46]. One of the most commonly used zeolites are the faujasite type (FAU), because their structure is very ventilated, its pores have large, 12-ring openings (7.4 Å), therefore, the adsorptive can approach easily the internal sites during adsorption [47]. Moreover, the thermal stability of FAU makes it not just an ideal adsorbent but also a great catalyst in wide temperature range. Lynde type A (LTA) is another well-known representative of the zeolite family, built up from α- and β-cages forming an 8-ring channel system. LTA is usually used as an ion-exchanger mainly in laundry detergents and desiccant both in the industry and in laboratories [48]. Although sodalites have limited adsorption capacities due to their framework with only 6-ring windows, there are many examples in the literature where they were used successfully as heavy metal ion adsorbents in aqueous media [49-51]. However, there were only a few studies carried out about dye adsorption properties of sodalites.

3.2.2 The adsorption of dyes

Dyes are one of the major water contaminants, released principally by the textile industry. These soluble, toxic, often carcinogenic agents not only cause aesthetic damage to the environment but also affect the whole aquatic biota by preventing the penetration of light, hence, the photosynthesis of the aquatic plants is also hindered [52]. Moreover, these textile dyes can also contain heavy metals, as chromium, cobalt, or copper, which can be assimilated by the flora and the fauna. Through the food chain, these pollutants can even accumulate in the human body causing a variety of pathologies. For instance, Basic Violet 14 is a proven carcinogenic and toxic textile dye, which can induce the appearance of skin irritations, dermatitis, local sarcomas and tumours in the mammary glands, bladder, and liver [53, 54]. Despite the indisputable toxicity of these textile dyes, they are still available on the market and present in the environment.

In order to reduce the pollution of the water bodies, many purification techniques have been studied; however, in case of textile dyes, adsorption is considered as one of the most attractive solutions, because of its versatility, simplicity, and low energy consumption. Furthermore, unlike oxidation techniques, adsorption does not cause the formation of potentially carcinogenic intermediates during the purification method [55]. On the other hand, adsorbents and their regenerations can be expensive, therefore, there are more and more studies

about waste materials used as dye adsorbents in the literature. Gupta et al. [56] demonstrated that red mud can be potentially used to remove rhodamine B, methylene blue and fast green from industrial wastewater; however, the pre-treatment (hydrogen peroxide leaching, calcination and grinding) of the adsorbent was found to be a must to obtain an optimal result. The obtained adsorbent had promising results, above 75% of the dyes were removed from the solution, and the process can be described with the Langmuir isotherm, indicating a monolayer adsorption.

Zhou et al. [57] studied another industrial waste, namely, coal gangue, as source material of ceramic adsorbent. The adsorbent is made by spray drying and sintering from the by-product of coal mining and washing and seems to be an impressive adsorbent of cationic dyes at basic pH, reaching more than 99% removal efficiency at optimal conditions. Food waste can also be used as dye adsorbent, as it is stated by Alhujaily et al. [58], who used spent mushroom waste to remove anionic dyes from aqueous media. The mushroom waste was washed with deionized water and dried at 100°C prior adsorption experiments. The process was described with the Langmuir isotherm and reached the maximum adsorption capacity at pH = 2. Fathi et al. [59] determined the adsorption capacity of corn stalks, proving that agricultural waste materials can also be efficient adsorbents. The washed, dried, and milled corn stalks proved to be a potential adsorbent of Direct Red 23 dye at pH = 3. One can see that although waste materials can be used as cost-friendly and effective adsorbents, they often need expensive pre-treatment with high energy consumption to achieve the desired outcome. Although adsorption capacities are often compared in the literature, they can be truly set side by side only if all the process conditions are the same, knowing that adsorption can be immensely influenced by even the slightest change in the temperature, initial concentrations, stirring rate, pH, etc.

3.2.3 Basic Violet 14 adsorption on different adsorbents

Basic Violet 14 (BV14), also known as basic fuchsin or magenta, is a triamino triphenyl methane dye, with the molecular structure shown in **Fig. 4**. This cationic dye has a pH of 5 in aquatic solutions and its molecular diameter is 12.4 Å [60]. It was the second aniline dye produced in the mid-nineteenth century, after mauveine, but unlike the latter, basic violet 14 is still in use not only as a dye in the textile, cosmetic and leather industries, but also in the biomedicine as staining agent for nuclei [61].

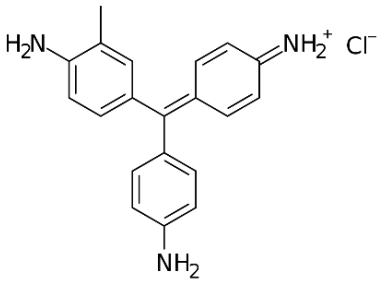

Fig. 4 Molecular structure of Basic Violet 14 ($C_{20}H_{19}N_3 \cdot HCl$) dye.

Under anaerobic conditions, Basic Violet 14 decomposes into toxic aromatic amines which can have carcinogenic and mutagenic effects and can cause serious skin irritations. Hence, adsorption seems to be the best practice to water purification, several other purification methods can result in even more toxic products. Manjula Rani et al. [62] used activated carbon from tea dust as adsorbent to remove BV14 from aqueous media. The match experiments showed great adsorption capacity at around pH 3 and the process proved to be spontaneous and endothermic. Jain et al. [63] also studied BV14 adsorption on plant residues, namely on used fenugreek. The maximum adsorption capacity was found to be 177.78 mg/g at pH 7.2 and 323 K. In order to use this vegetable waste as an adsorbent, it was washed and dried at 150°C for 30 minutes and ground into powder prior to batch experiments.

Saranya et al. [64] found out that not just biomass but some live plants, as Hydrilla verticillate, can also be used as BV14 adsorbents. Although the bioaccumulation of the dye takes up more time than the usual adsorbents, it is promising that at lower dye concentrations, the growth of the plant proved to be normal. On the other hand, its efficiency cannot be compared to the adsorption capacity of a regular adsorbent as ZSM-5 zeolite studied by Ba Mohammed et al. [65]. Under optimal conditions (pH 5 and 20°C) ZSM-5 modified with Fe can adsorb 251.87 mg/g Basic Violet 14 with 10 mg/L initial dye concentration, and the process can be described with the Langmuir isotherm in equilibrium. Elkady et al. [66] also concluded that the Langmuir isotherm can best describe the equilibrium on the surface of the functionalized co-polymer nanofiber adsorbent as adsorbing BV14 from aqueous solution. The maximum uptake was 67.11 mg/g at pH 6.2 in batch mode.

Sodalites could be considered as low-cost and efficient adsorbents of many impurities present in water bodies, not just for heavy metals but also for dye molecules such as Basic Violet 14. The cost-efficiency of this secondary raw material, however, should be judged in every case separately because it can depend on multiple factors, as application and regeneration costs and the safety assessments regarding the disposal of the spent adsorbent. On the other

hand, by using desilication product as an adsorbent we can reduce the quantity of the bauxite residue, even though, the remaining by-product can still cause serious environmental problems. Accordingly, the next chapter will focus on the main issue of this industrial waste material.

3.3 Waste management best practices of bauxite residue

Bauxite residue (BxR) is a slurry by-product generated in great quantity during the Bayer process, after leaching the bauxite ore in concentrated sodium aluminate solution under elevated temperature and pressure. Bauxite residue is not only highly alkaline, but the enormous quantity produced annually is also posing a severe and alarming environmental problem globally. Although the general properties, hence the risen obstacles regarding this by-product are similar worldwide, the composition of the BxR varies from refinery to refinery (Table 1), depending on the content of the bauxite source and the processing conditions. In addition, typically, 10 wt% of the waste consists of LOI (loss of ignition), in form of water, oxalates, flocculants and other organic materials [67]. During the Bayer process, the soluble tecto- and phyllosilicates present in the bauxite transform into both crystalline phases (70 wt%) and amorphous materials (30 wt%). These solids construct 20 to 80 % of the bauxite residue, depending on the disposal route applied.

Table 1 The typical range of the main mineral phases in bauxite residue [8].

Mineral phase	Typical amount (wt%)	Mineral phase	Typical amount (wt%)
Hematite	10 – 30	Calcite	2 – 20
Goethite	1 – 55	Tricalcium-aluminate	2 – 20
Magnetite	0 – 8	Perovskite	0 – 12
Sodalite	4 – 40	Titanium dioxide	2 – 15
Silica	3 – 20	Muscovite	0 – 15
Kaolinite	0 – 5	Boehmite	0 – 20
Cancrinite	0 – 50	Gibbsite	0 – 5

Nowadays, there are four bauxite residue disposal methods used by the industry. Marine discharge was the first and the simplest method, the slurry being disposed directly into the ocean, well offshore. Due to its environmental hazard, for instance, the increased turbidity of seawater in that area and the formation of colloidal metal compounds, since 1981 it was called to be the last resort, only if there is no suitable land disposal available. Lagooning, or wet disposal is another simple method not needing any treatment of the slurry prior to discharge; however, it is very dependent on good engineering practice, having high requirements on the land-based ponds. The importance of the construction and maintenance of the impoundments

was demonstrated by the tragical wall collapse of the Ajka Timföldgyár in 2010. As a result, there is a consistent trend not just from the marine to land-based disposal, but from wet to dry disposal methods as well. Dry stacking, or thickened tailings disposal (TTD) involves the transport of a paste-like residue into the yard. Prior the discharge, its solid content is about 48 – 55 wt%, but the drying solar and air effect reduces the final dry density up to 70% after settling, therefore, the layers can be stacked on each other. This method diminishes earthquake and erosion risks; hence it is the most popular disposal method. Moreover, dry cake disposal method looks to be an environmentally even friendlier and simpler solution, although economically is not an attractive technology yet, and the air pollution caused by the alkaline bauxite residue dust may be the root of severe health problems around this disposal areas if it is not monitored constantly. Compared to the TTD, this method needs pressure filtration after thickening to achieve the solid content > 65 wt% prior to disposal, as a result, bauxite residue is not thixotropic anymore, its rheological properties remain constant in the whole dam [68].

All in all, every solution has its drawbacks and benefits, and the physico-chemical attributes of the bauxite residue makes the waste management challenging.

3.3.1 Application of bauxite residue as secondary raw material

One possibility of a good bauxite residue management would be to reduce the quantity of the waste material by applying it as secondary raw material or by extracting the valuable metals from the residue. Metal recovery can be implemented by several techniques, such as magnetic separation, acid leaching, or hydrometallurgy, depending on the target products. Titanium, vanadium, and rare earth elements (REE) are just a few metals which selective extraction has been studied recently by numerous research groups [69-71]. Bauxite residue can also be used as mineral material in constructions as additives and aggregates of cements, bricks, geopolymers, or tiles [72, 73]. Considering the large specific surface area (according to Gräfe et al. [74] its average is 32.7 m^2/g) of the bauxite residue samples, it can also be an excellent catalyst support and adsorbent for flue gases [75] and wastewater [56, 76]. Despite all the application possibilities of the bauxite residue, it is clear that the neutralization of the waste material is mandatory prior to further use, therefore, as Wang et al. [77] also stated, we should focus first on the neutralization behaviour of the bauxite residue and then we can develop an economically and environmentally feasible solution of waste reuse.

3.3.2 Possible neutralization methods of the bauxite residue (BxR)

Neutralization of bauxite residue may not just reduce the environmental impact of storage but can also increase the number of possible applications by other industries. Therefore, there are many studies in the literature focusing on the possible neutralization techniques of this by-product. One of the well-known methods to reduce the alkalinity of the BxR is the neutralization with seawater considering that Mg^{2+} and Ca^{2+} from the salty liquor react with the hydroxide, aluminate, and carbonate ions of the BxR, thus forming insoluble alkaline solids which buffer the solution in the range of pH 8.2 – 9.0. Although, the target pH is reached with this method, it is only viable in cases where the refinery is close to marine environment [78].

Another popular technique, acidic gas neutralization mainly uses CO_2 or SO_2 to bubble it through the slurry, and the so-forming carbonic or sulphuric acid reacts with the alkaline compounds of the bauxite residue, thus lowering the pH. Unfortunately, pH bounces back up to pH 9.5 can be observed if the contact time is not long enough, therefore, neutralization with flue gas should be ideally used combined with another technique, such as acid leaching [79]. Several mineral acids have been tried as neutralizing agents of the bauxite residue because acid-base reaction usually is a simple and direct chemical reaction. Unfortunately, for BxR the neutralization is more difficult because of the complex composition of the by-product. Moreover, to neutralize the rapidly producing slurry, great quantity of acid is needed at a low cost (pickling liquor waste, for instance, HCl or H_2SO_4), and, based on the literature reports, it would take approximately 50 days to reach the equilibrium in the neutral range due to pH buffers [80].

According to Khaitan et al. [81], pH buffering also takes place at around pH 9.9, 8.7, and 5.0 during the dissolution of the slurry in acidic liquor because of the presence of some solid phases in the bauxite residue, namely tricalcium aluminate, sodium aluminium silicate, and calcite. One can see that to efficiently neutralize the industrial by-product firstly we must understand the chemical reaction of the individual alkaline solids which buffer the pH. In conclusion, the dissolution of the tricalcium aluminate was investigated in this work, which seems to be a buffer in the pH range from 8.7 to 9.9.

3.3.3 Tricalcium aluminate hexahydrate and its neutralization

Tricalcium aluminate hexahydrate, $Ca_3Al_2(OH)_{12}$ or $3CaO \cdot Al_2O_3 \cdot 6H_2O$ (or in cement industry: C3AH6), also known as katoite mineral, belongs to the hydrogarnet group. Hydrogarnets have cubic structure with the general formula $Ca_3(Al,Fe)_2(SiO_4)_y(OH)_{4(3-y)}$, where $0 < y < 3$. The aluminium containing series' end member is the tricalcium aluminate hexahydrate, where the silicon tetrahedra are completely replaced by $(OH)^-$ groups ($y = 3$) [82]. The structure of TCA (**Fig. 5**) consists of AlO_6 octahedral and CaO_8 dodecahedral frameworks. To balance the charge, the OH_4 tetrahedra appear in the vacant sites [83].

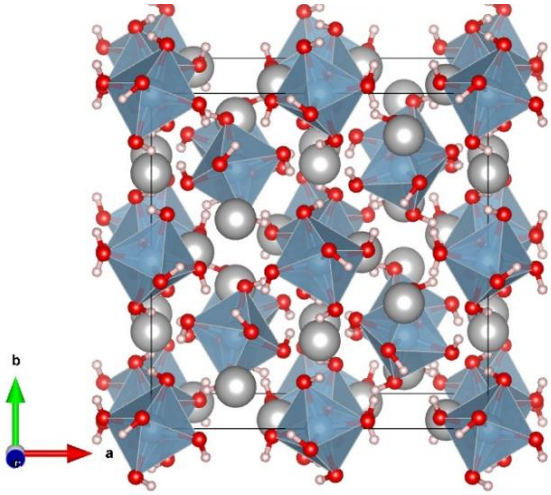

Fig. 5 The crystal structure of the tricalcium aluminate hexahydrate ($Ca_3Al_2(OH)_{12}$). AlO_6 octahedra are painted with blue, Ca atoms are presented as large grey, O as small red, and H as tiny white spheres [84].

The most popular synthesis method in the literature is the hydrothermal preparation in the absence of caustic soda, usually using oxides as starting material and long synthesis time [85, 86]. Another synthesis method is based on the decomposition of other calcium aluminate hydrates in presence of organic acids, but these chemical reactions cannot be perfectly controlled, therefore, the products are usually not uniform, and the reproducibility is also very poor [87, 88]. On the other hand, the TCA produced by these methods do not have the same characteristics as the minerals present in the bauxite residue, hence, there are some studies which aim is preparation of phase pure tricalcium aluminate hydrates under Bayer conditions, using sodium aluminate solution and lime as starting materials [89-91]. Whittington and Cardile [92] concluded that it is complicated to prepare pure TCA because several conditions can affect the success of the chemical reaction. According to them, the best practice is to use low temperature (90 – 150°C), low caustic (C = 100 – 200 g/L), high alumina (A/C = 0.4 – 0.7) concentrations, to exclude carbonate, and any other impurities present in the industrial Bayer

liquor, like NaCl, Na_2SO_4, etc. Moreover, their studies show that CaO has a thermodynamic advantage relative to $Ca(OH)_2$.

Although, there are several studies about the synthesis and characterization of the tricalcium aluminate hexahydrate, to the best of our knowledge, only few of them investigated the neutralization and dissolution process of these solids [93]. However, based on the comprehensive work of Khaitan et al. [81] and Lyu et al. [94], the detailed examination of the neutralization reaction of the TCA is a mandatory first step to solve the problems occurred in the alumina industry due to the high pH of the bauxite residue.

4. OBJECTIVES

In the first step of this work, the goal was to reduce the quantity of the Bauxite Residue by controlling the sodalite formation. For this, a synthesis method was developed to achieve similar sodalite as the one formed under industrial conditions. To verify the similarities of the solids, the products were characterized by different methods. To characterize the various parameters, present in the real-life systems, series of kaolinite samples were utilized during this work, as well as two different pre-treatment methods, milling and calcination, were applied. Moreover, the effect of the organic impurities was also studied on the dissolution behaviour of the kaolinite and the formation mechanism of the sodalite.

As a next step, the final products were not just characterized, an adsorption study was also carried out to examine the possibility of utilization of these industrial by-products as dye adsorbents. Basic Violet 14 was used as a reference dye molecule employed in many industries and in medicine. Its regular shape makes it a perfect compound to calculate and model the adsorbent mechanisms on the surface of the sodalite.

Finally, tricalcium aluminate hexahydrate (TCA) was synthesized with a novel method aiming a formation mechanism similar to the one used in the alumina industry. The so-obtained TCA was then characterized and compared with a reference TCA. The neutralization of these highly alkaline solids was studied in detail hence these are the most alkaline solids in the bauxite residue. By understanding the reaction mechanisms with acids and reducing the pH of the components, bauxite residue could be applied in many industries, solving not one but two problems: waste and resource management.

5. EXPERIMENTAL PART

5.1 Materials

All the materials listed in Table 2 were used as received and their purity was ≥ 98%. Milli-Q water (by Merck Millipore) was used for the preparation of the solutions throughout this work.

Table 2 The list of chemicals used in the experiments.

Name	Abbreviation	Vendor
Irregular aluminium shots	Al	Alfa Aesar
Sodium hydroxide pellets	NaOH	VWR International
≈ 37 m/m% hydrochloric solution	HCl	VWR International
Kaolinite (Eckalite1)	Kaol1	Imerys Minerals
Kaolinite	Kaol2	Alfa Aesar
Kaolinite	Kaol3	Georgia KGa-1B
Kaolinite	Kaol4	Zettlitz/Sedlec
Kaolinite	Kaol5	Sigma-Aldrich
Anhydrous sodium sulfate	Na_2SO_4	Molar Chemicals
Anhydrous sodium carbonate	Na_2CO_3	VWR International
Isopropanol	IPA	Sigma-Aldrich
Dimethyl sulfoxide	DMSO	Sigma-Aldrich
TritonX-100	TrX	Reanal
Polyvinylpyrrolidone, M.W.: 40000	PVP	Alfa Aesar
Polyethylene glycol, M.W.: 6000	PEG	Sigma-Aldrich
Sodium dioctyl sulfosuccinate	DSS	Sigma-Aldrich
Sodium polyacrylate	PAC	Acros Organics
Sodium dodecyl sulphate	SDS	Sigma-Aldrich
Sodium dodecylbenzene sulfonate	SDBS	Sigma-Aldrich
Benzalkonium chloride	BACl	Sigma-Aldrich
Cetyltrimethylammonium bromide	CTAB	VWR International
Hexadecyl pyridinium chloride monohydrate	HDPCl	Sigma-Aldrich
D-sorbitol	Sorb	Sigma-Aldrich

D-fructose	Fruc	Sigma-Aldrich
Sodium-D-gluconate	Gluc	Sigma-Aldrich
α-D-heptagluconate	Hpgl	Sigma-Aldrich
D-mannitol	Man	Sigma-Aldrich
Saccharose	Sac	Reanal
NaY zeolite	YZ	Reanal
Activated carbon	AC	Reanal
Basic Violet 14 (Fuchsin)	BV14	Reanal
calcium hydroxide	$Ca(OH)_2$	VWR International
calcium carbonate	$CaCO_3$	Sigma-Aldrich
aluminium oxide	Al_2O_3	Sigma-Aldrich

5.2 Preparation of the sodium aluminate solution

First of all, a carbonate-free sodium hydroxide solution was prepared following the procedure described by Radnai et al. [95]. To obtain a concentrated (ca. 20 M) NaOH stock solution, NaOH pellets were dissolved in distilled water, then, after the precipitation of the sodium carbonate, the solution was filtered through a PTFE membrane, and finally, standardized by HCl solution via acid-base titration.

Next, the sodium aluminate solution was prepared by slowly dissolving aluminium shots to a diluted (9 M) NaOH solution, keeping the whole system carbonate-free by using a reflux equipped with a CO_2 pipe. The aluminium was slowly added to the mixture, the whole process took 4-5 days, then it was filtered, and the exact concentration of the sodium aluminate solution was determined by classical titration. The final concentrations of the solution used for the sodalite preparation were 2.6 M of NaOH and 1.9 M of $[AlOH_4]^-$, fitting the concentration of the spent liquor in the industry. On the other hand, for the tricalcium aluminate hexahydrate synthesis the so-called pregnant or green liquor (with the concentrations of 3.4 M NaOH and 4.6 M $[AlOH_4]^-$) was prepared with the same method.

5.3 Synthesis of the sodalites

Sodalites were the products of the dissolution experiments, carried out in closed PTFE vessel specifically designed and implemented for this purpose [96]. The spent liquor was stirred and heated up to 95 ± 0.5°C in this vessel by using silicon oil bath. First, sodium sulfate (0.05 M) and sodium carbonate (0.2 M) was dissolved in the liquor, then, 0.09 M kaolinite was dosed

gradually into the vessel. In some cases, organic compounds were also added to the mixture, to mimic the industrial impurities. After six hours of stirring, the dispersion was filtered through a 0.45 μm PTFE filter and the solid was dried at 60°C, on air.

5.4 Preparation of the tricalcium aluminate hexahydrate

For the synthesis of the tricalcium aluminate hexahydrate (TCA), calcium oxide (obtained by the calcination of calcium hydroxide at 1000°C for 8 hours) was added into the green liquor (Ca:Al molar ratio was 1:1), in the same apparatus as the one used during the sodalite synthesis. After mixing the starting materials at 95°C for four hours, the dispersion was filtered, washed with distilled water, and dried under N_2 atmosphere. The TCA prepared with this method here after will be named *Bayer TCA*.

Another method was also used for TCA synthesis and its product will be called *reference TCA*. Here, calcium oxide (obtained from the calcination of calcium carbonate at 1000°C for 12 hours) and aluminium oxide ($CaO:Al_2O_3$ = 3:1 molar ratio) was dry milled in a mixer mill at 12 Hz for 30 minutes (ball:sample mass ratio = 50:1). Next, the mixture was calcined at 1300°C for four hours, and the product was identified with powder XRD as tricalcium aluminate (PDF #38–1429). This oxide was hydrated for two days at 95°C, washed with distilled water, and dried under N_2 atmosphere [97]. This method was found in the literature and only used as a reference in this study.

5.5 Instrumentation and characterization methods

5.5.1 Characterization of the solids

ICP-OES with radial configuration (Thermo Scientific iCAP 7400 ICP-OES DUO spectrometer) was used for the determination of the chemical composition of the kaolinite samples and silica concentration in the Bayer liquor samples (with yttrium as internal standard) diluted and acidified with hydrochloric or nitric acid prior to the measurements. Later, the components of the bauxite residue were characterized by an Agilent 7900 ICP-MS in He gas mode, determining the sodium, aluminium, and silicon concentrations of the solids (the precipitate collected from the reaction vessel after completing the dissolution experiment, see below). The carrier gas was Ar with 15 mL/min gas flow, and He with 1 mL/min flow.

Powder X-ray diffraction (XRD) patterns of the solids were recorded on a Rigaku Miniflex II instrument equipped with Ni foil Kβ filter and scintillation detector operating at 30

kV and 15 mA. 2°/min scan speed was used in continuous mode with step width of 0.02 2θ° and in the range of 2θ = 4–70° applying CuKα (λ = 1.5418 Å) radiation under atmospheric pressure. The registered reflections were identified according to the JCPDS−ICDD (Joint Committee of Powder Diffraction Standards − International Centre for Diffraction Data) database, while the average crystallite sizes were estimated by using the Scherrer using the first reflections (001) of kaolinite, the (211) reflection of the DSP, and the (211) reflection at the TCA samples, applying 0.9 shape factor in all three cases.

The solids were investigated by Fourier-transform infrared spectroscopy, FT–IR (BIO-RAD Digilab Division FTS-65A/896FT-IR spectrophotometer). The normalized spectra (between 4000–600 cm^{-1}) were recorded with 4 cm^{-1} resolution, accumulated from 256 scans for each spectrum, and they were normalized with respect to the most intense absorption band. The measurements were executed in the diffuse reflectance mode (KBr) with a deuterated triglycine sulfate (DTGS) detector.

The water (physisorbed and structural) and organic compound content of the samples were probed by thermogravimetric analysis using a TA instruments Discovery TGA instrument coupled with a mass spectrometer (MS, Hiden Analytical, HPR-20 EGA) up to 1000°C. The thermogravimeter was operated under constant flow (60 mL/min) of Ar containing 5% O_2 at 10°C /min heating rate, while the mass spectrometer applied electron impact ionisation (70 eV energy) and Faraday cup detector to identify the ions in the (m/z) range of 1–300 in full scan mode. The MS transfer line (quartz inert capillary) was maintained at 200°C and 30–40 mg materials were placed into platinum crucibles for the measurements.

The specific surface area and acidity of the samples were mapped by a BELCAT-A catalyst analyser. Before the measurements, the samples were degassed in helium flow at 300°C for 60 minutes to ensure a clean surface, except for the kaolinites calcined at 100 and 200°C, where the pre-treatments were carried out at the (self-explaining) lower temperature for 120 minutes. Before the analysis, the particles were degassed at 60°C for 120 minutes as well. The specific surface area values were determined by using the Brunauer−Emmett−Teller (BET) equation from the adsorption branches of the N_2 adsorption-desorption measurements. To calculate the total pore volumes, the Barett−Joyner−Halenda (BJH) method was applied by using the desorption branches. The samples were saturated with NH_3 at 90°C and heated at constant heating rate of 20°C/min up to 300°C. The NH_3 desorption was detected by a thermal conductivity detector (TCD).

The total organic carbon content of the solids was measured with an Analytik Jena N/C® 3100 apparatus equipped with NDIR detector. The furnace temperature was 950°C. The measurements were made in triplicate.

The morphologies of the materials were examined by scanning electron microscopy (SEM, Hitachi S–4700 type II) at various magnifications and acceleration voltages. A few nm of conductive gold–palladium alloy film was sublimed onto the surface of the solids in order to avoid charging. The microscope was also equipped with energy dispersive X-ray analysis (EDAX) detector (Röntec QX2 spectrometer with Be window) for double-checking the elemental composition of the samples also determined from the ICP results.

A Malvern NanoZS dynamic light scattering (DLS) instrument operating with a 4-mW helium-neon laser light source ($\lambda = 633$ nm) was applied to map the heterogeneity in the particle diameters in solution (due to various degrees of aggregation) and hydrodynamic diameters of the materials at room temperature. The measurements were performed in back-scattering mode at 173°, and the samples were dispersed in distilled water (0.05 g/L dispersion concentration). Sample pretreatment included 1 h ultrasonic irradiation prior to measurements.

The point of zero charge (PZC) of the solids was also determined with the pH drift method, adjusting the pH with HCl and NaOH in 0.1 M NaCl solution. To determine the pH, the solids were suspended in distilled water, having a 0.25 g/L suspension concentration, as during the adsorption experiments, and were stirred for three hours. Then, the pH of the suspensions was measured with a SenTix® H glass electrode.

5.5.2 Pre-treatment of the kaolinites

5.5.2.1 Mechanochemistry

The kaolinite samples were ground prior the dissolution experiments in Retsch MM 400 mixer mill (**Fig. 6**) for different time intervals (from 5 to 60 minutes). The samples were loaded into two stainless steel grinding jars with an inner volume of 50 cm^3 and having one-one grinding balls with 25 mm diameter (8.2 cm^3 volume) in them. The ball/sample mass ratio was constantly 100 and the frequency was 12 Hz in every case. In these type of mills, the jars move in radial oscillations along the horizontal axis and the balls impinge from the rounded ends of the jars, resulting in the deformations of the samples [32].

Fig. 6 Ball mill used during the milling of the kaolinite samples.

5.5.2.2 Calcination

During thermal treatment, 1 g of kaolinite was placed into ceramic crucibles and placed into a Nabertherm Controller B170 muffle furnace (**Fig. 7**). The applied temperature varied from 100 to 1000°C while the heating rate was constantly 20°C/min. The calcination time was regularly 30 minutes, and the pre-treatment was carried out in air.

Fig. 7 Oven used for the calcination of the kaolinite samples.

5.5.2.3 DMSO intercalation

Dimethyl sulfoxide was intercalated between the kaolinite layers (**Fig. 8**) with the modified method of Yuan et al. [98]. 5 g kaolinite was mixed with 5 cm^3 water and 30 cm^3 dimethyl sulfoxide, where water promotes the process by reducing the intercalation energy, according to Wang et al. [99]. The dispersion was stirred for 12 hours at 150°C under reflux,

then, for another 12 hours at room temperature in air. At the end, the solids were washed with 200 cm^3 isopropanol, filtered (pore size: 0.45 μm), and dried at temperatures between 25 and 150°C for two hours.

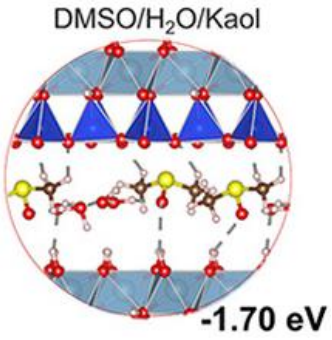

Fig. 8 DMSO and water intercalated between the layers of kaolinite and the calculated energy needed to the process [99].

5.5.3 Adsorption study

Basic Violet 14 stock solutions with 0.1 g/L concentration were prepared with Milli-Q water, then, all the subsequent experiments were executed by diluting these solutions. Adsorption experiments were carried out at ambient temperature in batch mode, under experimental conditions (initial dye and adsorbent concentration, stirring rate, etc.) determined by preliminary studies. The pH and the temperature were not changed due to energetic and financial considerations, regarding to the future industrial applications. After stirring the dispersions for given time (from 5 to 180 minutes), the adsorbents were separated with an 0.45 μm syringe filter and the concentration of the remained dye was determined at λ_{max} = 564 nm with an Analytik Jena Specord 210 Plus double beam UV-Vis spectrophotometer, using a standard quartz cuvette with 1 cm optical length. The adsorption efficiency (R, %) and dye uptake at given time (q_t, mg/g) were calculated using the following equations:

$$R = 100\frac{c_0 - c_t}{c_0} \quad (3)$$

$$q_t = \frac{(c_0 - c_t)}{m}V \quad (4)$$

where c_0 (mg/L) is the initial Basic Violet 14 concentration, c_t (mg/L) is the dye concentration at time t, m (g) is the mass of the adsorbent, and V (L) is the volume of the solution. All the tests were made in triplicate and the standard deviations calculated were marked in the figures.

The adsorption isotherms were determined at room temperature for 24 hours, applying 0.25 g/L adsorbent and 0.005 – 0.1 g/L initial dye concentrations. The experimental data were

fitted assuming different adsorption models, employing the orthogonal distance regression since both the independent (c_{eq}) and dependent (q_{eq}) variables were determined experimentally:

Langmuir equation: $q_{eq} = q_L \frac{K_L c_{eq}}{1+K_L c_{eq}}$ (5)

Freundlich equation: $q_{eq} = K_F {c_{eq}}^{1/n}$ (6)

where q_L, q_T, K_L, K_T and K_F are adjustable parameters; K_L is the Langmuir equilibrium constant of adsorption and q_L is the maximum binding capacity of the adsorbent.

5.5.4 Potentiometry

Potentiometric titrations were performed using a titroprocessor (Metrohm 888 Titrando using tiamo™ 2.5 software for titration control, Metrohm AG, Switzerland) employing an InLab Expert Pro-ISM combined pH electrode from Mettler Toledo. The electrode was calibrated before and after every measurement to 10 points at pH 1.68, 2.00, 4.01, 5.00, 7.00, 9.18, 10.01, 11.00, 12.00, using standard buffers received from VWR International. The measurements were executed in a closed custom-made PTFE vessel thermostated externally with a Julabo F12-MB thermostat to 25 °C.

5.5.5 Modelling the adsorbent-dye interactions

To explain what can happen on the surface of the porous adsorbents, various models have been constructed, and calculations have been performed by the Gaussian16 [100] program package. Density functional calculations were made by B97XD functional [101] which yielded remarkable interaction energies for systems composed of main group elements [102, 103]. The computational modelling and the calculations were executed by András Stirling, and only part of his results will be shown in my thesis aiming to the better understanding of the surface interactions.

6. Results and discussion

6.1 Characterization of the raw kaolinites

Five kaolinite samples were characterized, as-received, by various techniques to determine every possible difference between their physico-chemical properties. Based on the powder XRD patterns and the crystal phase distribution (**Fig. 9**), it was estimated that the main phase was indeed kaolinite, and the constant impurity present in every sample was insoluble quartz, found in 4.6 to 11.6 mass%. Other minor impurities detected were 1.4 mass% anatase in Kaol3, and 2.1 and 3.4 mass% muscovite in Kaol4 and Kaol5, respectively.

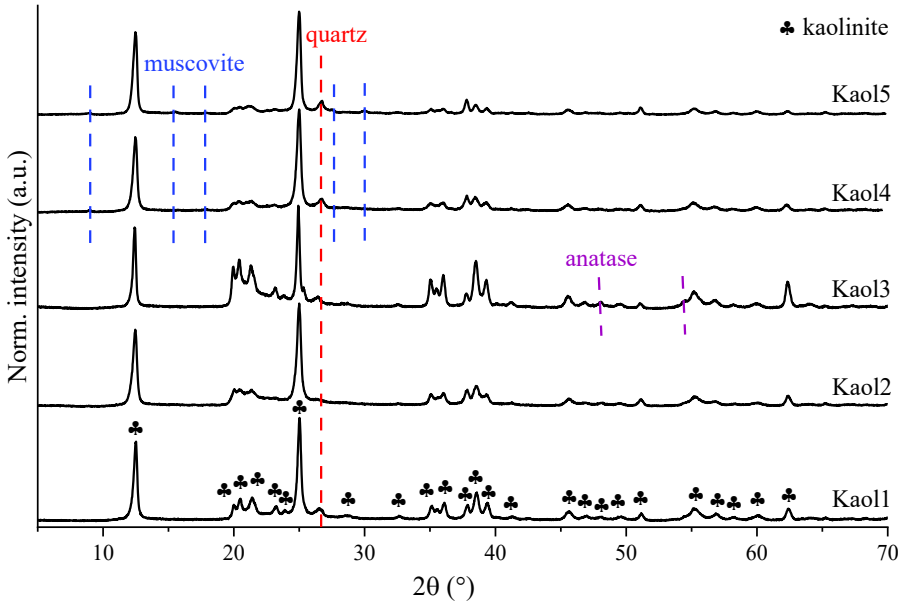

Crystal phase distribution (mass%)				
Sample	Kaolinite	Anatase	Quartz	Muscovite
Kaol1	88.4	< 1	9.5	< 1
Kaol2	92.3	< 1	4.6	< 1
Kaol3	90.7	1.4	6.5	< 1
Kaol4	84.2	< 1	11.6	2.1
Kaol5	84.5	< 1	10.5	3.4

Fig. 9 Powder XRD patterns and the crystal phase distribution of the raw kaolinite samples received from different sources. Measured data were normalized such that the highest value is unity [96].

In Table 3, the main physico-chemical features of the kaolinites are shown from the point of view of the dissolution. Firstly, the crystallinity of the kaolinite, determined by the Hinckley index, was calculated from the characteristic reflections on XRD pattern, based on

the method described by Plancon et al. [104]. The results show that Kaol1 is the most, while Kaol2 is the least crystalline sample, the other three has similar Hinckley indices (≈ 0.9). Based on this, Kaol2 would be expected to have the fastest dissolution rate, and presumably Kaol1 will be slowest of all. From the XRD patterns the average crystallite sizes were also calculated via using the Scherrer equation. The results do not correlate with the Hinckley indices. From here we can anticipate that Kaol3 will have the slowest kinetics, while Kaol2 will have the fastest, because the larger the crystallite, the slower the dissolution should be. On the other hand, these particles can aggregate in solutions, therefore, their hydrodynamic diameter, obtained from the dynamic light scattering measurements, can shade the results of the dissolution kinetics.

The received data displayed a wide range of size in every case, as it can be expected at mined solids without any pre-treatment. From the N_2 adsorption measurements the specific surface areas were also calculated with the BET equation, and the total pore volume with the BJH method. Four samples have pretty similar textural properties, while Kaol5 has a small specific surface area, only 7.8 $m^2\ g^{-1}$, it should have the slowest rate during the dissolution tests. The acidity was determined with NH_3-TPD measurements, and it shows similar changes as the textural parameters discussed previously.

Table 3 The calculated physico-chemical properties of the raw kaolinite samples. Data obtained from the results of various measurement techniques mentioned above [96].

Sample	Hinckley index	Average crystallite sizes (nm)	Hydro-dynamic diameter (nm)	Specific surface area ($m^2\ g^{-1}$)	Total pore volume ($cm^3\ g^{-1}$)	Acidity (mmol NH_3 g^{-1})
Kaol1	1.24	29	300−1000	15.6 ± 0.9	0.053 ± 0.008	0.013 ± 0.002
Kaol2	0.56	23	90−900	16.2 ± 1.2	0.047 ± 0.006	0.010 ± 0.003
Kaol3	0.90	36	150−600	13.7 ± 1.1	0.032 ± 0.006	0.006 ± 0.002
Kaol4	0.85	24	300−850	14.6 ± 0.7	0.040 ± 0.005	0.009 ± 0.002
Kaol5	0.93	23	500−1200	7.8 ± 0.6	0.027 ± 0.003	0.04 ± 0.001

6.2 Dissolution behaviour of the raw kaolinites

The five kaolinite samples were dissolved in hot sodium aluminate solution as it was already described in chapter 4.1.2. and the concentration of the Si(IV) was monitored by ICP-OES (samples were taken from the dispersion and prepared as described in chapter 4.2.1). Then,

the dissolved silica concentration was plotted as a function of time, shown in **Fig. 10**, resulting in different kaolinite dissolution – sodalite formation kinetics. As one can see, Kaol1 gets dissolved with the fastest rate from all samples, moreover, due to this rapid kinetics, more silica can dissolve into the liquor (2.8 g L^{-1} SiO_2 in the maximum). With the slower dissolution mechanism, less silica can dissolve due to the sodalite formation, thus, the overall silica concentration decreases in the maximum point. This maximum can greatly shift (even 120 minutes) depending on the starting material; however, it is not possible to identify one single parameter to explain this observation.

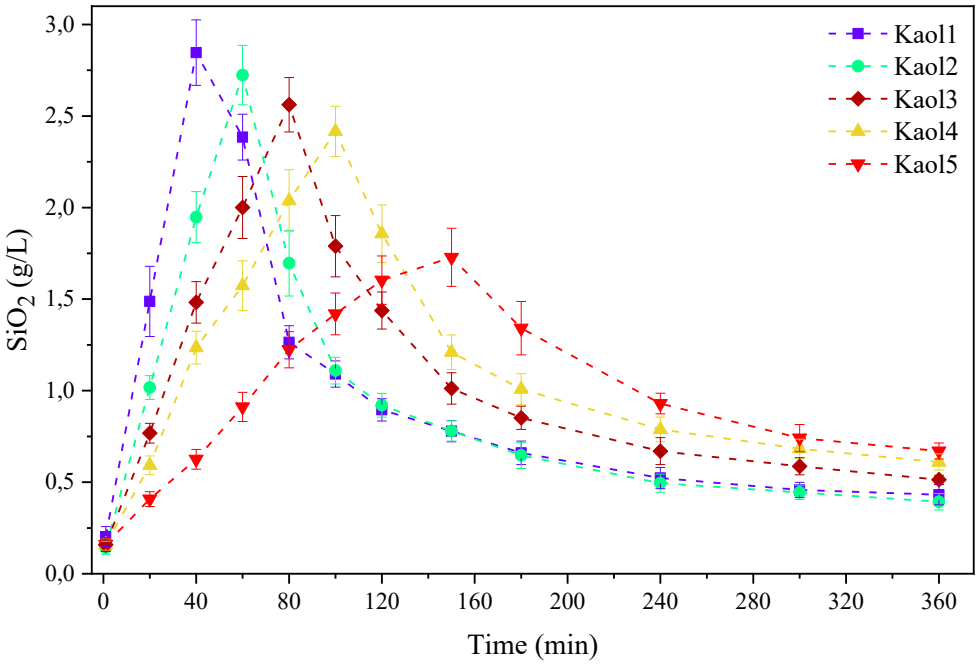

Fig. 10 The dissolution of kaolinites, followed by sodalite precipitation: the variation of the dissolved silica concentration, $[SiO_2]_T$ in g L^{-1} as a function of time. Initial concentrations: $[NaOH]_T$ = 4.5 M, $[Al(III)]_T$ = 1.9 M, $[Na_2SO_4]_T$ = 0.05 M, $[Na_2CO_3]_T$ = 0.22 M, added kaolinite: 23 g L^{-1}, T = 95 ± 0.5°C. First measuring point being at t = 0, maximum of 1 minute mixing time was allowed before [96].

6.3 The effect of mechanochemical and thermal treatments on the physico-chemical characteristics and the dissolution behaviour of the kaolinites

As it was shown, the five kaolinite samples from different sources had different dissolution kinetics; however, none of their physico-chemical properties justified it exhaustively. So far, based on the results, most likely an interplay between the specific surface area, the total pore volume, the Lewis acid site amount and the hydrodynamic diameter seemed to influence the rate of dissolution and the sodalite formation. The other investigated characteristics seem to be much less significant. Therefore, to gain information about the connection between the dissolution under industrial conditions and the properties of the

kaolinites used, a few of their characteristics was changed by mechanochemical activation, then the products were dispensed in the spent liquor.

6.3.1 The effect of the milling time on Kaol1

The as-received Kaol1, Eckalite, a well-known reference kaolinite in the industry, was mechanically activated for 5-, 15-, 30- or 60-minute prior to dissolution. Due to grinding, kaolinites withstood partial structural amorphization visible in the XRD patterns. In **Fig. 11** can be seen that the quartz reflections remained intact while the kaolinite reflections gradually weakened with increasing grinding time, especially the intense (001) and (002). In addition, the (020), (110) and (111) reflections merged which suggests the formation of disordered metakaolinite (MK) phase [105], which results in the fact that the Hinckley indices of the solids were not possible to be calculated in this case. On the other hand, the calculated average crystallite sizes shown in **Table 4**, systematically decreased with the milling time, as it was expected.

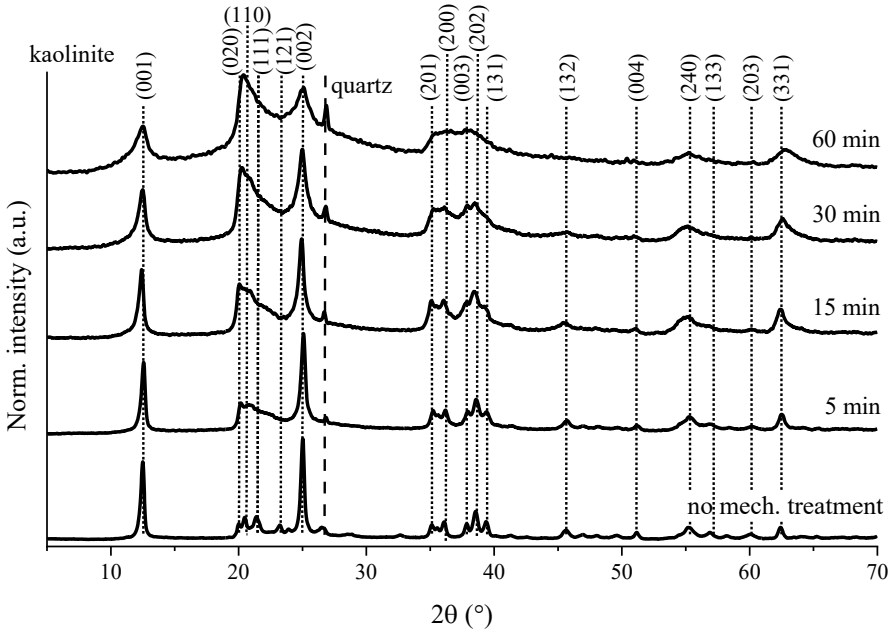

Fig. 11 Powder XRD patterns of the mechanochemically treated Kaol1. Typical kaolinite reflections are shown on the top of the figure. Measured data were normalized such that the highest value is unity [96].

In **Table 4** further physico-chemical characteristics of the milled Kaol1 are shown. The specific surface area of the samples increased with the milling time, because the particles fragmented into smaller particles, until the aggregation tendency of the particles became predominant (after 15 minutes of milling), then the specific surface area and the total pore

volume decreased [33]. The predominant hydrodynamic diameter attested similar changes, the largest sizes were obtained after 15- and 30-minute mechanochemical treatment. The acidity was found to increase with the milling time up to 30 minutes, then it decreased, in parallel with the specific surface area, pore volume and hydrodynamic diameter. The thermogravimetric analysis provides semi-quantitative data about the dehydration/dehydroxylation process, specifically, the mass loss associated with the physisorbed water increases, while the one connected to the structural hydroxyl groups decreases gradually with increasing milling times. The total mass loss remains constant regardless the milling time, suggesting that the released structural water remained in the samples like surface adsorbed/coordinated water.

Table 4 The calculated physico-chemical parameters of the milled Kaol1. Data obtained from the results of various measurement techniques mentioned above [96].

Duration of milling (min)	Crystallite sizes (nm)	Specific surface area (m^2 g^{-1})	Total pore volume (cm^3 g^{-1})	Predomi-ant hydro-dynamic diameter (nm)	Acidity (mmol NH_3 g^{-1})	1st mass loss (%)	2nd mass loss (%)
0	29	15.6 ± 0.8	0.053 ± 0.008	570	0.013 ± 0.002	1.4	15.3
5	27	24.5 ± 1.5	0.058 ± 0.006	450	0.031 ± 0.007	1.9	14.8
15	23	34.4 ± 3.6	0.077 ± 0.012	860, 1250	0.090 ± 0.011	1.7	12.2
30	14	31.7 ± 2.1	0.059 ± 0.011	760, 900	0.102 ± 0.018	4.5	11.2
60	9	12.2 ± 0.6	0.026 ± 0.006	600	0.056 ± 0.007	7.2	7.7

The infrared spectra (**Fig. 12**) of the mechanochemically treated Kaol1 samples confirmed the partial dehydration, hence the formation of metakaolinite, already predicted from the XRD patterns. The bands of the internal and external (Al−OH) stretching vibrations at 3690 and 3620 cm^{-1} progressively disappeared with increasing milling time, while the symmetric and asymmetric adsorption bands of Si−O bonds at 1115, 1040 and 1005 cm^{-1}. Moreover, at 940 and 910 cm^{-1}, the deformation mode of the (Al−OH) groups were shifted and gradually weakened. Under 800 cm^{-1}, the lattice vibrations showed slight changes implying only slight deformations of the internal framework of the solids. The weak signals of Si−O bonds in the quartz phase are visible around 690 cm^{-1} without any significant change in their intensity [106, 107].

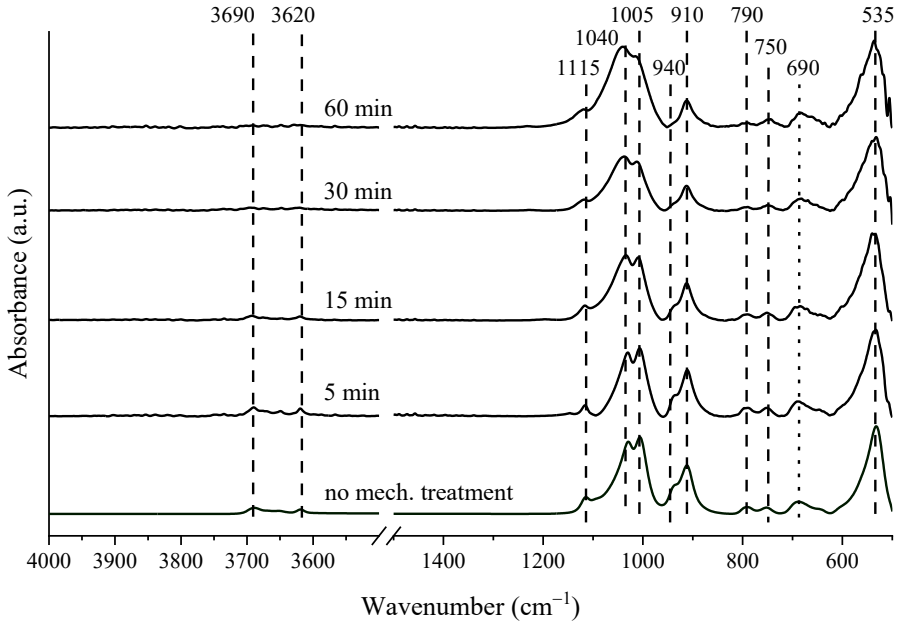

Fig. 12 ATR IR spectra of the milled Kaol1 samples, indicating the position of the maximum of the characteristic vibration bands. The data were normalized such that the highest value is unity, and break was used due to better visibility; no peaks were removed by it. Measured data were normalized such that the highest value is unity [96].

In **Fig. 13** one can see that the mechanochemical activation significantly affected the dissolution behaviour of the solids, the maximum shifted gradually, and more than 15 minutes grinding resulted in practically instantaneous dissolution of Kaol1. These enhanced dissolution rates could be the results of the previously discussed smaller crystallite sizes and the predominant hydrodynamic diameters, but seemingly the acid character of the solids can also be a key factor behind the fact that more dissolved silica was detected in the liquor after dissolving milled Kaol1.

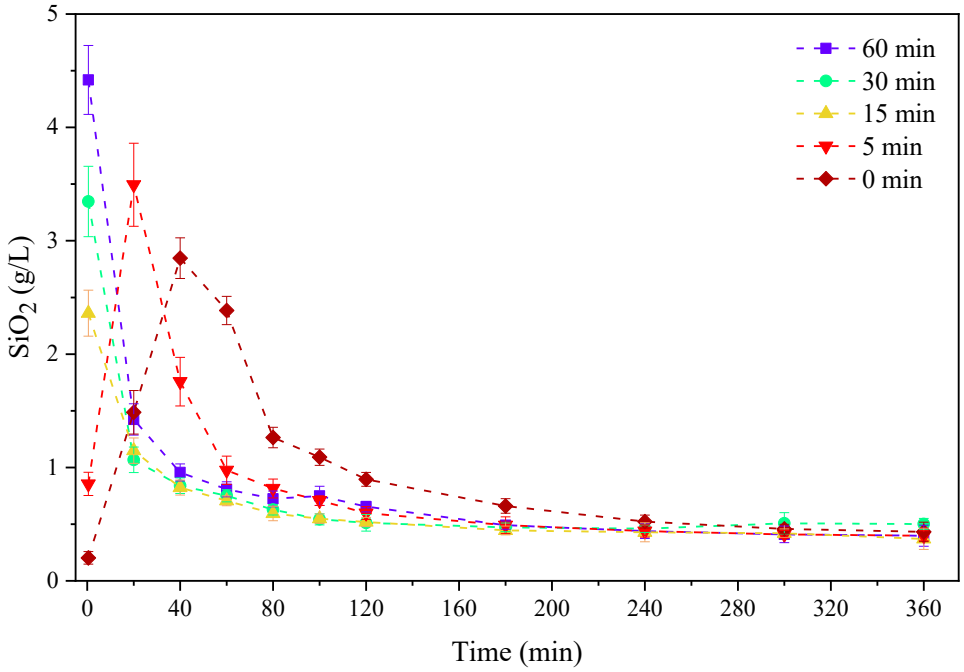

Fig. 13 The dissolution of mechanochemically treated Kaol1, followed by sodalite precipitation: the variation of the dissolved silica concentration as a function of time (expressed in terms of $[SiO_2]_T$ in g L^{-1}). Experimental conditions: $[NaOH]_T$ = 4.5 M, $[Al(III)]_T$ = 1.9 M, $[Na_2SO_4]_T$ = 0.05 M, $[Na_2CO_3]_T$ = 0.22 M, added kaolinite: 23 g L^{-1}, T = 95 ± 0.5°C. The milling times are shown in the graph. First measuring point being at t = 0, a maximum of 1 minute stirring time was allowed before [96].

6.3.2 The effect of thermal treatment on Kaol1

The phase transformations of Kaol1 due to the thermal treatment were followed by powder XRD as it is shown in **Fig. 14**. The calcination up to 500°C shown no variation relative to the raw kaolinite phase (*JCPDS* card no. 01-089-6538). From 550°C the characteristic reflections disappear and an amorphous phase, most probably metakaolinite forms. At 1000°C, although the amorphous phase hides most of the characteristic reflections, the typical reflections of mullite phase (*JCPDS* card no. 01-079-1456) and a Si-Al spinel phase are noticeable. On the other hand, it would be difficult to distinguish these two phases from each other hence their similar compositional and structural properties. Although, based on the study of Chakravorty and Ghosh [108], the Si-Al spinel forms at 980°C and mullite only at higher temperature, at 1250°C, the faster heating rate promotes the formation of the mullite at lower temperatures [109] and the presence of a γ-alumina derived spinel is very plausible [110].

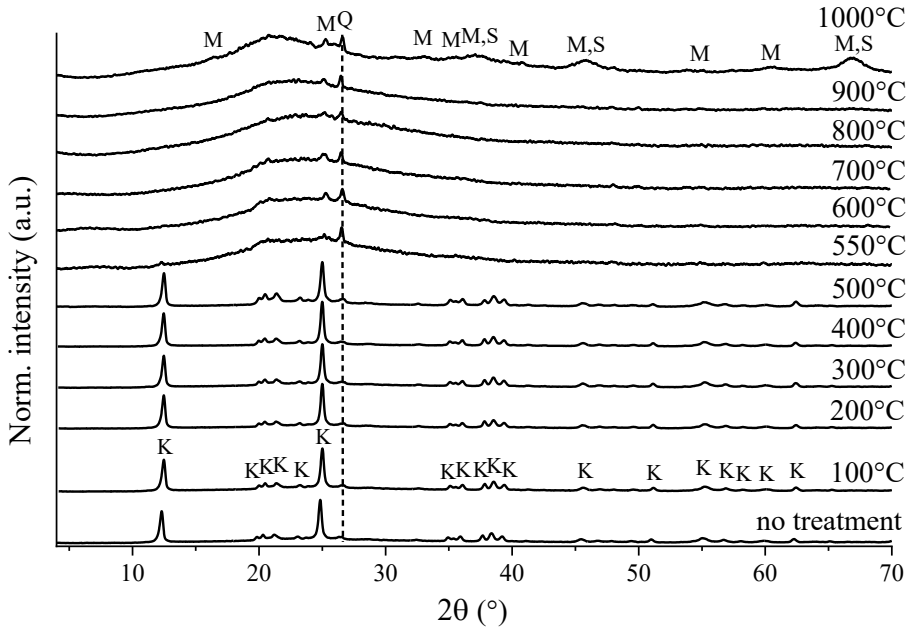

Fig. 14 Powder XRD traces of the calcined kaolinite sample, where K = kaolinite, Q = quartz (present as impurity), M = mullite and S = Si-Al spinel. Measured data were normalized such that the highest value is unity [111].

The specific surface area values, calculated from the N_2 adsorption measurement results, showed no systematic temperature dependence. The different phases formed between 100 – 1000°C had largely similar specific surface areas between 16.6 and 25.3 $m^2\ g^{-1}$, which are only slightly larger than that of the raw kaolinite (**Table 5**).

The acidity of the calcined kaolinites was determined by temperature-programmed desorption of NH_3. The ammonia molecules are removed from the Bronsted acid sites above 300°C, while at lower temperatures, the desorption occurs from the Lewis acid sites built up of either Si-centres formed by dehydroxylation or penta- or tetrahedrally coordinated Al-sites, according to Rodríguez-González et al. [112] and Kumar et al. [113]. As a result of calcination, the binding strength of the NH_3 molecules to the acid centres weakened and a slight decrease in the number of the acidic sites is seen in **Table 5**, especially after the formation of the previously mentioned metakaolinite and spinel type phases. This can be explained with the possible collapse of the layers, thus the increased active surface for the ammonia to adsorb [114, 115], or by the decreased Si:Al ratio on the surface of the samples due to the oxidation [116].

The predominant hydrodynamic diameters (**Table 5**) of the thermally treated kaolinites at T < 500°C are slightly bigger, than that of the raw Kaol1 (570 nm) and the ones calcined at T > 550°C. Moreover, the mainly unimodal character of the size distribution appeared to be bimodal at T > 550°C and finally became a multimodal distribution for the phases formed at

1000°C. These changes suggest that the size distribution of the aggregates widened which could be indirectly explained with the delamination of the particles.

Table 5 The calculated physico-chemical properties of the calcined Kaol1. Data obtained from the results of various measurement techniques mentioned above [111].

Calcination temperature (°C)	Specific surface area (m^2 g^{-1})	Acidity (mmol NH_3 g^{-1})	Predominant hydrodynamic diameter(s) (nm)	Total mass loss (%)
no treatment	15.6 ± 0.8	0.013 ± 0.002	570	16.7
100	16.6 ± 0.8	0.016 ± 0.003	625	14.0
200	19.4 ± 0.8	0.012 ± 0.003	940	14.0
300	20.2 ± 1.6	0.015 ± 0.005	760	13.8
400	17.3 ± 1.1	0.014 ± 0.003	935	13.7
500	19.9 ± 1.0	0.012 ± 0.002	550, 790	9.5
550	23.1 ± 0.8	0.008 ± 0.002	400, 825	3.0
600	19.2 ± 1.2	0.009 ± 0.002	510, 875	2.3
700	18.8 ± 0.9	0.008 ± 0.002	740	1.5
800	22.0 ± 1.4	0.010 ± 0.003	500, 790	0.8
900	20.4 ± 1.4	0.009 ± 0.003	480	0.6
1000	25.3 ± 1.9	0.005 ± 0.001	340, 520, 880	0.7

Thermogravimetry showed a rather colourful thermal behaviour (**Fig. 15**). The solids calcined at T < 500°C behaved in a way very similar to that of the raw kaolinite. First a negligible amount of physisorbed water leaves the surface (up to 100°C), then, the departure of the structural hydroxyl groups was observed around 525°C. Kaolinite samples treated at 500°C had a pretty different behaviour: the total mass loss found to be significantly lower (by about 7 w/w%) compared to the not treated kaolinite sample (**Table 5**). It can indicate that the delamination of the sheets in kaolinite occurs in parallel with the dehydroxylation process. At higher temperatures, the total mass loss decreased from 3 to 0.7 w/w% with the increased temperature of the heat-treatment, however, the minima on the DTG curves varied in a wide range (**Fig. 15**), probably due to the adsorption of water during storage. Thus, a partial rehydration of the metal-oxide moieties can be observed here. The thermogravimetric analysis

of the solid calcined at 1000°C only shows the departure of the adsorbed water on the surface and the leave of the structural hydroxyls at 675°C [117, 118].

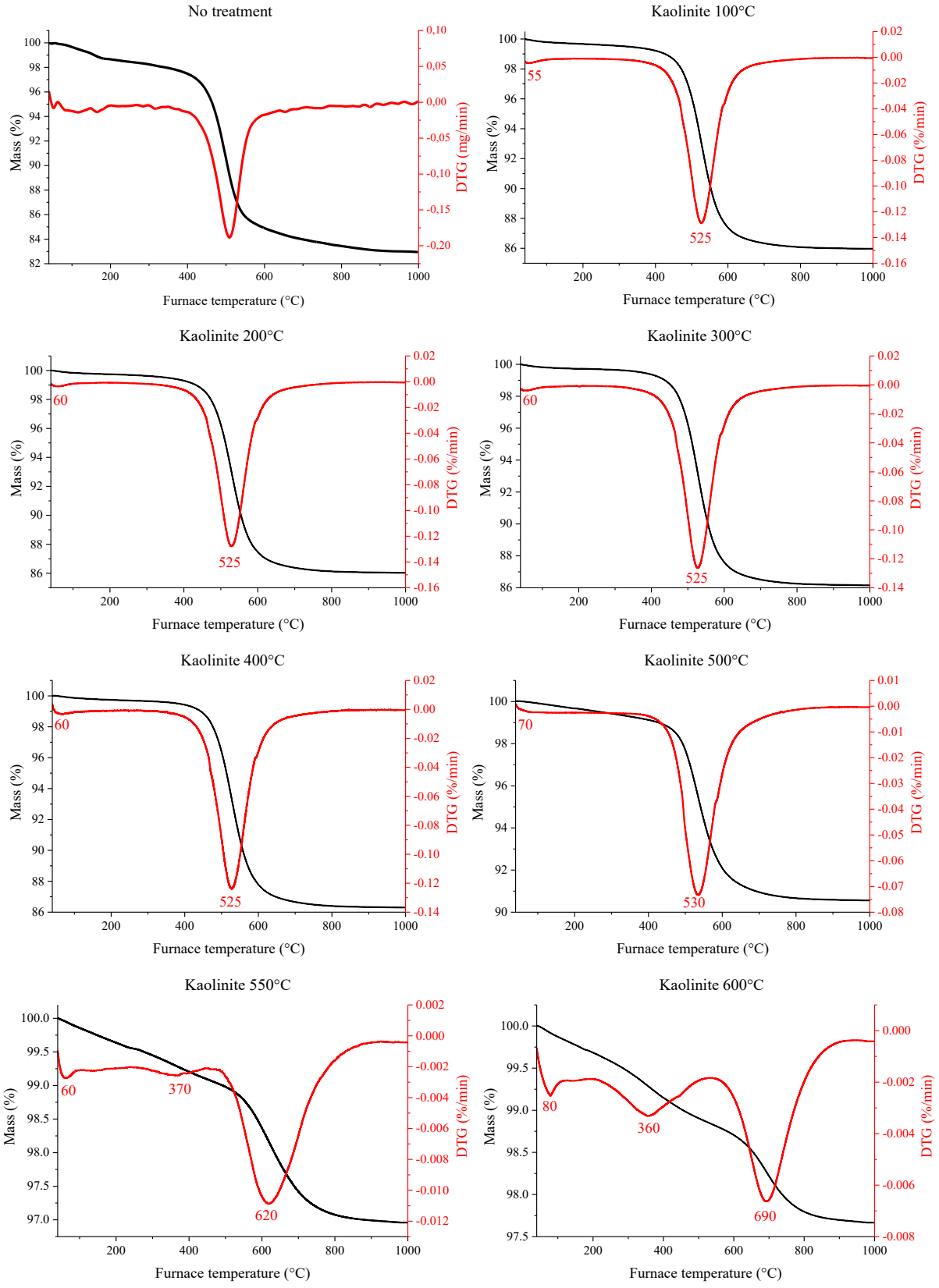

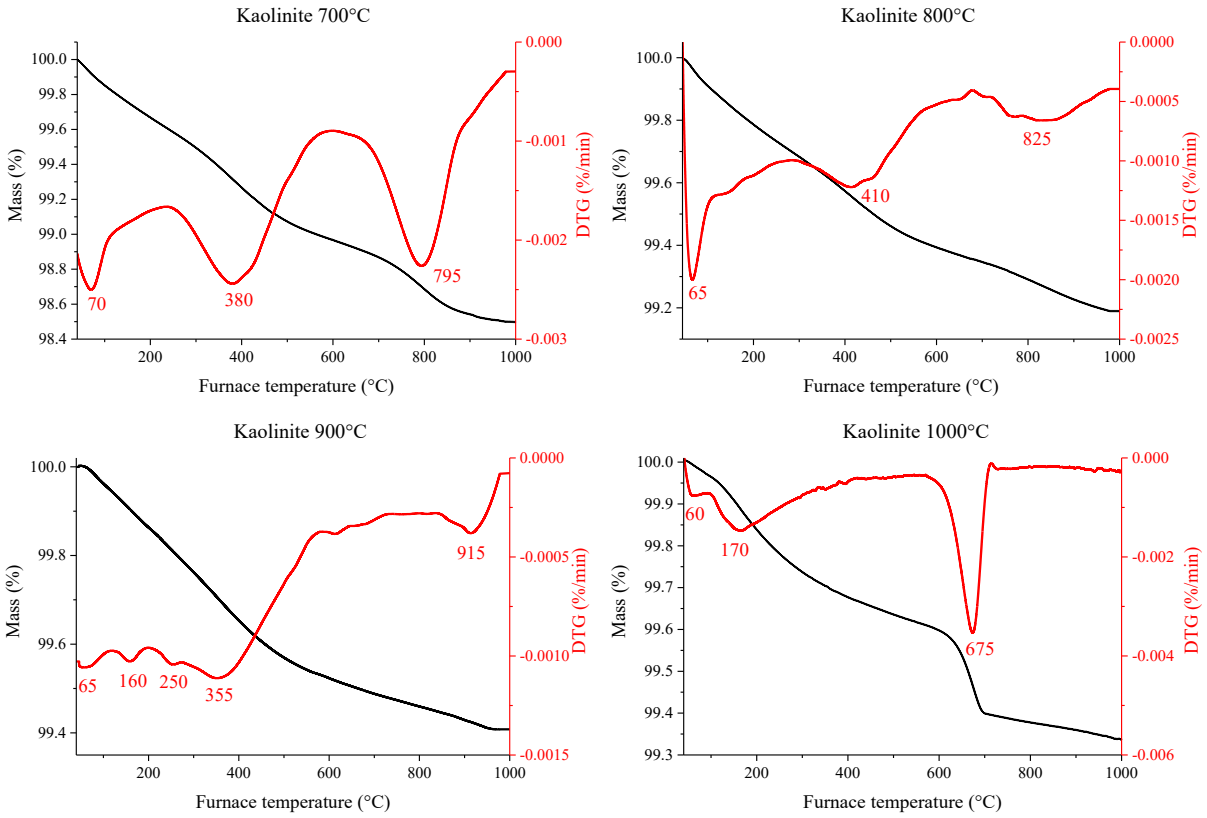

Fig. 15 Thermogravimetric curves of the raw Kaol1 and the heat-treated kaolinite samples from 100 to 1000°C [96, 111].

The dissolution behaviour of the calcined kaolinites strongly depends on the temperature of the heat treatment as well as on the phases formed during this process (**Fig. 16**). Even a mild heat treatment at 100°C resulted in higher maximum dissolved silica concentration ($[SiO_2]_{max}$ equal approximately with 4.8 g L^{-1}), than the raw Kaol1 ($[SiO_2]_{max}$ being around 3 g L^{-1}). The calcination under 500°C showed similar result at every temperature value, more precisely, an increase in $[SiO_2]_{max}$ (up to 4.8 g L^{-1}).

Although, the characterization of the kaolinite sample calcined at 500°C showed similarities with the ones treated at lower temperatures (see above), its dissolution behaviour was noticeably unique: the dissolution of the kaolinite seems to be practically instantaneous, moreover, no peak can be observed because of the favoured sodalite formation at the start of the experiment. (Hereafter, this phenomenon will be called "instantaneous dissolution" in this work.) The XRD and thermogravimetric measurements did not indicate significant dehydroxylation, the results of the treated sample at 500°C were pretty similar to the ones of the raw kaolinite. As before in **Fig. 13** after more than 15-minute milling, the delamination of the kaolinite can be a potential reason behind this phenomenon. The dissolution was preferred

because the activation weakened the hydrogen bonding, therefore, the peeling of the crystal planes happened, which enhanced the accessibility of the surfaces [119].

The calcination between 550°C and 900°C resulted in a dramatically increase of the dissolved silica concentration, the measured $[SiO_2]_{max}$ was 7.98–9.46 g L^{-1}. Moreover, the position of the maxima shifted by 20 minutes, suggesting that the dissolution kinetics of the kaolinites became faster due to thermal treatment. Peng et al. also observed these changes in the dissolution behaviour after thermal activation of the kaolinite samples, however, their reaction conditions were slightly different from ours (lower starting kaolinite and aluminate amounts) [120]. At 1000°C new phases were formed; thus, the completely different dissolution behaviour was more or less expected.

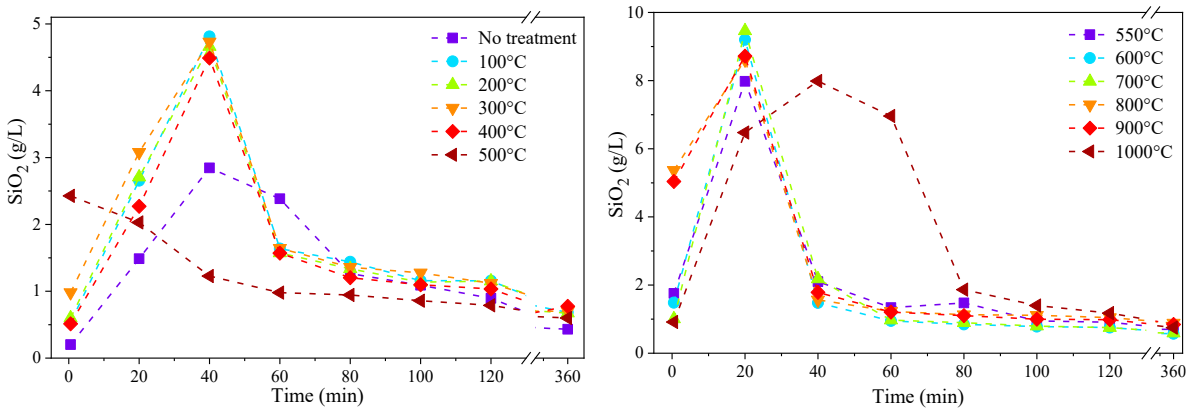

Fig. 16 The dissolution of the thermally treated kaolinites, followed by the precipitation of the sodalite: graph shows the variation of the dissolved silica concentration (denoted as $[SiO_2]_T$ in g L^{-1}) as a function of time. Experimental conditions: $[NaOH]_T$ = 4.5 M, $[Al(III)]_T$ = 1.9 M, $[Na_2SO_4]_T$ = 0.05 M, $[Na_2CO_3]_T$ = 0.22 M, added kaolinite: 23 g L^{-1}, T = 95 ± 0.5°C. The temperature of the heat-treatment is shown in the figure above. First measuring point being at t = 0, a maximum of 1 minute stirring time was allowed before [111].

6.3.3 The combined effect of the mechanochemical and the thermal treatment on Kaol1 sample

From the results of the previous chapters, it is clear that an instantaneous dissolution is achievable with at least 15-minute milling, however, with higher milling time, the maximum silica concentration of the solution can be increased. Furthermore, the 500°C heat treatment facilitates this rapid dissolution by weakening the hydrogen bonds and peeling the crystal planes. Therefore, the synergic effect of the two consecutive treatments should result in instantaneous dissolution with higher silica concentrations than each treatment alone. When the grinding anticipated the calcination, the sample was denoted as 15/60 min milling (depending on the milling time) + 500°C, and in the reverse cases vice versa.

As it was foreseeable, calcination resulted in the amorphization of the kaolinite phase and the formation of metakaolinite. As it is visible in **Fig. 17**, the deterioration of the kaolinite particles is more pronounced, when the first step was grinding of the samples. The XRD pattern of the solid milled for 60 minutes, then calcined at 500°C is very similar to the diffractogram of the metakaolinites shown in **Fig. 14** where the kaolinite samples suffered a heat treatment between 550°C and 900°C. In the other cases, the most intense (001) reflection of the kaolinite phase was still well detectable, thus, the crystallite sizes of the particles could be calculated (**Table 6**), and they showed a decreasing tendency. Calcination unequivocally could aid further the amorphization of the solids compared to the patterns of the solids milled for 15 and 60 min.

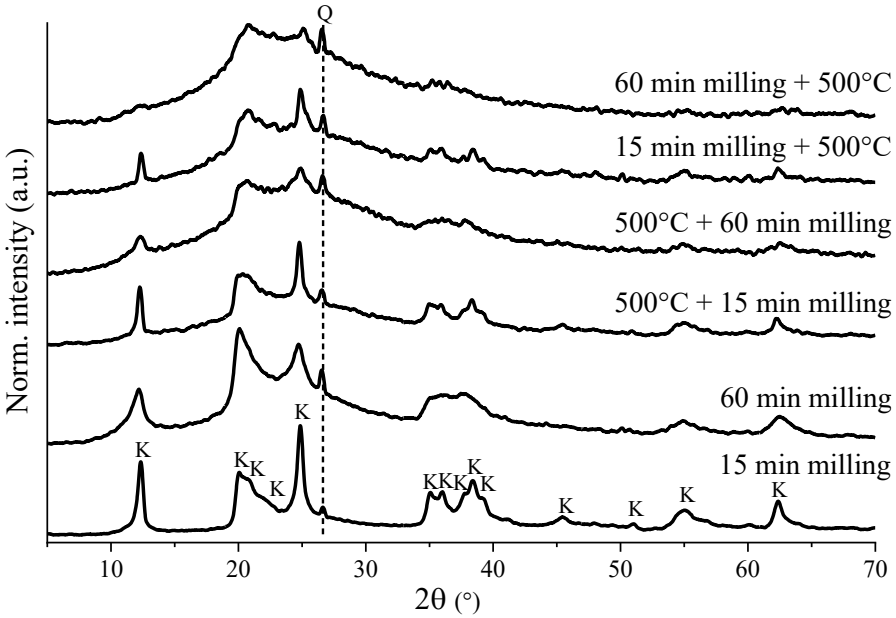

Fig. 17 Diffractograms of the kaolinites which were subjected to heat- and/or mechanochemical treatment in various orders. The characteristic reflections of the kaolinite are denoted on the XRD patterns by K. The characteristic reflection of quartz is marked by Q. Measured data were normalized such that the highest value is unity [111].

The physico-chemical properties of the samples obtained by the above-mentioned combined treatments are summarized and compared with each other in **Table 6**. Moreover, the characteristics of the samples introduced before, with none or only a single treatment was used as references, so the cooperative effect of the calcination and the grinding could be investigated. The average crystallite sizes decreased as a result of the combined treatment. The calcination decreased the specific surface areas compared to the sample milled for 15 min, although, the 60 min milling had an inverse effect on this parameter. The acidity of the samples slightly increased, when grinding step was combined with the heat treatment, but their acidity was found to be significantly lower than of the milled-only kaolinites. The predominant hydrodynamic

diameters decreased during the milling due to the delamination and fragmentation, also delamination and dehydroxylation of the surface hydroxyl groups occurred as a result of the calcination. The total mass loss values showed interesting results, namely, when the mechanochemical treatment was the second step, the values increased up to the value obtained for the calcined-only sample. These data revealed a prominent difference between the order of the treatments, milling being the first step probably facilitates the metakaolinite formation.

Table 6 Calculated physico-chemical characteristics of the milled and/or calcined Kaol1. Data obtained from the results of various measurement techniques mentioned in the previous chapters [96, 111].

Sample	Average crystallite sizes (nm)	Specific surface area ($m^2\ g^{-1}$)	Acidity (mmol $NH_3\ g^{-1}$)	Predominant hydrodynamic diameters (nm)	Total mass loss (%)
no treatment	29	15.6 ± 0.8	0.013 ± 0.002	570	17.0
500°C calcination	28	19.9 ± 1.0	0.012 ± 0.002	550, 790	9.5
15 min milling	23	34.4 ± 3.6	0.090 ± 0.011	860, 1250	13.9
60 min milling	9	12.2 ± 0.6	0.056 ± 0.007	600	14.9
15 min milling + 500°C	16	26.4 ± 1.3	0.018 ± 0.003	380, 650	7.5
60 min milling + 500°C	–	17.8 ± 0.9	0.017 ± 0.003	590	4.4
500°C + 15 min milling	19	19.3 ± 1.2	0.023 ± 0.005	525	11.5
500°C + 60 min milling	6	14.1 ± 0.7	0.011 ± 0.003	620	10.9

Following the pre-treatments detailed above, the phenomenon of “instantaneous dissolution” was observed for most of the samples. In two cases, namely when the heat-treatment was combined with the 60 min milling, the trigger points were found to be at 20 minutes (**Fig. 18**). The appearance of the maxima at 20 min could be clearly connected to the presence of the metakaolinite phase (see results above), as well as the high dissolved silica concentration (9.4 g L^{-1} for the sample treated for 60 min milling + 500°C). Comparing the dissolution behaviour illustrated in **Fig.18** with the various kaolinites either milled or calcined solely, the combination of the pre-treatments resulted in concentration increase for almost all cases. Furthermore, the dissolution rates fastened up due to the pre-treatments.

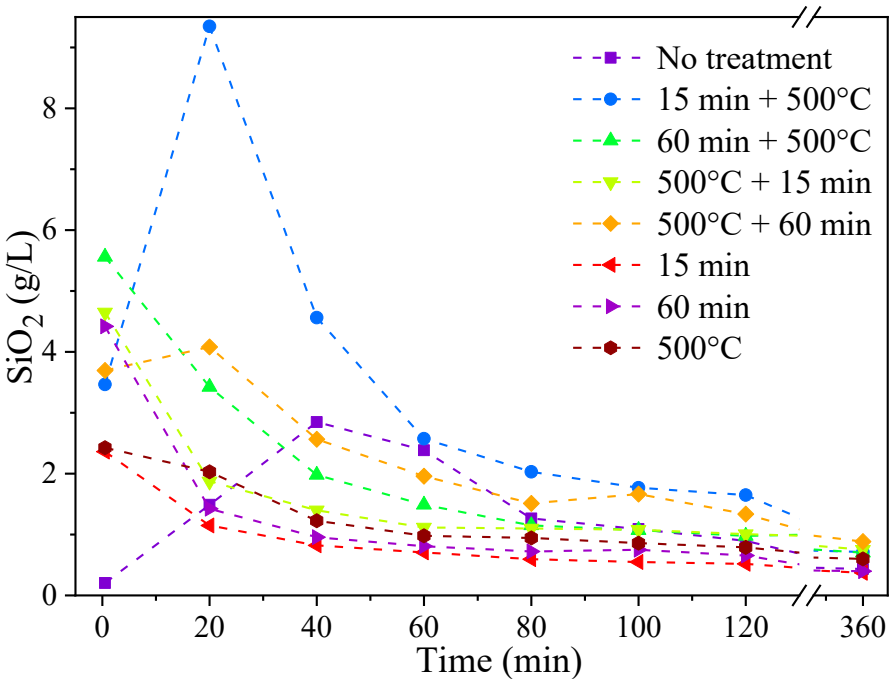

Fig. 18 The dissolution of the mechanochemically and/or thermally treated kaolinites, followed by the precipitation of the sodalite: graph shows the variation of the dissolved silica concentration (denoted as $[SiO_2]_T$ in g L^{-1}) as a function of time. Experimental conditions: $[NaOH]_T$ = 4.5 M, $[Al(III)]_T$ = 1.9 M, $[Na_2SO_4]_T$ = 0.05 M, $[Na_2CO_3]_T$ = 0.22 M, added kaolinite: 23 g L^{-1}, T = 95 ± 0.5°C. The conditions of the pre-treatments are shown in the figure above. First measuring point marked at t = 0, a maximum of 1 minute stirring time was allowed before [111].

6.3.4 The effect of DMSO intercalation on the properties of Kaol1

The effect of delamination without fragmentation or dehydroxylation was investigated by the intercalation of DMSO between the kaolinite layers with the method described in **chapter 4.2.2**. The success of the intercalation was confirmed by the shift of the (001) reflection toward 8.01 2θ°, 1.10 nm basal distance in **SI. 1** figure of the Supplementary Information, characteristic of DMSO−kaolinite composites, characteristic also mentioned in other studies [98, 121]; however, only a partial intercalation was obtained due to the omission of the pre-milling step. It was skipped in order to avoid the effects of the mechanical activation, like fragmentation and amorphization. The FT-IR spectra shown in (**Fig. 19A**) also justify the intercalation, peaks at 3540, 3500 cm^{-1} (hydrogen bonds with the Al–OH groups), at 3025 and 2930 cm^{-1} (C–H bands) and at 1430, 1385 and 1320 cm^{-1} (sulfinyl stretching vibrations) validate the incorporation of the DMSO [121]. The thermal analysis of the solids registered only the departure of the water at 155°C and DMSO molecules at 520°C, with 18 and 78 m/z values, respectively (**SI. 2**). According to the thermogravimetry and elemental analysis (**SI. 3**) the chemical composition of the DMSO−kaolinite system was calculated:

$Al_2Si_2O_5(OH)_4(DMSO)_{0.53}$. Unfortunately, the acidity could not be measured accurately because the intercalated DMSO covered the acid centres, thus blocked the adsorption of the NH_3 molecules.

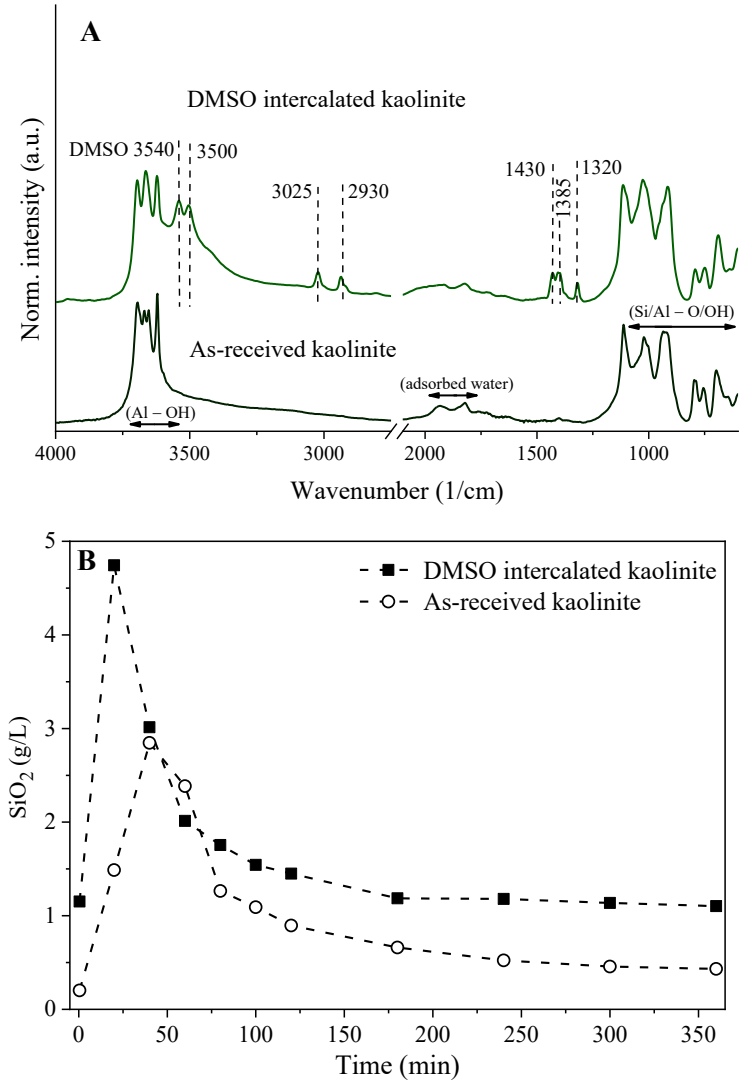

Fig. 19 Infrared spectra of the as-received kaolinite and DMSO intercalated kaolinite (A) and the dissolution behaviour of the as-received kaolinite and the DMSO intercalated kaolinite (B). Measured IR data were normalized such that the highest value is unity. Concentration and composition of the sodium aluminate solution is as before [111].

In **Fig. 19B** the dissolution behaviour of the DMSO intercalated kaolinite shows that due to the delamination, the maxima decreased by 20 minutes relative to raw kaolinite. The DMSO presumably decreased the strength of the interlayer forces by replacing the original hydrogen bonds, and it promoted the collapse of the kaolinite structure during dissolution. The presence of DMSO between the layers resulted in a notable increase in $[SiO_2]_{max}$, similar to the concentrations measured after the heat treatment under 500°C. The separate addition of DMSO

to the spent liquor did not result in any change neither in the position of the maxima, nor in the significant concentration increase, as it can be seen further in this work, in **chapter 6.7**.

6.4 The investigation of the dissolution product

Interestingly, after the 6-hour reaction times, the final silica concentrations were found to be practically the same for all samples (~1 g L^{-1} SiO_2), independent of the pre-treatment method. It suggests that the products forming are always the same or pretty similar. Accordingly, they were investigated in this chapter.

Based on the X-ray diffractograms (**Fig. 20A**) and the infrared spectra of the solids, a mixture of different anion-containing sodalites was obtained, next to the contaminants present in the starting materials, namely quartz (SiO_2, JCPDS card no. 01-085-0457), anatase (TiO_2, JCPDS card no. 01-071-1166) and muscovite ($KAl_2(AlSi_3O_{10})(OH)_2$, JCPDS card no. 01-082-0576). The identified materials based on the XRD database were hydroxy-sodalite ($Na_8(AlSiO_4)_6(OH)_2(H_2O)_2$, JCPDS card no. 01-076-1639), lazurite ($Na_8(AlSiO_4)_6SO_4$, JCPDS card no. 01-077-1702) and carbonate-nosean ($Na_8(AlSiO_4)_6CO_3$, JCPDS card no. 01-089-0843). In case of Kaol4 and Kaol5, incomplete transformation could be observed, the typical reflections of kaolinite traces ($Al_2Si_2O_5(OH)_4$, JCPDS card no. 01-089-6538) were identified around 12, 21, 25 and 38 2θ°. This indicates that longer digestion time is needed for certain kaolinite samples, and the properties of the mined kaolinites can greatly influence the formation rate of the sodalites.

The IR spectra confirmed the powder XRD findings, the presence of the CO_3^{2-} and SO_4^{2-} ions are undeniably visible in **Fig. 20B,** at 660 and 1390 as well as at 615 and 1140 cm^{-1}, respectively [107]. The spectra show internal and external Al−OH stretching vibrations between 3695 and 3620 cm^{-1}, while broad bands of crystalline water hydroxyl groups around 3400 cm^{-1} and the bending vibrations of water molecules at 1640 cm^{-1}. At 1115, 1030 and 1005 cm^{-1} the signal of symmetric and asymmetric absorption bands of Si−O and further tetrahedral (Si, Al)−O bands at 975 cm^{-1} are seen. The strong shoulder-type peak around 940-915 cm^{-1} and the peaks under 800 cm^{-1} can be attributed to the deformation mode of Al−OH and the Si−O−Al parts, respectively, with the weak signals of Si−O bonds in the quartz phase around 690 cm^{-1} [106, 107, 122]. Although it is difficult to support with these methods, according to Vogrin et al. [6] the molar amount of the hydroxide and tetrahydroxoaluminate anions were significantly larger in the spent liquor than the sulfate and carbonate anions had, thus the formation of the sodalites with $OH^-/Al(OH)_4^-$ anions incorporated in the cage is plausible.

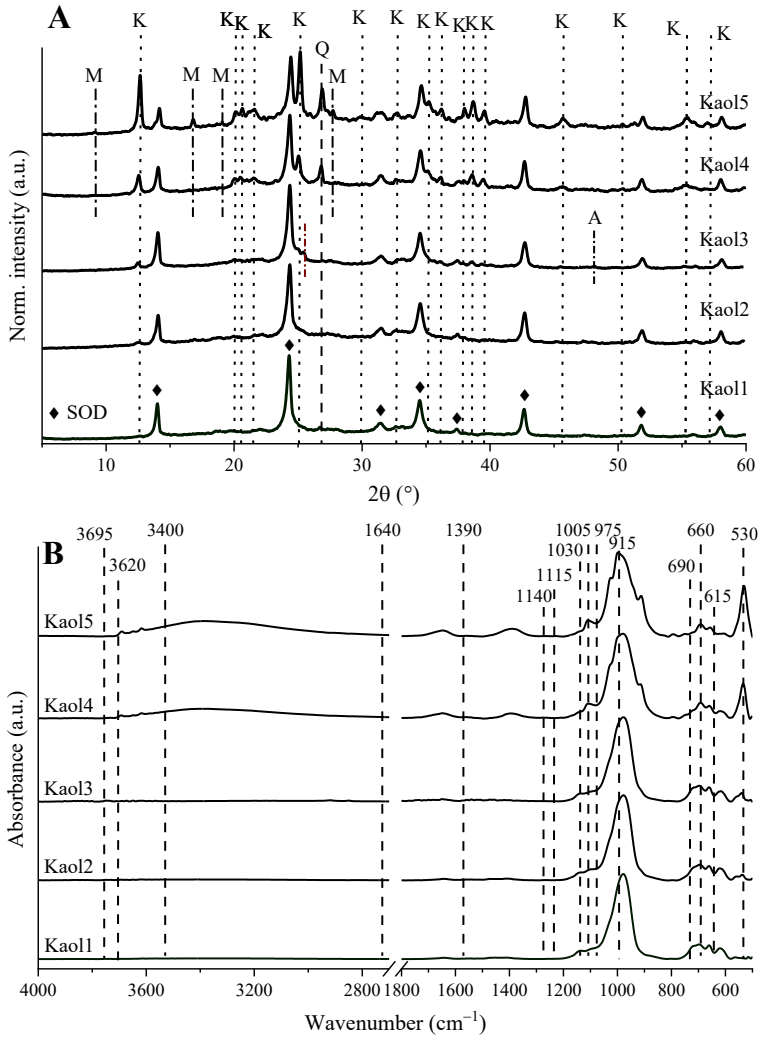

Fig. 20 Powder XRD traces of the solids at the end of dissolution (A), obtained by using various kaolinite samples and separated at the completion of the kinetic runs from the reaction mixtures. Next to SOD, there are by-products/impurities present in the sample: K = kaolinite (not transformed to SOD yet) and the impurities also visible in the kaolinite samples: Q = quartz, M = muscovite, A = anatase. IR spectra of the solid product (B), obtained at the end of the dissolution tests. The presence of the CO_3^{2-} and SO_4^{2-} ions are visible at 660 and 1390 as well as at 615 and 1140 cm^{-1}, respectively. Symbols show new phases forming upon neutralization. Measured data were normalized such that the highest value is unity [96].

The sodalites showed the well-defined ball of yarn-type lepispherical structures [123], even after pre-treatments (**Fig. 21**). The enhanced dissolution rates resulted in a higher number of nuclei, thus in the formation of SOD particles with smaller sizes. Although higher silica concentrations increased the growth rate of the sodalite crystals, metakaolinite formation proved to be the key factor. This is proven by the large lepispheres formed from the thermally treated kaolinites, where metakaolinite formation was also observed. Although, the biggest balls

(around 2000 nm) were produced using the combination of 60 min milling and 500°C calcination prior to dissolution.

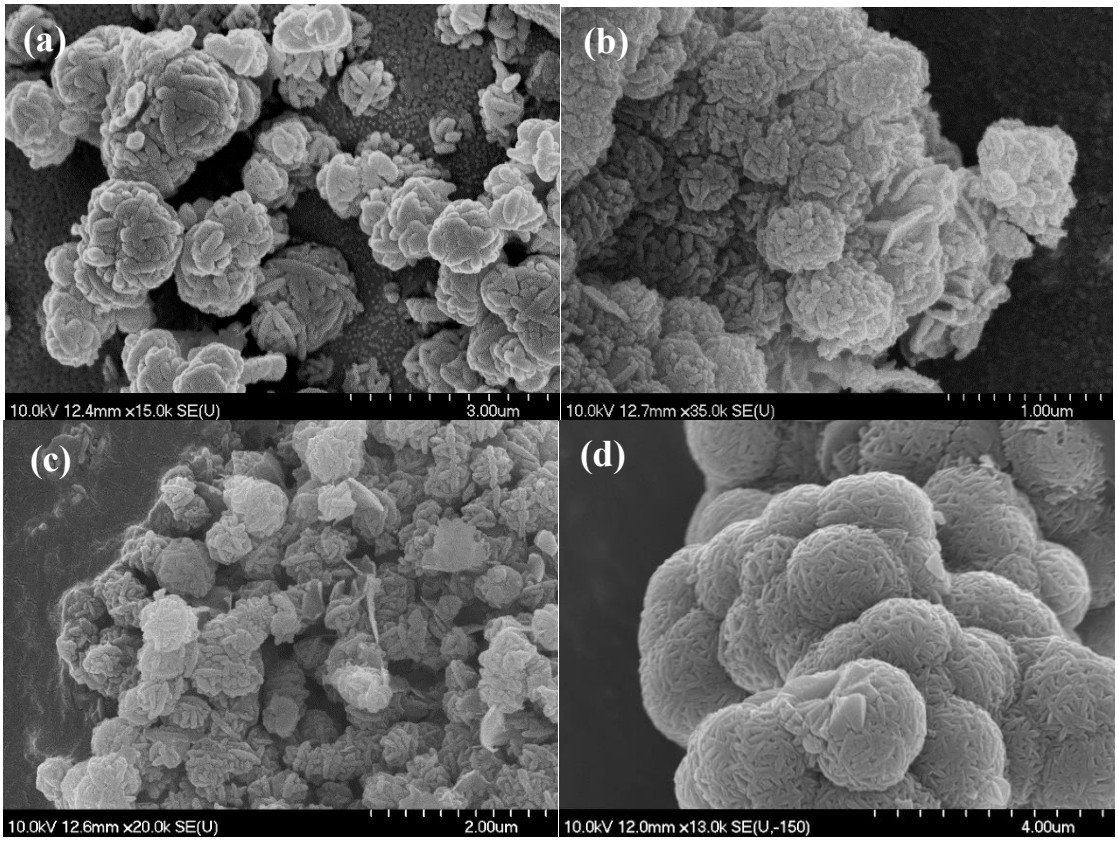

Fig. 21 SEM images of sodalite lepispheres after the 6-hour dissolution in the spent liquor of (a) not treated and activated kaolinite samples: (b) 60 min milling, (c) heat treatment at 500°C and (d) 60 min milling + 500°C calcination [96, 111].

6.5 Comparison of sodalite and Y zeolite

The physical properties of the sodalite (from kaolinite without any treatment) have been compared with the characteristics of the well-known Y zeolite. First, the XRD patterns were studied, checking not only the crystal phases of the solids and the presence of any crystalline impurities, but also their average crystallite sizes. The zeolite has smaller average crystallite size (28 nm), calculated from the first reflections of the solids, than SOD (37 nm) suggesting that the former will have greater specific surface area. This assumption was confirmed with the results of the N_2 adsorption-desorption measurements, which not only gives us information about the specific surface area and the average pore volume, but also about the porosity of the solids. The sodalite has smaller specific surface area with at least one order of magnitude (19 $m^2\ g^{-1}$) than the zeolite (563 $m^2\ g^{-1}$), probably because of the specific framework of the latter. The thermogravimetric measurements show, on one hand, that the only significant mass loss is the physisorbed water loss below 300°C, in the case of both adsorbents. The two endothermic

minima suggest the departure of the greater mass from the external surface and from wider pore windows, at the lower temperature, and less water removal from the internal pores with smaller diameter and from inside the cages. On the other hand, zeolite contains more water (23.38 wt%) than sodalite (9.84 wt%), probably because of its greater specific area and extensive pore system. The pH of the two suspensions is above the PZC, which means that there are negative charges on the surface of the solids. According to the results shown in **Table 7**, the zeolite has more deprotonated silanol groups on the surface, therefore, the electrostatic attraction between the adsorbent and the cationic dye is greater than in the case of SOD, where the pH of the suspension is only slightly above the PZC.

Table 7 Comparison of the specific characteristics of the untreated SOD and the zeolite [124].

Adsorbent	Average crystallite size (nm)	Specific surface area (m^2 g^{-1})	Average pore size diameter (nm)	$pH_{suspension}$	pH_{PZC}
sodalite	37	19	0.78	9.1	9.2
zeolite	28	563	1.3–1.5*	8.1	7.5

* According to the literature [17, 125].

6.6 Adsorption isotherm of sodalite and zeolite

To determine the optimum adsorption parameters of Basic Violet 14 on SOD, the effects of the major operating factors were studied (**Fig. 22**). The findings show that the efficiency of the BV14 removal is practically independent of the stirring rate. The main part of the dye adsorption takes place in the first 60 minutes and reaches equilibrium afterwards, visible in the deceleration of the sorption rate. The increase of the initial dye concentration leads to an increase in the amount of adsorbed dye. Although adsorption theory indicates that adsorption should decrease as temperature increases, decreasing viscosity and increasing molecular motion at higher temperatures apparently allows the organics to enter the pores more easily.

Our results revealed that the uptake of the BV14 increased with the increasing temperature which can be attributed to the formation of hydrogen bonds between the surface of the SOD and the adsorbate, chemisorption being an endothermic process in contrast to the adsorption in gas phase which is exothermic. This bond formation is favoured, having the adsorption at a pH close to the PZC of the desilication product (see in **Table 7**). On the other hand, reaching the equilibrium did not fasten, 60 minutes were also needed at higher

temperatures. All experiments were performed at the natural pH of the solutions. All measurements were carried out at least three times. In continuation, the experiment focused on the comparison of the adsorbents' efficiency with 60 mg L^{-1} initial dye concentration and 250 mg L^{-1} adsorbent concentration, at ambient temperature (26 ± 1°C).

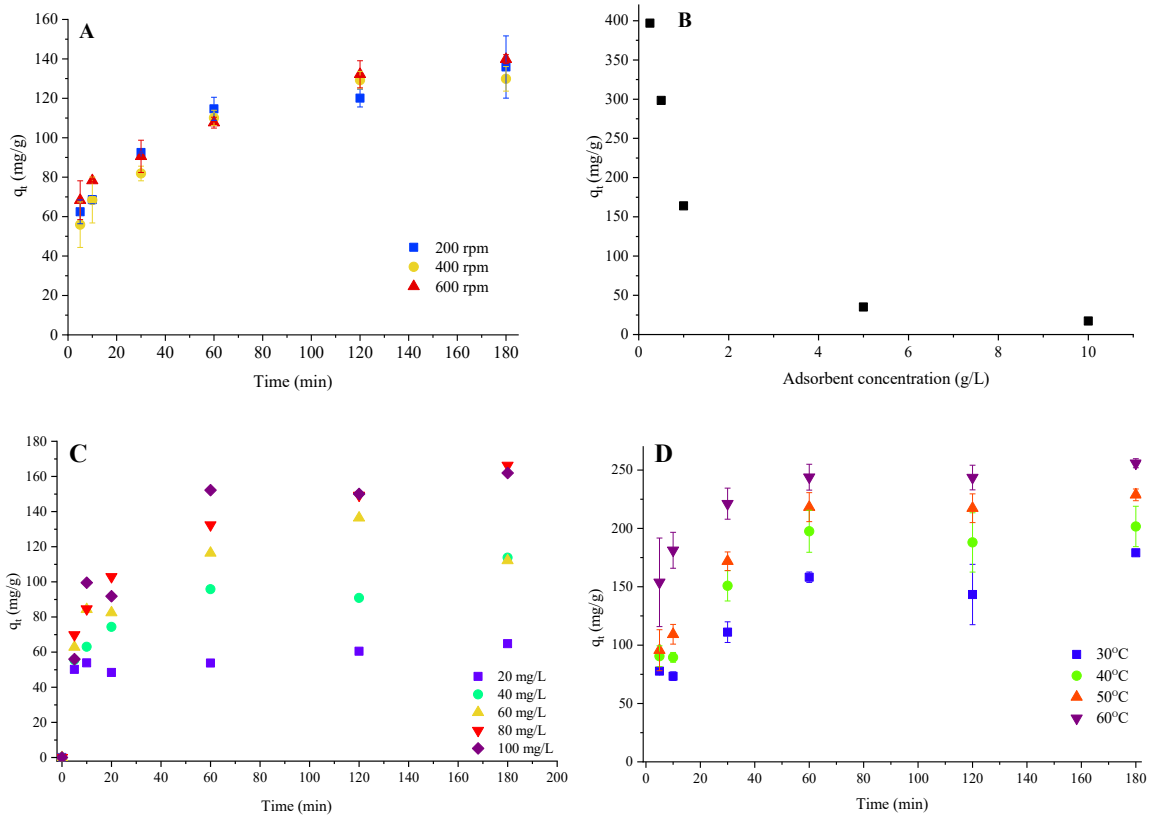

Fig. 22 Effect of the stirring rate (A), adsorbent dose (B), initial dye concentration (C) and temperature (D) on the adsorbed amount of BV14 on sodalite at ambient temperature. In the experiments the initial dye concentration was 60 mg/L and the adsorbent concentration was 250 mg/L, unless it was marked otherwise [124].

The amount of adsorbed Basic Violet 14 per unit of mass of samples in given time at room temperature are presented in **Fig. 23**. The maximum adsorbed quantities on SOD, zeolite and activated carbon are 110 mg g^{-1}, 30 mg g^{-1}, and 180 mg g^{-1}, respectively. Activated carbon, according to its well-known high specific surface area, probably has more binding sites available, therefore, it was not a surprise the great adsorption capacity of this solid. On the other hand, the specific surface area does not explain the lower adsorption capacity of the zeolite compared to the sodalite. Specifically, despite the ~30-fold smaller specific surface area of SOD, it can still bind 3–4 times more BV14 molecules at the same adsorbent concentration of 250 mg L^{-1}. Assumably, sodalite has some properties which promote the adsorption of the dye

molecules, opposed to the zeolite. Moreover, comparing the adsorption rates of these two solids, zeolite reaches the maximum after 30 minutes, while equilibrium in the case of sodalite is not yet reached even after 3 hours.

The study of these two shows that not only the untreated adsorbents but also the thermally activated solids (at 150 °C for 3 hours) result in similar outcome. The thus obtained adsorbents do not have better adsorption capacities (taking the experimental uncertainties into account), even though, based on the thermogravimetric measurements, the thermal treatment leads to a significant degree of dehydration for both solids. This is in line with the fact that these water molecules are situated in the zeolite cages, therefore they are expected to have little effect on surface adsorption.

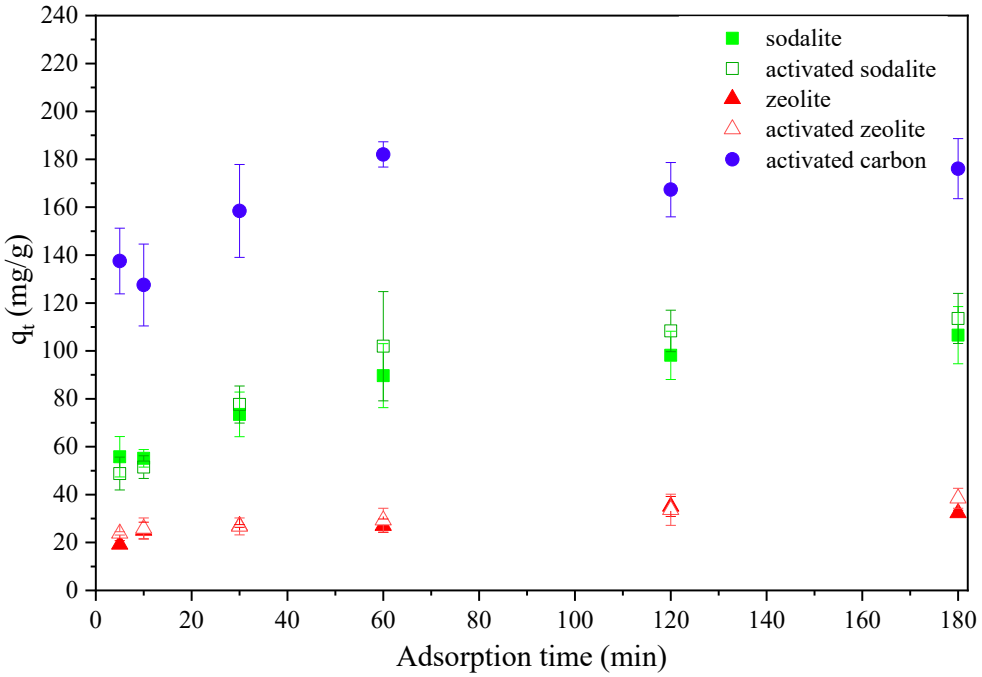

Fig. 23 Adsorbed quantity of Basic Violet 14 on different adsorbents at room temperature. The initial adsorbent and BV14 concentrations were 250 mg/L and 60 mg/L, respectively [124].

Having the time-dependence of the adsorption of the sodalite and the zeolite characterized, we now turn to the analysis of dye adsorption in equilibrium. To this end, we measured the adsorption isotherm of the two adsorbents by mixing suspensions with 250 mg L^{-1} adsorbent with 24-hour contact time and varying dye concentration between 5–100 mg L^{-1}. All samples were at room temperature for 24 hours to allow for the attainment of equilibrium. The thus attained adsorbed amount molecules q_{eq}, are shown in **Fig. 24** and the measured data

were modelled with two different adsorption models usually used in dye adsorption studies, namely the Langmuir and Freundlich equations [126].

The thus obtained fits are shown in **Fig. 24**, whereas the fitted parameters are listed in **Table 8**. The two models provide very similar fits based on the R^2 parameter; however, it is rarely used in nonlinear fitting due to its limitations [127]. In **Fig. 24** is seen that the Freundlich equation fails to reproduce the data below $c_{eq} \approx 15$ g L^{-1}. As for the Langmuir model, it provides satisfactory fit in the entire range of c_{eq}, even below 15 g L^{-1}. Therefore, we find the Langmuir model to be the most probable mechanism for BV14 adsorption at the surface of SOD in the concentration range investigated. Regarding the zeolite, the data fall below $q_{eq} = 50$ mg g^{-1} and they are very scattered, see **Fig. 24**, which arises certainly from the uncertainty associated with adsorption experiments at low concentrations. Our data thus cannot be fitted with either of the above models. It is however reasonable to assume that the average of the q_{eq} values gives us the estimated maximum adsorption capacity, q_L, for which we obtain (31±11) g L^{-1}, which agrees well with the maximum value found from the time-dependence of $c_{fuchsine} = 60$ mg L^{-1}.

Table 8 Results of the Langmuir and Freundlich models fitting on the experimental data of maximum amount of adsorbed Basic Violet 14 (q_{eq} in mg g^{-1}) as a function of its equilibrium concentration (c_{eq} in mg L^{-1}), for sodalite as adsorbent. Shown are the fitted parameters and their standard error of the fit [124].

Adsorption model	Equation*	Fitted parameters
Langmuir	$q_{eq} = q_L \frac{K_L c_{eq}}{1 + K_L c_{eq}}$	q_L = (261±17) mg g^{-1} K_L = (0.053±0.011) L mg^{-1}
Freundlich	$q_{eq} = K_F {c_{eq}}^{1/n}$	K_F = (41.4±6.9) mg g^{-1} n = 2.56±0.30

*q_L, K_L, and K_F are adjustable parameters. In addition, K_L is the Langmuir equilibrium constant of adsorption, q_L is the maximum binding capacity of the adsorbent.

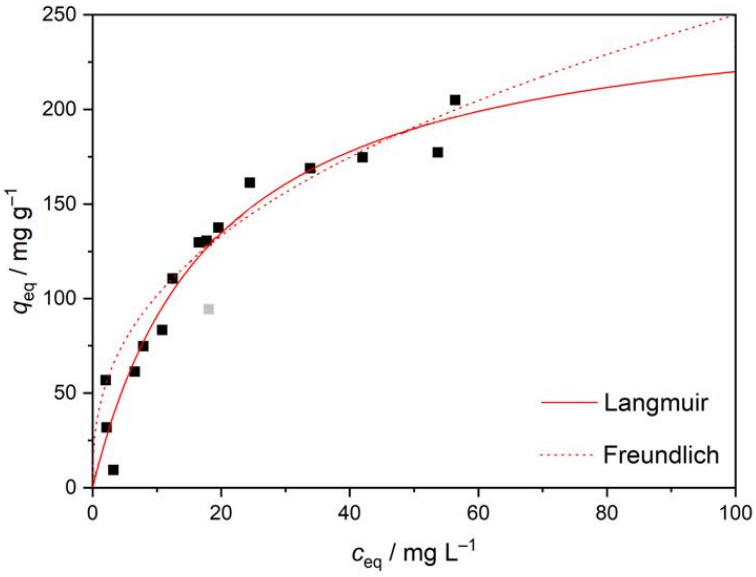

Fig. 24 Equilibrium adsorbed dye mass, q_{eq}, as a function of equilibrium dye concentration, c_{eq}. The initial DSP adsorbent and dye concentrations were 250 mg L^{-1} and 5–100 mg L^{-1}, respectively. All samples were stirred at room temperature for 1 day before filtration. Black squares depict experimental values of q_{eq}, whereas red lines are the results of fitting different adsorption models to the data. The grey symbol stands data omitted during fitting [124].

Comparing the adsorption capacities of the sodalite and the zeolite, it is noticeable that the sodalite has a q_L extremely higher than that of zeolite, despite the 28-fold higher specific surface area of the latter (**Table 7**), suggesting that q_L is not correlated with the SSA. A possible explanation can be that while q_L reports only on the adsorption of dye molecules at the surface of the adsorbent, the N_2 molecules are adsorbed to both the top layer and the interior surfaces due to their smaller sizes, during the experimental determination of the SSA. The diameter of BV14 (12.4 Å) [60] is greater than the pores of the adsorbents (see **Table 7**), thus the dye molecules cannot penetrate into the solid, therefore the inside area does not play a role in the adsorption process. This hypothesis was supported by the calculated absorption Gibbs free energies and the results of the computational modelling, both implicating a considerably stronger adsorption capacity for sodalite compared to zeolite. They also reflect on the preferable chemical composition of the surface of the sodalite, hence the increased Al-content of the zeolite weakens the adsorption of the dye while for SOD the 1:1 Al:Si composition enhances it. These calculations have been explained in the manuscript [124], here they will be not discussed in detail because these are not part of my doctoral work. On the other hand, this outcome makes the whole study complete, thus it was worth to mention it here.

6.7 Sodalite formation in presence of various organics

While sodalite has demonstrated promising potential as an adsorbent for Basic Violet 14 (BV14), it has also become evident that even minor variations in synthesis conditions can substantially influence its performance. Therefore, it is crucial to consider that sodalite formation may be affected not only by inorganic ions but also by various organic compounds—either anthropogenic in origin or derived from sedimentological sources [128-130]. To explore this in greater detail, a range of organic substances—including nonionic, anionic, and cationic species with varying carbon chain lengths—were introduced into the aluminate solution. The objective was to examine how these additives might alter the rate of sodalite crystallization, the physicochemical properties of the resulting materials, and their subsequent adsorption capacities. **Fig. 25** presents the sodalite formation rate in the presence of the different organic additives. Although the position of the crystallization maxima remained unchanged, certain additives increased the maximum silica concentration in solution by approximately 1 g/L, suggesting a slight inhibition of sodalite formation, likely through temporary stabilization of dissolved silica species.

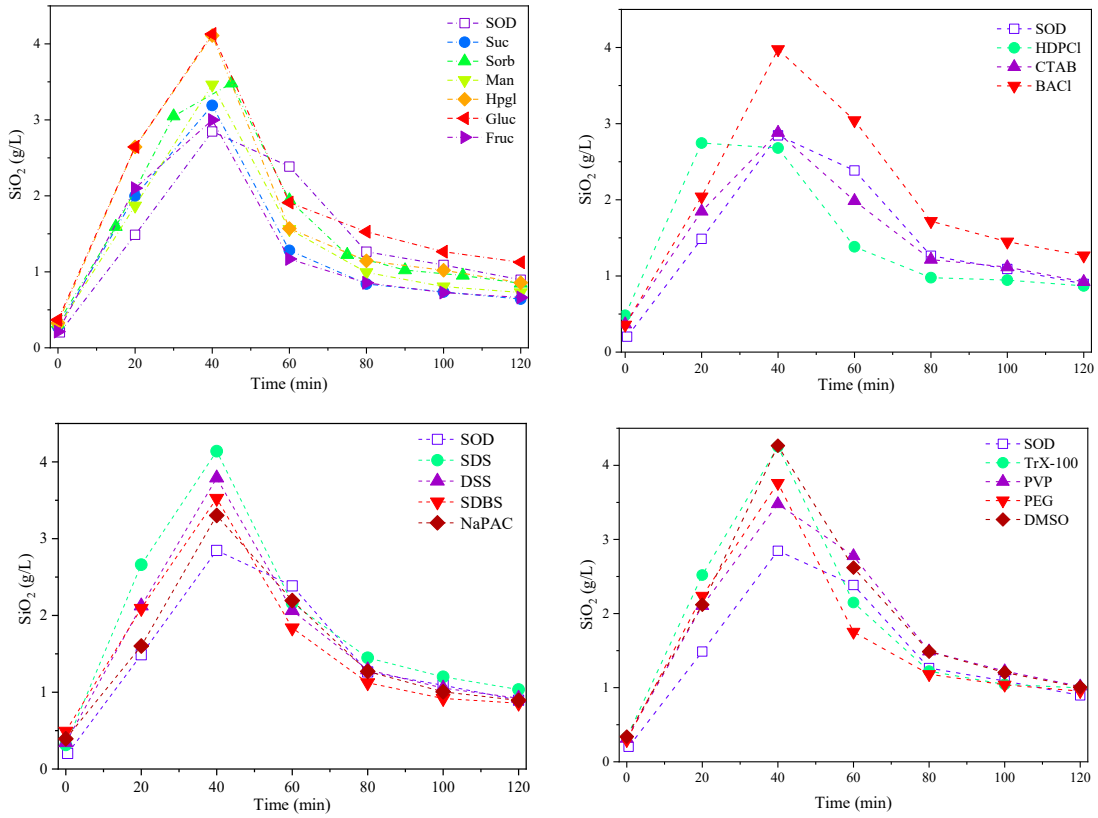

Fig. 25 The dissolution of the kaolinites in presence of different organic additives representing impurities present in bauxite, followed by the precipitation of the sodalite. Experimental conditions: $[NaOH]_T$ = 4.5 M, $[Al(III)]_T$ = 1.9 M, $[Na_2SO_4]_T$ = 0.05 M, $[Na_2CO_3]_T$ = 0.22 M, added kaolinite: 23 g L^{-1}, T = 95 ± 0.5°C. The impurities present in the liquor are shown in the figure above [124].

Comprehensive physicochemical analyses revealed that sodalite was the primary crystalline phase formed in all cases, with its characteristic lepispherical morphology preserved across the different conditions. However, particle size varied significantly depending on the additive used (**Fig. 26**). For instance, sodium dodecylbenzene sulfonate (SDBS) increased particle size by approximately 7 nm, whereas dimethyl sulfoxide (DMSO) led to a reduction of around 4 nm. Importantly, most organic compounds appeared to undergo partial decomposition during synthesis, thus their molecular size did not correlate directly with the pore size of the resulting products.

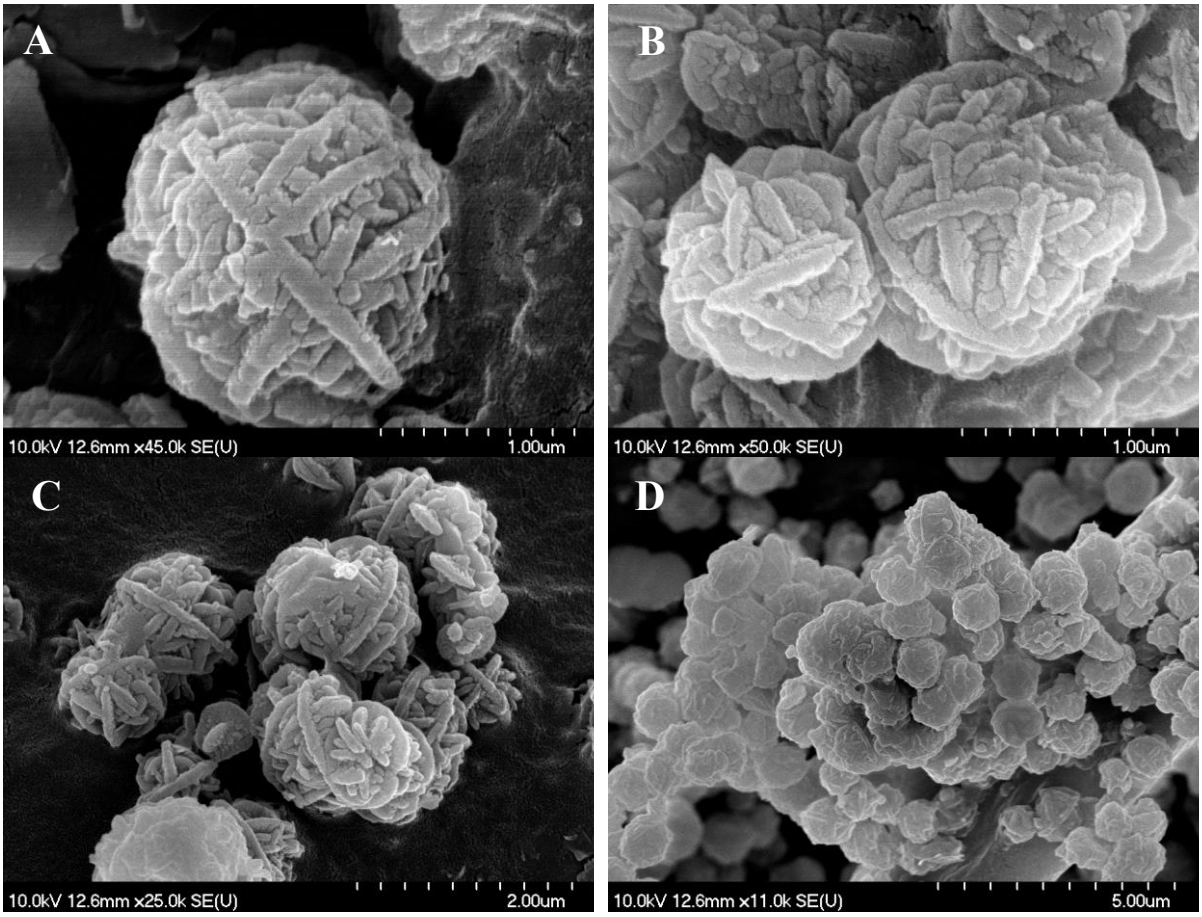

Fig. 26. SEM pictures of sodalite synthesized in the presence of (A) Fruc, (B) DMSO, (C) CTAB, (D) HDPCl. All samples show the lepispherical structure typical of sodalites [124].

Nonetheless, the presence of organic additives exerted a discernible influence on the textural properties of the sodalite. In some cases, increased pore size was observed in conjunction with a reduction in specific surface area, a change likely attributable to morphological alterations during crystallization. Based on nitrogen sorption data, cationic additives appeared to have a particularly pronounced impact on porosity (**SI.4).** Interestingly,

while some additives led to a reduction in specific surface area, they also enhanced the dye adsorption capacity of the material (**Fig. 27**). However, no clear correlation was observed between porosity, carbon content, and adsorption performance. Cationic organics generally improved the dye uptake, whereas sugar-type compounds and anionic surfactants resulted in a marked decrease—often by 20–30 mg/g—in BV14 adsorption. These findings suggest that electrostatic interactions may play a pivotal role in the adsorption mechanism. According to Ba Mohammed et al., favourable adsorption can be attributed to the electrostatic attraction between cationic BV14 molecules and deprotonated silanol groups on the sodalite surface. Furthermore, anionic additives—some of which, based on TOC measurements, may have been incorporated into the sodalite structure—could amplify this electrostatic effect and even introduce additional binding sites, thereby resulting in enhanced dye uptake (by 20–40 mg/g) compared to the unmodified desilication product.

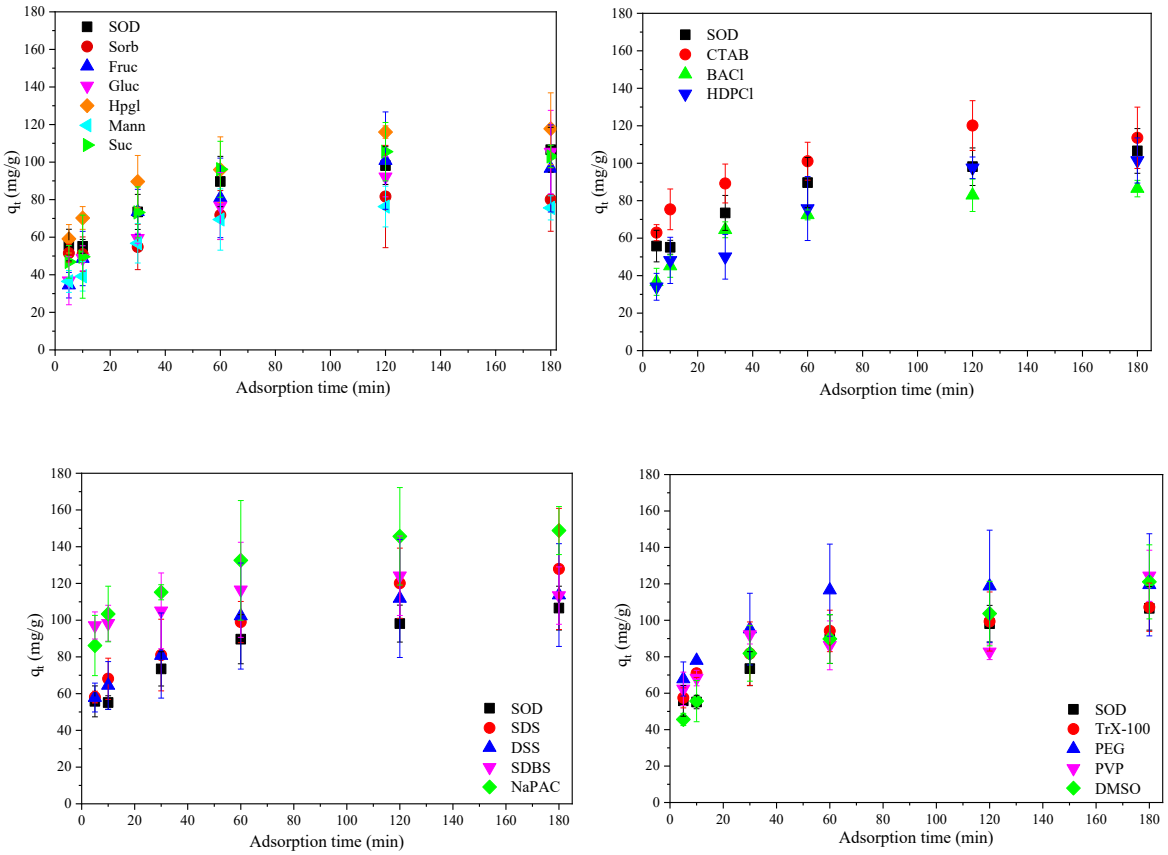

Fig. 27 The adsorbed quantity of BV14 on the desilication products formed in presence of various organic additives. The measurements were carried out at room temperature, with 250 mg/L and 60 mg/L initial adsorbent and dye concentrations, respectively [124].

6.8 Limitations of the sodalite studies and future considerations

Despite the promising findings, this study has certain limitations. A full evaluation of the adsorption efficiency of untreated sodalite across a wide range of adsorbates would take an impractically long time—possibly even a lifetime. This becomes even more complicated when considering the many possible treatment methods, each of which could significantly change the physical and chemical properties of sodalite, and therefore its adsorption performance.

Sodalite, a common mineral phase found in bauxite residue (red mud), forms naturally during the Bayer process. Its composition largely depends on the geochemical and sedimentological characteristics of the original bauxite ore. Because of this, there can be noticeable differences in sodalite composition from one mining site to another due to natural geological variation. For example, changes in the silica, sodium, and alumina content of the ore can directly affect the structure and composition of the resulting sodalite. On top of that, human factors—such as processing conditions, temperatures, and chemical concentrations—can also lead to further variation.

Because of this complexity, it's not realistic to include all of these natural and artificial variables in one single study. For that reason, this research focuses only on untreated sodalite produced under specific conditions, without exploring how its properties might change after different treatments. In addition, another important topic for future research is the potential for reusing sodalite as an adsorbent, especially in systems with continuous flow. Studies should look into how well it performs over time, whether it can be regenerated, and how stable it is during repeated use.

6.9 Characterization of the tricalcium aluminate hexahydrate

According to Litwinek and Madej, the precursors involved in hydration can significantly influence the resulting solids' properties—affecting factors such as morphology, particle size, and thermal stability [131]. Consequently, a detailed comparative analysis is warranted between the two distinctly synthesized tricalcium aluminate hydrates examined in this study: the reference TCA and the Bayer-derived TCA (see **chapter 5.4**).

Powder X-ray diffractograms (**Fig. 28A**), showed no discernible differences between the two samples, both matching the JCPDS card no. 98-006-2704. Peak positions and intensities were identical, with the most intense reflection observed at $2\theta = 39.21°$. While the diffractograms displayed no clear reflections of secondary phases, further calculations

suggested the presence of impurities constituting less than 2 wt%. One possible source of this could be residual CaO, which would elevate the overall calcium content. Additionally, a faint peak at 11.5° 2θ points to the formation of a layered double hydroxide (LDH), specifically $Ca_2Al(OH)_7 \cdot 3H_2O$ (JCPDS card no. 33-0255), which is a known intermediate in oxide hydration [132, 133]. Based on the XRD findings, the FT-IR spectra (**Fig. 28B**) further confirm the compositional similarity between the two samples and provide insights into molecular-level structures. Both the peak positions and intensities were consistent across the samples. Characteristic internal and external M–OH stretching vibrations appeared near 3657 cm^{-1}, while symmetric and asymmetric M–O absorption bands were observed around 790 cm^{-1}. Minor signals at ~1390 and 1510 cm^{-1}, attributable to surface-adsorbed carbonates, suggest that CO_2 exclusion during synthesis was incomplete, with Bayer TCA retaining slightly more carbonate. Additionally, the weak bands around 1660 cm^{-1} indicate the presence of crystal water in both samples.

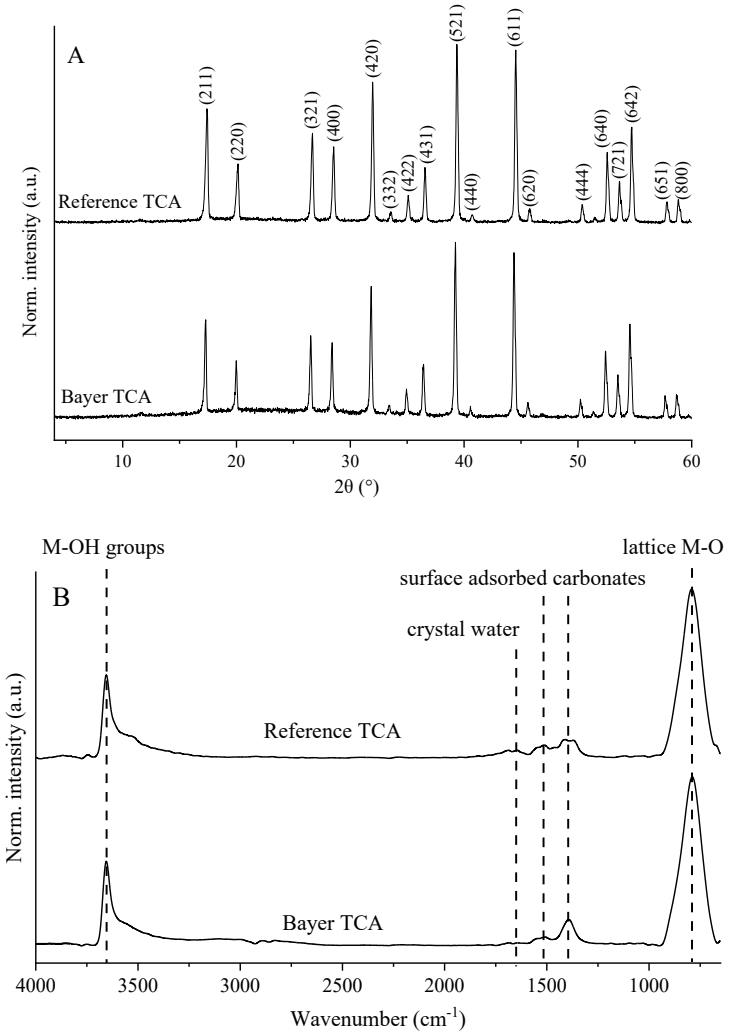

Fig. 28 The X-ray diffractogram (A) and infrared spectra (B) of the differently synthesized tricalcium-aluminate hydrates. Measured values were normalized such that the highest value is unity [134].

The thermal properties of both hydrates were remarkably similar (**SI.5**). Differential thermogravimetric (DTG) analysis showed three endothermic events: (1) loss of physisorbed water below 150 °C, (2) structural hydroxyl group release up to 1000 °C, with DTG minima at 320 °C for the reference TCA and 335 °C for Bayer TCA. Total mass losses of 28.16% and 28.36%, respectively, confirm the same empirical formula: $Ca_3Al_2(OH)_{12}\cdot 0.11H_2O$. SEM images (**Fig. 29**) revealed a clear difference in particle size and crystallinity. Bayer TCA appeared more crystalline with larger particle sizes compared to the reference TCA. The latter's smaller particles likely result from pre-milling before calcination, a known method for reducing particle size [96]. Despite morphological variation, both samples displayed the characteristic hexagonal particle structure typical of tricalcium aluminate hydrates.

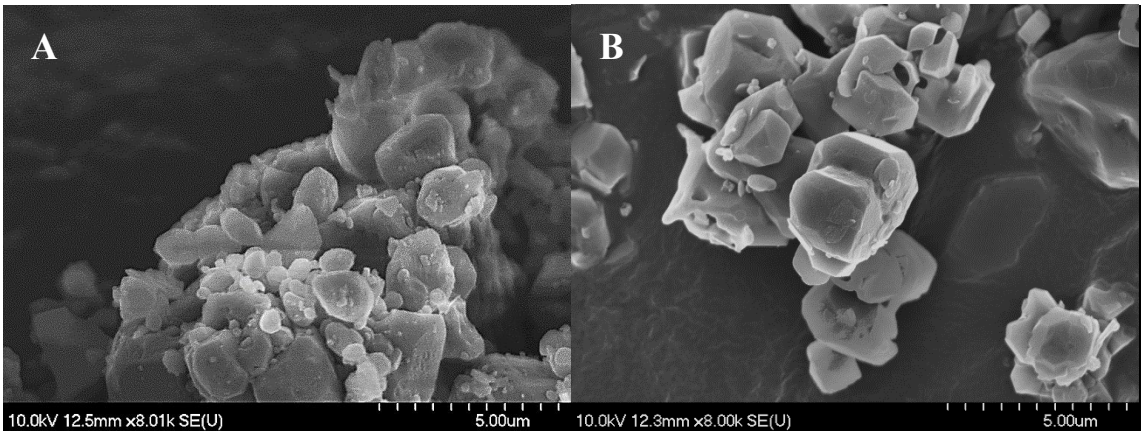

Fig. 29 SEM image of the reference (A) and the Bayer TCA (B), having visibly different particle sizes probably due to the milling of the reference TCA during preparation [134].

6.10 Neutralization of the tricalcium aluminate hexahydrate

Having analysed the physical and chemical characteristics of the tricalcium aluminate hydrates, we now turn our attention to their reactivity, focusing specifically on their interaction with hydrochloric acid.

Preliminary data and literature sources [135] suggest that tricalcium aluminate hydrates react rapidly with aqueous HCl. pH variation curves (**Fig. 30**) show that after a 2-hour equilibration (or 5-hour batch experiment waiting period), the suspensions begin at pH ≈ 12 and gradually decline to pH 10.8 following HCl addition (equivalent to 30 cm^3 of 1 M titrant). Interestingly, the reaction proceeds more rapidly in NaCl solution than in distilled water. This acceleration may be due to enhanced ionic strength promoting dissociation, or potentially a quantum tunneling-like effect associated with sodium ions.

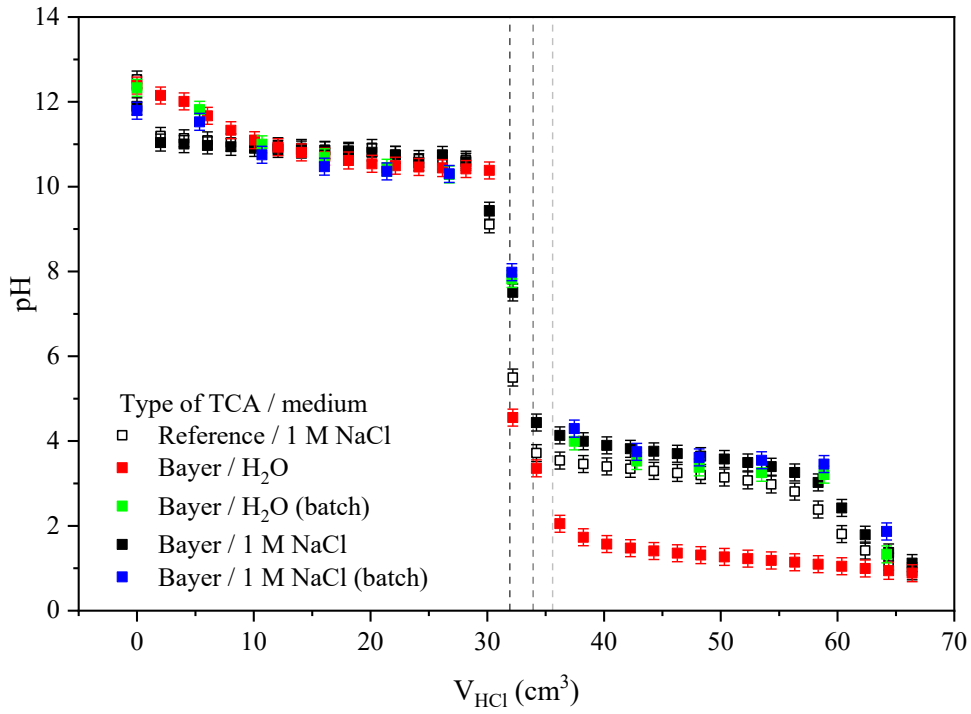

Fig. 30 Titration curves of HCl in suspensions of the reference or Bayer TCA in different medium (NaCl or H_2O: initial mass concentration of 100 g/L and volume of 20 mL; the concentration of HCl was 0.99 M), measured via either potentiometric titrations or separate batch experiments. The first vertical dashed line represents the calculated equivalence point, corresponding to 6 equivalent titrant, then the next lines corresponds to the next calculated theoretical pH at given titrant amount added [134].

To gain deeper insight into the reaction mechanism between hydrochloric acid and tricalcium aluminate hydrate, a series of batch experiments were conducted. Following the addition of HCl, the suspensions were filtered, washed with distilled water, and dried overnight under a nitrogen atmosphere. Subsequent XRD analysis (**Fig. 31A**) revealed that, at approximately pH 10.4—corresponding to the presence of one equivalent of HCl—the tricalcium aluminate hydrate undergoes a distinct phase transformation, forming hydrocalumite (CaAl-layered double hydroxide, or CaAl-LDH). As the pH decreases further, particularly below 7 ($V_{HCl} > 35$ mL), the solid exhibits substantial structural amorphization, resulting in the formation of predominantly amorphous phases such as $Al(OH)_3$ and AlOOH. These observations were reproducible not only in 1 M NaCl solution but also in distilled water, where the amorphous phases appeared even more prominently (**Fig. 31B**).

Results suggest that any $Al(OH)_4^-$ ions released into solution readily reprecipitate as solid $Al(OH)_3$. Interestingly, the solubility pattern changes in the acidic region, implying the coexistence of hydrocalumite alongside $Al(OH)_3$ (**Eq.7**), as indicated by XRD.

$$Al(OH)_4^-(aq) \rightleftharpoons Al(OH)_3(s) + OH^-(aq) \quad (7)$$

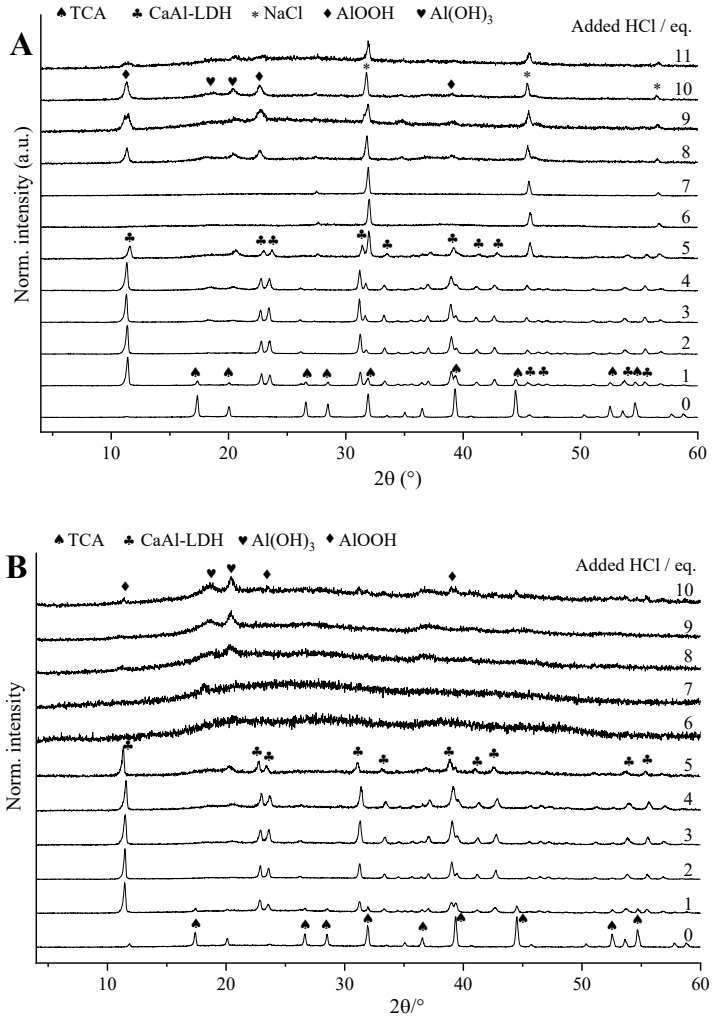

Fig. 31 Powder XRD traces of the solids during the neutralization process in 1 M NaCl solution (A) and in H_2O (B). Traces of powder XRD of Bayer TCA after adding different equivalents of HCl to a 100 g/L suspension in 1 M NaCl (A) or distilled water (B). Symbols show new phases forming upon neutralization. Measured data were normalized such that the highest value is unity [134].

Based on these experimental results and in alignment with previous work by Rosenberg et al.[136], Kirwan et al. [137], and Gácsi et al. [138], we propose the following mechanism for the neutralization of tricalcium aluminate hydrate by hydrochloric acid. Upon dissolution, the initial solid $Ca_3Al_2(OH)_{12}$ breaks down into Ca^{2+}, $Al(OH)_4^-$, $Ca_2Al(OH)_6^+$, and hydroxide ions (Eq. 8). The $Ca_2Al(OH)_6^+$ species then reacts with an anion X^-, resulting in the formation of

$Ca_2Al(OH)_6X$ (Eq. 9). Alternatively, a reaction pathway involving $Ca(OH)_2$, $Al(OH)_4^-$, and X^- leads to the same product, also generating OH^- (Eq. 10). Finally, this LDH compound remains in dynamic equilibrium with its dissociated ionic components (Eq. 11). In these reactions, X^- represents the interlayer charge-compensating anion.:

$$Ca_3Al_2(OH)_{12}(s) \rightleftharpoons Ca_2Al(OH)_6^+(aq) + Al(OH)_4^-(aq) + Ca^{2+}(aq) + 2\ OH^-(aq) \quad (8)$$

$$Ca_2Al(OH)_6^+(aq) + X^-(aq) \rightleftharpoons Ca_2Al(OH)_6X(s) \quad (9)$$

$$2\ Ca(OH)_2(s) + Al(OH)_4^- + X^-(aq) \rightleftharpoons Ca_2Al(OH)_6X(s) + 2\ OH^-(aq) \quad (10)$$

$$Ca_2Al(OH)_6X(s) \rightleftharpoons Ca_2Al(OH)_6^+(aq) + X^-(aq) \rightleftharpoons Al(OH)_4^- + 2\ Ca^{2+} + 3\ OH^- + X^- \quad (11)$$

To confirm the identity of this anion, SEM-EDX analysis was performed on the neutralized solids (**Table 9**). The results show a gradual decrease in the Ca/Al atomic ratio with increasing acid concentration, indicating partial dissolution of Ca^{2+}. Moreover, the presence of chloride in the solids confirms that Cl^- acts as the interlayer anion in the LDH structure formed during neutralization. This conclusion is further validated by additional experiments involving other acids such as HNO_3 and $HClO_4$. Regardless of the acid used, CaAl-LDH forms consistently at pH ≈ 10.4, with XRD patterns indicating that the incorporated anion matches that of the corresponding acid, thereby supporting the proposed mechanism (**SI. 6**).

Table 9 The atomic ratio of the Ca, Al and Cl in the solids after acid addition, measured by SEM–EDX [134].

V_{HCl} (cm^3)	Ca at. %	Al at. %	Cl at. %	Ca/Al	Err. (%)	Ca/Cl	Err. (%)
5.35	44.7	35.7	19.5	1.3	0.1	2.2	0.2
10.70	46.2	32.6	21.2	1.4	0.2	2.2	0.2
21.40	33.2	51.3	14.6	0.65	0.1	2.3	0.2
48.15	7.9	67.8	24.3	0.12	0.01	2.8	0.4

To evaluate the kinetics of the hydrocalumite formation, time-resolved XRD measurements (**Fig. 32**) were carried out following the addition of four equivalents of HCl (21.40 mL) to the suspension. The samples were stirred for varying durations between 20 and 120 minutes. The results indicate that the transformation from TCA to hydrocalumite occurs rapidly, with the phase change being nearly complete within 20 minutes, regardless of whether the medium is distilled water or NaCl solution.

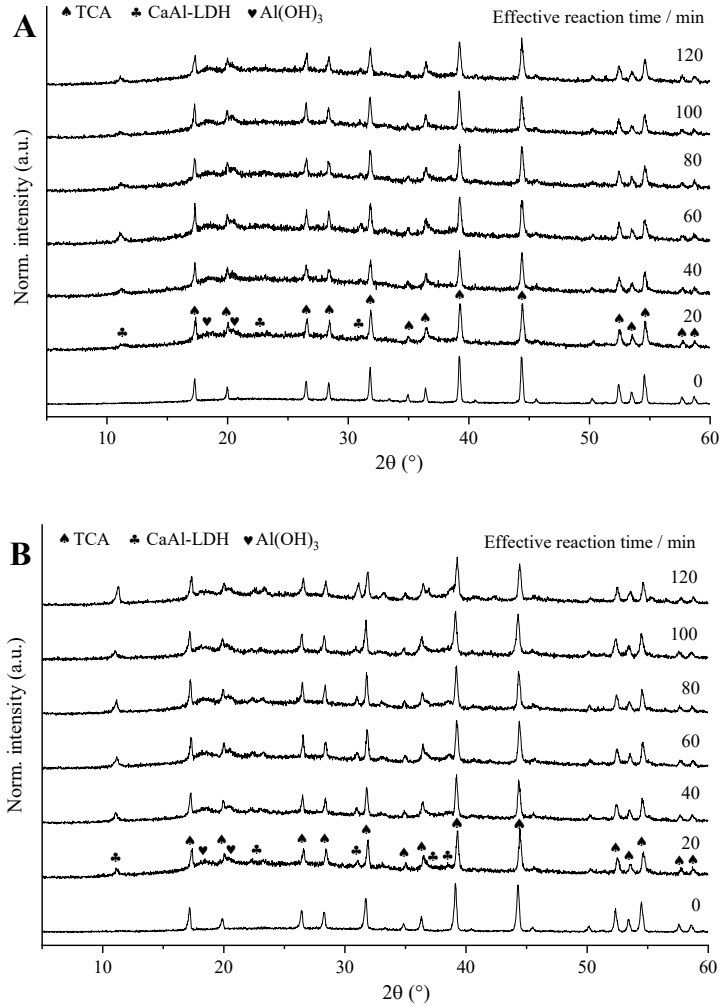

Fig. 32 Powder XRD traces of the solids after different reaction time in H_2O (A) and in 1 M NaCl solution (B). Symbols show new phases forming upon neutralization. Measured data were normalized such that the highest value is unity [134].

This investigation focused solely on the tricalcium aluminate hydrate component of bauxite residue. For a comprehensive understanding of neutralization behaviour, further studies should address additional components—both individually and in mixtures. Notably, matrix effects from iron-rich phases may significantly alter reactivity and slow acid neutralization rates. These aspects warrant systematic exploration in future work.

7. CONCLUSIONS AND PERSPECTIVES

In the first part, the dissolution kinetics of as-received, mechanochemically and/or thermally treated kaolinites were studied in industrial spent liquor, an alkaline sodium aluminate solution typical to Bayer desilication. From industrial point of view, the physico-chemical properties of the mined kaolinite, component of the bauxite, proved to be essential, hence the silica concentration of the spent liquor in given time depends on the kaolinite dissolution and sodalite formation rate. For instance, the mechanochemical treatments could enhance reaction kinetics by augmenting the accessible surface area and the quantity of the acid sites, thereby facilitating the dissolution reaction between aluminium and silicon cations and hydroxide anions, thus accelerate the solubility of kaolinites. The experimental data indicates that the primary drivers of these physico-chemical modifications are the fragmentation and delamination of solid particles, coupled with the generation of structural defects during amorphization. Furthermore, the contribution of Al/Si−OH moiety dehydroxylation to these changes appears to be comparatively major.

Moreover, the characteristics of the formed sodalite proved to be influenced by the starting material and the presence of the impurities in the aluminate solution. Sodalite was synthesized in presence of a wide range of organic impurities of Bayer solutions and their adsorption characteristics were studied concerning Basic Violet 14. Sodalites showed no significant differences in terms of their X-ray diffractograms, infrared spectra, morphology and elemental composition. But they differed markedly in their SSA, which suggested strong correlation to the total organic content either bound to the surface or located in the pores of the sodalite framework (or both). Based on this study, there is no clear dependence of the adsorbed dye quantity, and the organic impurities present during sodalite formation. Comparing the adsorption properties of sodalite to zeolite, we observed 3–4 times higher amount of adsorbed BV14 for SOD, despite its much smaller SSA. As a conclusion, the adsorption capacity did not correlate to the specific surface area of the adsorbents, possibly because of the size of the dye molecules compared to the difference between the sizes of the zeolite and the sodalite.

The last part of the dissertation details the synthesis of high-purity tricalcium-aluminate hydrate, under conditions typical to the aluminium industry. A comparative analysis of this synthesized TCA with a sample produced via a conventional method revealed no statistically significant differences in their fundamental characteristics. Consequently, their dissolution behaviours in a 1 M NaCl solution and in H_2O were also found to be equivalent. Furthermore,

the reaction mechanism between 1 M HCl and the TCA was studied, proposing a novel mechanism. The experimental results demonstrate that following the dissolution of TCA, hydrocalumite (LDH) formation is observed with increasing acid concentration. Subsequently, at pH = 7, aluminium hydroxide becomes the sole solid phase.

Due to the complexity of the work, certain topics were only touched upon in this dissertation. We aimed to highlight the potential inherent in this field, without claiming to be exhaustive. Examples include the utilization of sodalite as an adsorbent, or the opportunities presented by neutralized bauxite residue in the construction industry. However, this thesis would never have been completed if we had pursued a comprehensive study that addressed every detail and satisfied our curiosity. The number of potential avenues within this field is infinite, and although many unanswered questions remained, it is our hope that the number of answers will eventually surpass the number of questions. We also hope that this work will contribute to the advancement of greener industrial practices over time.

8. MAGYAR NYELVŰ ÖSSZEFOGLALÓ

A disszertáció első részében kezeletlen, mechanokémiailag és/vagy termikusan kezelt kaolinitok oldódási kinetikáját vizsgáltuk ipari a Bayer-féle eljárásra jellemző lúgos nátrium-aluminát oldatban. Ipari szempontból a bauxit alkotóelemeként bányászott kaolinit fizik-kémiai tulajdonságai kulcsfontosságúak, mivel a kioldódott szilícium koncentrációja adott idő alatt a kaolinit oldódásának és a szodalit képződésének sebességétől függ. A mechanokémiai kezelések például növelhetik a reakciókinetikát az elérhető felület és a savas helyek mennyiségének növelésével, ezáltal elősegítve az alumínium- és szilícium kationok, valamint a hidroxid anionok közötti oldódási reakciót, és így felgyorsítva az oldhatóságot. A kísérleti adatok azt mutatják, hogy a fiziko-kémiai módosulások fő hajtóerői a szilárd részecskék fragmentációja és delaminációja, valamint az amorfizáció során keletkező szerkezeti hibák. Továbbá, az Al/Si−OH csoportok dehidroxilezési hozzájárulása ezekhez a változásokhoz viszonylag jelentősnek bizonyult.

Továbbá, a képződött szodalit tulajdonságait a kiindulási anyag és az aluminát oldatban lévő szennyeződések jelenléte befolyásolta. A szodalitot szerves szennyezők jelenlétében is szintetizáltunk, és termék adszorpciós jellemzőit vizsgáltuk a Basic Violet 14-re vonatkozóan. A szodalitok röntgendiffrakciós mintázataik, infravörös spektrumaik, morfológiájuk és elemi összetételük tekintetében nem mutattak jelentős különbségeket. Viszont jelentősen eltértek a fajlagos felületükben, ami erős összefüggésre utal a teljes szervesanyag tartalommal, akár a felülethez kötött, akár a szodalit váz pórusaiban elhelyezkedő (vagy mindkettő) szerves anyag mennyiségével. A tanulmányaink alapján nincs egyértelmű összefüggés az adszorbeált festék mennyisége és a szodalit képződése során jelen lévő szerves szennyeződések között. A szodalit adszorpciós tulajdonságait zeolithoz hasonlítva, a szodalit esetében 3-4-szer nagyobb BV14 adszorpciót tapasztaltunk, annak jóval kisebb fajlagos felületének ellenére. Következtetésként, az adszorpciós kapacitás nem korrelált az adszorbensek fajlagos felületével, valószínűleg a festékmolekulák mérete, illetve a zeolit és a szodalit pórusainak mérete közötti különbség miatt.

A disszertáció utolsó része a nagy tisztaságú trikalcium-aluminát-hidrát alumíniumiparra jellemző körülmények között történő szintézisét részletezi. Az így szintetizált TCA és egy hagyományos módszerrel előállított minta összehasonlító elemzése nem mutatott statisztikailag szignifikáns különbségeket alapvető tulajdonságaikban. Ennek következtében az 1 M NaCl oldatban és H_2O-ban mért oldódási viselkedésük is egyenértékűnek bizonyult. Továbbá az 1 M HCl és a TCA közötti reakciómechanizmust is vizsgáltuk, egy új mechanizmust

javasolva. A kísérleti eredmények azt mutatják, hogy a TCA oldódását követően hidrokalumit (LDH) képződés figyelhető meg a növekvő savkoncentrációval. pH=7-nél pedig az alumínium-hidroxid válik az egyetlen szilárd fázissá.

A munka összetettsége miatt bizonyos témákat csak érintettünk a disszertációban. Célunk az volt, hogy rávilágítsunk az ebben a témában rejlő lehetőségekre, anélkül, hogy a teljesség igényével léptünk volna fel. Például, a szodalit adszorbensként való felhasználása, vagy a semlegesített bauxit maradék építőiparban rejlő lehetőségei. Ez a dolgozat azonban soha nem készült volna el, ha minden részletre kiterjedő, kíváncsiságunkat kielégítő munkát végzünk. A témában rejlő lehetőségek száma végtelen, és bár sok megválaszolatlan kérdés maradt, reméljük, hogy a válaszok száma idővel meghaladja majd a kérdések számát. Reméljük továbbá, hogy ez a munka hozzájárulhat az ipari gyakorlatok zöldítéséhez is.

9. REFERENCES

1. Bayer, K.J., *Process of making alumina*, U.S.P. OFFICE, Editor. 1894.
2. Power, G. and J. Loh, *Organic compounds in the processing of lateritic bauxites to alumina.* Hydrometallurgy, 2010. **105**(1-2): p. 1-29.
3. Power, G., et al., *A review of the determination of organic compounds in Bayer process liquors.* Anal Chim Acta, 2011. **689**(1): p. 8-21.
4. Power, G., J.S.C. Loh, and C. Vernon, *Organic compounds in the processing of lateritic bauxites to alumina Part 2: Effects of organics in the Bayer process.* Hydrometallurgy, 2012. **127-128**: p. 125-149.
5. Vogrin, J., et al., *The Influence of Sodium Sulphate on Sodium Aluminosilicate Solubility in Bayer Liquor.* Hydrometallurgy, 2023. **219**: p. 106079.
6. Vogrin, J., et al., *The anion effect on sodium aluminosilicates formed under Bayer process digestion conditions.* Hydrometallurgy, 2020. **192**: p. 105236.
7. Gomes, J.F., et al., *The formation of desilication products in the presence of kaolinite and halloysite – The role of surface area.* Hydrometallurgy, 2021. **203**: p. 105643.
8. Evans, K., *The History, Challenges, and New Developments in the Management and Use of Bauxite Residue.* Journal of Sustainable Metallurgy, 2016. **2**(4): p. 316-331.
9. Wulf, A., *The Invention of Nature: Alexander Von Humboldt's New World*. 2015: Alfred A. Knopf, Inc.
10. Patil, S.V. and B.N. Thorat, *Mechanical dewatering of red mud.* Separation and Purification Technology, 2022. **294**.
11. Singh, B. and R.J. Gilkes, *Properties of soil kaolinites from south-western Australia.* Journal of Soil Science, 1992. **43**(4): p. 645-667.
12. Zbik, M., *Nanomorphology of Kaolinites: Comparative SEM and AFM Studies.* Clays and Clay Minerals, 1998. **46**(2): p. 153-160.
13. Ross, C.S. and P.F. Kerr, *The Kaolin Minerals.* Journal of the American Ceramic Society, 1930. **13**(3): p. 151-160.
14. Weck, P.F., E. Kim, and C.F. Jove-Colon, *Relationship between crystal structure and thermo-mechanical properties of kaolinite clay: beyond standard density functional theory.* Dalton Trans, 2015. **44**(28): p. 12550-60.
15. Picaro, T., *Red mud processing*, E.P. Office, Editor. 1998.
16. Jenkins, D.H. and H.N. Sinha, *Leaching Kinetics of Bauxite in Hydrochloric Acid.* Mineral Processing and Extractive Metallurgy Review, 1995. **15**(1-4): p. 143-143.
17. Ostap, S., *Control of Silica in the Bayer Process Used for Alumina Production.* Canadian Metallurgical Quarterly, 2013. **25**(2): p. 101-106.
18. Authier-Martin, M., et al., *The mineralogy of bauxite for producing smelter-grade alumina.* Jom, 2001. **53**(12): p. 36-40.
19. Vogrin, J., et al., *The influence of sodium sulphate on sodium aluminosilicate solubility in Bayer liquor aiding the desilication process.* Hydrometallurgy, 2023. **219**.
20. Barnes, M.C., J. Addai-Mensah, and A.R. Gerson, *The kinetics of desilication of synthetic spent Bayer liquor and sodalite crystal growth.* Colloids and Surfaces A: Physicochemical and Engineering Aspects, 1999. **147**(3): p. 283-295.
21. Whittington, B.I., B.L. Fletcher, and C. Talbot, *The effect of reaction conditions on the composition of desilication product (DSP) formed under simulated Bayer conditions.* Hydrometallurgy, 1998. **49**: p. 1-22.
22. Jayaweera, L.D., *The effect of organic impurities on the precipitation of alumina trihydrate in the Bayer process*. 1981, University of New South Wales: Australia.
23. Hickman, A.H., et al., *Buxite mineralization in the Darling Range, Western Australia*. 1992: Department of Mines, Western Australia.

24. Kelly, J.L., *A Study of the Influences of Bayer Process Impurities on the Crystallization of Alumina Trihydrate*, in *Department of Chemical Engineering*. 1962, Louisiana State University.
25. Cama, J. and J. Ganor, *The effects of organic acids on the dissolution of silicate minerals: A case study of oxalate catalysis of kaolinite dissolution.* Geochimica et Cosmochimica Acta, 2006. **70**(9): p. 2191-2209.
26. Dickson, J.O., et al., *Competitive incorporation of perrhenate and nitrate into sodalite.* Environ Sci Technol, 2014. **48**(21): p. 12851-7.
27. Smith, P., *The processing of high silica bauxites — Review of existing and potential processes.* Hydrometallurgy, 2009. **98**(1-2): p. 162-176.
28. Otieno, S., et al., *Effect of kaolin pre-treatment method and NaOH levels on the structure and properties of kaolin-derived faujasite zeolites.* Materials Advances, 2021. **2**(18): p. 5997-6010.
29. Tian, L., et al., *Insight into the Loading and Release Properties of an Exfoliated Kaolinite/Cellulose Fiber (EXK/CF) Composite as a Carrier for Oxaliplatin Drug: Cytotoxicity and Release Kinetics.* ACS Omega, 2020. **5**(30): p. 19165-19173.
30. Drillet, V. and D. Defives, *Clay Dissolution Kinetics in Relation to Alkaline Flooding*, in *All Days*. 1991.
31. Hu, B., C. Zhang, and X. Zhang, *The Effects of Hydrochloric Acid Pretreatment on Different Types of Clay Minerals.* Minerals, 2022. **12**(9): p. 1167.
32. Balaz, P., *Mechanochemistry in Nanoscience and Minerals Engineering*. 2008: Springer.
33. Juhász, Z., *Mechano-chemical activation of kaolin minerals.* Acta mineralogica-petrographica, 1980. **24**: p. 121-145.
34. Aglietti, E.F., J.M.P. Lopez, and E. Pereira, *Kinetic aspects of kaolinite acid dissolution II. Mineral after mechanochemical treatment.* Reactivity of Solids, 1986. **2**: p. 35-44.
35. Baki, V.A., et al., *The impact of mechanochemical activation on the physicochemical properties and pozzolanic reactivity of kaolinite, muscovite and montmorillonite.* Cement and Concrete Research, 2022. **162**: p. 106962.
36. Mako, E., et al., *Surface modification of mechanochemically activated kaolinites by selective leaching.* J Colloid Interface Sci, 2006. **294**(2): p. 362-70.
37. Moodi, F., A.A. Ramezanianpour, and A.S. Safavizadeh, *Evaluation of the optimal process of thermal activation of kaolins.* Scientia Iranica, 2011. **18**(4): p. 906-912.
38. Brindley, G.W. and M. Nakahira, *The KaoIinite-MuIIite Reaction Series: Ill, The High-Temperature Phases.* Journal of the American Ceramic Society, 1959. **42**(7): p. 319-324.
39. Chakraborty, A.K., *Dehydroxylation Mechanism*, in *Phase Transformation of Kaolinite Clay* 2014. p. 313-322.
40. Artioli, Y., *Adsorption*, in *Encyclopedia of Ecology*. 2008. p. 60-65.
41. Cossu, R., H.-J. Ehrig, and A. Muntoni, *Physical–Chemical Leachate Treatment*, in *Solid Waste Landfilling*. 2018. p. 575-632.
42. Sharma, G., et al., *Activated Carbon as Superadsorbent and Sustainable Material for Diverse Applications.* Adsorption Science & Technology, 2022. **2022**: p. 1-21.
43. Singh, K.P., et al., *Color Removal from Wastewater Using Low-Cost Activated Carbon Derived from Agricultural Waste Material.* Industrial & Engineering Chemistry Research, 2003. **42**(9): p. 1965-1976.
44. Perrich, J.R., *Activated Carbon Adsorption For Wastewater Treatment*. 1981: CRC Press.
45. Pan, B., et al., *Development of polymeric and polymer-based hybrid adsorbents for pollutants removal from waters.* Chemical Engineering Journal, 2009. **151**(1-3): p. 19-29.

46. Matusiak, J., A. Przekora, and W. Franus, *Zeolites and zeolite imidazolate frameworks on a quest to obtain the ideal biomaterial for biomedical applications: A review.* Materials Today, 2023. **in press**.
47. Chaouati, N., A. Soualah, and M. Chater, *Adsorption of phenol from aqueous solution onto zeolites Y modified by silylation.* Comptes Rendus Chimie, 2013. **16**(3): p. 222-228.
48. P.A. Jacobs, et al., *Introduction to Zeolite Science and Practice*. 2001: Elsevier.
49. Esaifan, M., et al., *Synthesis of Hydroxy-Sodalite/Cancrinite Zeolites from Calcite-Bearing Kaolin for the Removal of Heavy Metal Ions in Aqueous Media.* Minerals, 2019. **9**(8): p. 484-497.
50. Ulfa, M., et al., *Controlling the Size and Porosity of Sodalite Nanoparticles from Indonesian Kaolin for Pb(2+) Removal.* Materials (Basel), 2022. **15**(8): p. 2745-2764.
51. Yu, H., et al., *Preparation, characterization and adsorption properties of sodalite pellets.* Materials Letters, 2014. **132**: p. 259-262.
52. Lellis, B., et al., *Effects of textile dyes on health and the environment and bioremediation potential of living organisms.* Biotechnology Research and Innovation, 2019. **3**(2): p. 275-290.
53. Sivarajasekar, N. and R. Baskar, *Adsorption of basic red 9 on activated waste Gossypium hirsutum seeds: Process modeling, analysis and optimization using statistical design.* Journal of Industrial and Engineering Chemistry, 2014. **20**(5): p. 2699-2709.
54. Khan, S. and A. Malik, *Toxicity evaluation of textile effluents and role of native soil bacterium in biodegradation of a textile dye.* Environ Sci Pollut Res Int, 2018. **25**(5): p. 4446-4458.
55. Wang, C., et al., *Characterization of coal gangue and coal gangue-based sodalite and their adsorption properties for Cd2+ ion and methylene blue from aqueous solution.* Journal of Material Cycles and Waste Management, 2023. **25**(3): p. 1622-1634.
56. Gupta, V.K., et al., *Removal of Rhodamine B, Fast Green, and Methylene Blue from Wastewater Using Red Mud, an Aluminium Industry Waste.* Industrial & Engineering Chemistry Research, 2004. **43**(7): p. 1740-1747.
57. Zhou, L., et al., *Adsorption removal of cationic dyes from aqueous solutions using ceramic adsorbents prepared from industrial waste coal gangue.* J Environ Manage, 2019. **234**: p. 245-252.
58. Alhujaily, A., et al., *Adsorptive removal of anionic dyes from aqueous solutions using spent mushroom waste.* Applied Water Science, 2020. **10**(7): p. 183-195.
59. Fathi, M.R., A. Asfaram, and A. Farhangi, *Removal of Direct Red 23 from aqueous solution using corn stalks: isotherms, kinetics and thermodynamic studies.* Spectrochim Acta A Mol Biomol Spectrosc, 2015. **135**: p. 364-72.
60. Loera-Serna, S., E. Ortiz, and H.I. Beltrán, *First trial and physicochemical studies on the loading of basic fuchsin, crystal violet and Black Eriochrome T on HKUST-1.* New Journal of Chemistry, 2017. **41**(8): p. 3097-3105.
61. Cooksey, C. and A. Dronsfield, *Fuchsine or magenta: the second most famous aniline dye. A short memoir on the 150th anniversary of the first commercial production of this well known dye.* Biotech Histochem, 2009. **84**(4): p. 179-83.
62. K. Manjula Rani, et al., *Adsorptive Removal of Basic Violet Dye from Aqueous Solution by Activated Carbon Prepared From Tea Dust Material.* International Journal of Innovative Research in Science, Engineering and Technology, 2015. **4**(8): p. 6845-6853.
63. Jain, S.N., et al., *Vegetable residue of fenugreek (Trigonella Foenum-Graecum), waste biomass for removal of Basic Violet 14 from wastewater: Kinetic, equilibrium, and reusability studies.* Sustainable Chemistry and Pharmacy, 2020. **16**: p. 100269.

64. Saranya, G., et al., *Equilibrium Uptake and Bioaccumulation of Basic Violet 14 Using Submerged Macrophyte Hydrilla verticillata.* CLEAN - Soil, Air, Water, 2011. **39**(3): p. 283-288.
65. Ba Mohammed, B., et al., *Fe-ZSM-5 zeolite for efficient removal of basic Fuchsin dye from aqueous solutions: Synthesis, characterization and adsorption process optimization using BBD-RSM modeling.* Journal of Environmental Chemical Engineering, 2020. **8**(5): p. 104419.
66. Elkady, M.F., M.R. El-Aassar, and H.S. Hassan, *Adsorption Profile of Basic Dye onto Novel Fabricated Carboxylated Functionalized Co-Polymer Nanofibers.* Polymers (Basel), 2016. **8**(5): p. 177-190.
67. Klauber, C., M. Gräfe, and G. Power, *Bauxite residue issues: II. options for residue utilization.* Hydrometallurgy, 2011. **108**(1-2): p. 11-32.
68. Power, G., M. Gräfe, and C. Klauber, *Bauxite residue issues: I. Current management, disposal and storage practices.* Hydrometallurgy, 2011. **108**(1-2): p. 33-45.
69. Avdibegovic, D., M. Regadio, and K. Binnemans, *Efficient separation of rare earths recovered by a supported ionic liquid from bauxite residue leachate.* RSC Adv, 2018. **8**(22): p. 11886-11893.
70. Lei, Q., et al., *Separation and recovery of scandium and titanium from red mud leaching liquor through a neutralization precipitation-acid leaching approach.* Journal of Rare Earths, 2021. **39**(9): p. 1126-1132.
71. Davris, P., et al., *Selective leaching of rare earth elements from bauxite residue (red mud), using a functionalized hydrophobic ionic liquid.* Hydrometallurgy, 2016. **164**: p. 125-135.
72. Hertel, T., et al., *Boosting the use of bauxite residue (red mud) in cement - Production of an Fe-rich calciumsulfoaluminate-ferrite clinker and characterisation of the hydration.* Cement and Concrete Research, 2021. **145**.
73. Singh, M., S.N. Upadhayay, and P.M. Prasad, *Preparation of Iron Rich Cements Using Red Mud.* Cement and Concrete Research, 1997. **27**(7): p. 1037-1046.
74. Gräfe, M., G. Power, and C. Klauber, *Bauxite residue issues: III. Alkalinity and associated chemistry.* Hydrometallurgy, 2011. **108**(1-2): p. 60-79.
75. Liu, S., et al., *The roles of red mud as desulfurization and denitrification in flue gas: A review.* Journal of Environmental Chemical Engineering, 2023. **11**(3).
76. Pepper, R.A., S.J. Couperthwaite, and G.J. Millar, *Value adding red mud waste: High performance iron oxide adsorbent for removal of fluoride.* Journal of Environmental Chemical Engineering, 2017. **5**(3): p. 2200-2206.
77. Wang, L., et al., *A Review on Comprehensive Utilization of Red Mud and Prospect Analysis.* Minerals, 2019. **9**(6): p. 362-381.
78. Menzies, N.W., I.M. Fulton, and W.J. Morrell, *Seawater neutralization of alkaline bauxite residue and implications for revegetation.* J Environ Qual, 2004. **33**(5): p. 1877-84.
79. Clark, M.W., M. Johnston, and A.J. Reichelt-Brushett, *Comparison of several different neutralisations to a bauxite refinery residue: Potential effectiveness environmental ameliorants.* Applied Geochemistry, 2015. **56**: p. 1-10.
80. Rai, S., K.L. Wasewar, and A. Agnihotri, *Treatment of alumina refinery waste (red mud) through neutralization techniques: A review.* Waste Manag Res, 2017. **35**(6): p. 563-580.
81. Khaitan, S., D.A. Dzombak, and G.V. Lowry, *Chemistry of the Acid Neutralization Capacity of Bauxite Residue.* Environmental Engineering Science, 2009. **26**(5): p. 873-881.

82. Dilnesa, B.Z., et al., *Synthesis and characterization of hydrogarnet Ca3(AlxFe1−x)2(SiO4)y(OH)4(3−y).* Cement and Concrete Research, 2014. **59**: p. 96-111.
83. Phrompet, C., et al., *Optical and dielectric properties of nano-sized tricalcium aluminate hexahydrate (C3AH6) cement.* Construction and Building Materials, 2018. **179**: p. 57-65.
84. Adhikari, P., C.C. Dharmawardhana, and W.Y. Ching, *Structure and properties of hydrogrossular mineral series.* Journal of the American Ceramic Society, 2017. **100**(9): p. 4317-4330.
85. Majumdar, A.J. and R. Roy, *The System CaO-Al2O3-H2O.* Journal of the American Ceramic Society, 1956. **39**(12): p. 434-442.
86. Alvaro, F., et al., *Performances Assessment of Tricalcium Aluminate as an Innovative Material for Thermal Energy Storage Applications.* Applied Sciences, 2021. **11**(4).
87. Young, J.F., *Effect of Organic Compounds on the Interconversions of Calcium Aluminate Hydrates: Hydration of Tricalcium Aluminate.* Journal of the American Ceramic Society, 1970. **53**(2): p. 65-69.
88. Young, J.F., *Effect of organic compounds on the interconversions of calcium aluminate hydrates. Hydration of monocalcium aluminate.* Cement and Concrete Research, 1971. **1**(1): p. 113-122.
89. França, S.C.A., et al., *Some aspects of tricalcium aluminate hexahydrate formation on the Bayer process*, in *Light Metals* 2010. p. 63-66.
90. Salimi, R. and J. Vaughan, *Crystallisation of tricalcium aluminate from sodium aluminate solution using slaked lime.* Powder Technology, 2016. **294**: p. 472-483.
91. Pan, X., et al., *Formation behaviour of tricalcium aluminate hexahydrate in synthetic sodium aluminate solution with high alkali concentration and caustic ratio.* Hydrometallurgy, 2020. **195**.
92. Whittington, B.I. and C.M. Cardile, *The chemistry of tricalcium aluminate hexahydrate relating to the Bayer industry.* International Journal of Mineral Processing, 1996. **48**(1-2): p. 21-38.
93. Palmer, S.J., R.L. Frost, and M.K. Smith, *Minimising reversion, using seawater and magnesium chloride, caused by the dissolution of tricalcium aluminate hexahydrate.* J Colloid Interface Sci, 2011. **353**(2): p. 398-405.
94. Lyu, F., et al., *Dealkalization processes of bauxite residue: A comprehensive review.* J Hazard Mater, 2021. **403**: p. 123671.
95. Radnai, T., et al., *Structure of Aqueous Sodium Aluminate Solutions: A Solution X-ray Diffraction Study.* The Journal of Physical Chemistry A, 1998. **102**(40): p. 7841-7850.
96. Kása, E., et al., *The dissolution kinetics of raw and mechanochemically treated kaolinites in industrial spent liquor – The effect of the physico-chemical properties of the solids.* Applied Clay Science, 2021. **203**.
97. Wang, T., et al., *Effective removal of zinc (II) from aqueous solutions by tricalcium aluminate (C(3)A).* J Colloid Interface Sci, 2015. **443**: p. 65-71.
98. Yuan, P., et al., *From platy kaolinite to aluminosilicate nanoroll via one-step delamination of kaolinite: Effect of the temperature of intercalation.* Applied Clay Science, 2013. **83-84**: p. 68-76.
99. Wang, J., et al., *Energetics, Interlayer Molecular Structures, and Hydration Mechanisms of Dimethyl Sulfoxide (DMSO)-Kaolinite Nanoclay Guest-Host Interactions.* J Phys Chem Lett, 2021. **12**(40): p. 9973-9981.
100. Frisch, M.J.T., G. W.; Schlegel, H. B.; Scuseria, G. E.; Robb, M. A.; Cheeseman, J. R.; Scalmani, G.; Barone, V.; Petersson, G. A.; Nakatsuji, H.; Li, X.; Caricato, M.; Marenich, A. V.; Bloino, J.; Janesko, B. G.; Gomperts, R.; Mennucci, B.; Hratchian, H.

P.; Ortiz, J. V.; Izmaylov, A. F.; Sonnenberg, J. L.; Williams-Young, D.; Ding, F.; Lipparini, F.; Egidi, F.; Goings, J.; Peng, B.; Petrone, A.; Henderson, T.; Ranasinghe, D.; Zakrzewski, V. G.; Gao, J.; Rega, N.; Zheng, G.; Liang, W.; Hada, M.; Ehara, M.; Toyota, K.; Fukuda, R.; Hasegawa, J.; Ishida, M.; Nakajima, T.; Honda, Y.; Kitao, O.; Nakai, H.; Vreven, T.; Throssell, K.; Montgomery, J. A.; Peralta, J. E.; Ogliaro, F.; Bearpark, M. J.; Heyd, J. J.; Brothers, E. N.; Kudin, K. N.; Staroverov, V. N.; Keith, T. A.; Kobayashi, R.; Normand, J.; Raghavachari, K.; Rendell, A. P.; Burant, J. C.; Iyengar, S. S.; Tomasi, J.; Cossi, M.; Millam, J. M.; Klene, M.; Adamo, C.; Cammi, R.; Ochterski, J. W.; Martin, R. L.; Morokuma, K.; Farkas, O.; Foresman, J. B.; Fox, D. J., *Gaussian16*. 2016, Gaussian, Inc.: Wallingford CT.

101. Chai, J.D. and M. Head-Gordon, *Long-range corrected hybrid density functionals with damped atom-atom dispersion corrections.* Phys Chem Chem Phys, 2008. **10**(44): p. 6615-20.
102. Santra, G., R. Calinsky, and J.M.L. Martin, *Benefits of Range-Separated Hybrid and Double-Hybrid Functionals for a Large and Diverse Data Set of Reaction Energies and Barrier Heights.* J Phys Chem A, 2022. **126**(32): p. 5492-5505.
103. Modrzejewski, M., G. Chalasinski, and M.M. Szczesniak, *Range-Separated meta-GGA Functional Designed for Noncovalent Interactions.* J Chem Theory Comput, 2014. **10**(10): p. 4297-306.
104. Plancon, A., R.F. Giese, and R. Snyder, *The Hinckley index for kaolinites.* Clay Minerals, 1988. **23**: p. 249-260.
105. Balczár, I., et al., *Mechanochemical and thermal activation of kaolin for manufacturing geopolymer mortars – Comparative study.* Ceramics International, 2016. **42**(14): p. 15367-15375.
106. Hamzaoui, R., et al., *Structural and thermal behaviour of proclay kaolinite using high energy ball milling process.* Powder Technology, 2015. **271**: p. 228-237.
107. Kloprogge, J.T., *Spectroscopic Methods in the Study of Kaolin Minerals and Their Modifications*. Springer Mineralogy. 2019.
108. Chakravorty, A.K. and D.K. Ghosh, *Kaolinite–Mullite Reaction Series: The Development and Significance of a Binary Aluminosilicate Phase.* Journal of the American Ceramic Society, 2005. **74**(6): p. 1401-1406.
109. Ptáček, P., et al., *Crystallization of spinel phase from metakaoline: The nonisothermal thermodilatometric CRH study.* Powder Technology, 2013. **243**: p. 40-45.
110. Castelein, O., et al., *The influence of heating rate on the thermal behaviour and mullite formation from a kaolin raw material.* Ceramics International, 2001. **27**(5): p. 517-522.
111. Kása, E., et al., *The effect of mechanical and thermal treatments on the dissolution kinetics of kaolinite in alkaline sodium aluminate solution under conditions typical to Bayer desilication.* Applied Clay Science, 2022. **229**.
112. Rodríguez-González, L., et al., *The acid properties of H-ZSM-5 as studied by NH3-TPD and 27Al-MAS-NMR spectroscopy.* Applied Catalysis A: General, 2007. **328**(2): p. 174-182.
113. Kumar, S., A.K. Panda, and R.K. Singh, *Preparation and Characterization of Acid and Alkaline Treated Kaolin Clay.* Bulletin of Chemical Reaction Engineering & Catalysis, 2013. **8**(1): p. 61-69.
114. López, D., et al., *Metal Oxide Nanoparticles Supported on Macro-Mesoporous Aluminosilicates for Catalytic Steam Gasification of Heavy Oil Fractions for On-Site Upgrading.* Catalysts, 2017. **7**(11).
115. Torres-Luna, J.A. and J.G. Carriazo, *Porous aluminosilicic solids obtained by thermal-acid modification of a commercial kaolinite-type natural clay.* Solid State Sciences, 2019. **88**: p. 29-35.

116. M. AlSawalha, F.R., L. Novikova, L. Bel'chinskaya, *Acidity of different Jordanian Clays characterized by TPD-NH3 and MBOH Conversion.* World Acad. Sci. Eng. Technol., 2011. **5**: p. 7-29.
117. Földvári, M., *Handbook of thermogravimetric system of minerals and its use in geological practice*. Vol. 213. 2011: Geological Institute of Hungary.
118. Pascual, J., et al., *Porous mullite and mullite-based composites by chemical processing of kaolinite and aluminium metal wastes.* Journal of Materials Chemistry, 2000. **10**(6): p. 1409-141.
119. Wu, Y., et al., *Dissolution kinetics and removal mechanism of kaolinite in diasporic bauxite in alkali solution at atmospheric pressure.* Transactions of Nonferrous Metals Society of China, 2019. **29**(12): p. 2627-2637.
120. Peng, H., J. Vaughan, and J. Vogrin, *The effect of thermal activation of kaolinite on its dissolution and re-precipitation as zeolites in alkaline aluminate solution.* Applied Clay Science, 2018. **157**: p. 189-197.
121. Mbey, J.-A., et al., *DMSO Intercalation in Selected Kaolinites: Influence of the Crystallinity.* ChemEngineering, 2020. **4**(4).
122. Albach, B., et al., *An evaluation of modified Kaolinite surface on the crystalline and mechanical behaviour of polypropylene.* Polymer Testing, 2019. **75**: p. 237-245.
123. Pahlevi, N.D., B. Guo, and K. Sasaki, *Immobilization of selenate in cancrinite using a hydrothermal method.* Ceramics International, 2018. **44**(7): p. 8635-8642.
124. Kasa, E., et al., *Utilization of desilication products as efficient adsorbents for the removal of basic fuchsine.* J Hazard Mater, 2024. **480**: p. 136234.
125. Perez-Botella, E., S. Valencia, and F. Rey, *Zeolites in Adsorption Processes: State of the Art and Future Prospects.* Chem Rev, 2022. **122**(24): p. 17647-17695.
126. Dávila-Jiménez, M.M., M.P. Elizalde-González, and A.A. Peláez-Cid, *Adsorption interaction between natural adsorbents and textile dyes in aqueous solution.* Colloids and Surfaces A: Physicochemical and Engineering Aspects, 2005. **254**(1-3): p. 107-114.
127. Spiess, A.N. and N. Neumeyer, *An evaluation of R2 as an inadequate measure for nonlinear models in pharmacological and biochemical research: a Monte Carlo approach.* BMC Pharmacol, 2010. **10**: p. 6.
128. Paramguru, R.K., P.C. Rath, and V.N. Misra, *Trends in Red Mud Utilization – a Review.* Mineral Processing and Extractive Metallurgy Review, 2004. **26**(1): p. 1-29.
129. Wellington, M. and F. Valcin, *Impact of Bayer Process Liquor Impurities on Causticization.* Industrial & Engineering Chemistry Research, 2007. **46**(15): p. 5094-5099.
130. Herrera-Gonzalez, A.M., M. Caldera-Villalobos, and A.A. Pelaez-Cid, *Adsorption of textile dyes using an activated carbon and crosslinked polyvinyl phosphonic acid composite.* J Environ Manage, 2019. **234**: p. 237-244.
131. Litwinek, E. and D. Madej, *Structure, microstructure and thermal stability characterizations of C3AH6 synthesized from different precursors through hydration.* Journal of Thermal Analysis and Calorimetry, 2019. **139**(3): p. 1693-1706.
132. Chi, L., et al., *Layered Double Hydroxides Precursor as Chloride Inhibitor: Synthesis, Characterization, Assessment of Chloride Adsorption Performance.* Materials (Basel), 2018. **11**(12).
133. Zheng, D., et al., *Hydration Characteristics of Tricalcium Aluminate in the Presence of Nano-Silica.* Nanomaterials (Basel), 2021. **11**(1).
134. Kása, E., et al., *The neutralization of tricalcium aluminate hexahydrate and its spontaneous transformation into Friedel's salt, a layered double hydroxide.* Cement and Concrete Research, 2024. **177**.

135. Tadros, M.E., W.Y. Jackson, and J. Skalny, *Study of the dissolution and electrokinetic behaviour of tricalcium aluminate*, in *Hydrosols and Rheology*, M. Kerker, Editor. 1976, Academic Press. p. 211-223.
136. Rosenberg, S.P., D.J. Wilson, and C.A. Heath, *Some Aspects of Calcium Chemistry in the Bayer Process*, in *Essential Readings in Light Metals*. 2016. p. 210-216.
137. Kirwan, L.J., et al., *Chemistry of bauxite residue neutralisation and aspects to implementation.* International Journal of Mineral Processing, 2013. **119**: p. 40-50.
138. Gácsi, A., et al., *Estimation of the solubility product of hydrocalumite–hydroxide, a layered double hydroxide with the formula of [Ca2Al(OH)6]OH·nH2O.* Journal of Physics and Chemistry of Solids, 2016. **98**: p. 167-173.

10. PUBLICATION LIST

Hungarian Scientific Bibliography (MTMT) identifier: 10069343

h-index: 5

Original research articles related to the PhD dissertation:

1. **Eszter Kása**, Ivett Petri, Márton Szabados, Áron Ágoston, András Sápi, Zoltán Kónya, Ákos Kukovecz, András Stirling, Pál Sipos, Bence Kutus, *Utilization of desilication products as efficient adsorbents for the removal of basic fuchsine.* Journal Of Hazardous Materials, 480 (2024) 136234. https://doi.org/10.1016/j.jhazmat.2024.136234. D1, IF_{2024}: 11.3; number of independent citations: 2.
2. **Eszter Kása**, Yvette Szabó, Márton Szabados, Zsolt Kása, Zoltán Kónya, Ákos Kukovecz, Pál Sipos, Bence Kutus, *The neutralization of tricalcium aluminate hexahydrate and its spontaneous transformation into Friedel's salt, a layered double hydroxide*. Cement And Concrete Research, 177 (2024) 107414. https://doi.org/10.1016/j.cemconres.2023.107414. D1, IF_{2024}: 13.1; number of independent citations: 5.
3. **Eszter Kása**, Kornélia Baán, Zsolt Kása, Zoltán Kónya, Ákos Kukovecz, István Pálinkó, Pál Sipos, Márton Szabados, *The effect of mechanical and thermal treatments on the dissolution kinetics of kaolinite in alkaline sodium aluminate solution under conditions typical to Bayer desilication.* Applied Clay Science, 229 (2022) 106671. https://doi.org/10.1016/j.clay.2022.106671. Q1, IF_{2024}: 5.8; number of independent citations: 5.
4. **Eszter Kása**, Márton Szabados, Kornélia Baán, Zoltán Kónya, Ákos Kukovecz, Bence Kutus, István Pálinkó, Pál Sipos, *The dissolution kinetics of raw and mechanochemically treated kaolinites in industrial spent liquor – The effect of the physico-chemical properties of the solids*. Applied Clay Science, 203 (2021) 105994. https://doi.org/10.1016/j.clay.2021.105994. Q1, IF_{2024}: 5.8; number of independent citations: 9.

Related research ΣIF=36.0

Publications not directly related to the PhD dissertation:

1. Zsolt Kása, Enikő Bárdos, **Eszter Kása**, Tamás Gyulavári, Lucian Baia, Zsolt Pap, Klara Hernadi, *Myth or reality? A disquisition concerning the photostability of bismuth-based photocatalysts.* Journal of Environmental Chemical Engineering, 10 (2022) 107624. https://doi.org/10.1016/j.jece.2022.107624. Q1, IF_{2024}: 7.2; number of independent citations: 3.
2. Zsolt Kása, **Eszter Orbán**, Zsolt Pap, Imre Ábrahám, Klára Magyari, Seema Garg, Klara Hernadi, *Innovative and Cost-Efficient BiOI Immobilization Technique on Ceramic Paper—Total Coverage and High Photocatalytic Activity*. Nanomaterials, 10 (2020) 1959. https://doi.org/10.3390/nano10101959. Q1, IF_{2024}: 4.3; number of independent citations: 13.
3. Bence Kutus, Csilla Dudás, **Eszter Orbán**, Alexandru Lupan, Amr AA Attia, István Pálinkó, Pál Sipos, Gábor Peintler, *Magnesium(II) d-Gluconate Complexes Relevant to Radioactive Waste Disposals: Metal-Ion-Induced Ligand Deprotonation or Ligand-*

Promoted Metal-Ion Hydrolysis? Inorganic Chemistry, 58 (2019) 6832. https://doi.org/10.1021/acs.inorgchem.9b00289. D1 (Inorganic Chemistry)/Q1 (Chemistry), IF_{2024}: 4.7; number of independent citations: 7.

4. Lucian Baia, **Eszter Orbán**, et al., *Preparation of TiO2/WO3 composite photocatalysts by the adjustment of the semiconductors' surface charge*. Materials Science In Semiconductor Processing, 42 (2016) 66. https://doi.org/10.1016/j.mssp.2015.08.042. Q2, IF_{2024}: 4.6; number of independent citations: 38.

Not related research ΣIF=20.8

ΣΣIF=56.8

Conference proceedings:

1. **Eszter Kása**, Yvette Szabó, Judit Papp, Márton Szabados, Bence Kutus, Pál Sipos, *Synthesis, characterization and dissolution of bauxite residue (BxR) components relevant to acid neutralization - overview on a bottom-up study conducted at University of Szeged.* Conference Proceedings of the 12th International Alumina Quality Workshop, 2024.
2. Zsolt Kása, **Eszter Orbán**, Zsolt Pap, Imre Ábrahám, Mohit Yadav, Seema Garg, Klara Hernadi, *Effect of the different BiOI immobilization technique on the coverage of ceramic paper and the photocatalytic activity*. Progressive Trends in Coordination, Bioinorganic and Applied Inorganic Chemistry: Monograph Series of the International Conferences on Coordination and Bioinorganic Chemistry, 2019.
3. **Eszter Orbán**, Márton Szabados, Bence Kutus, István Pálinkó, Pál Sipos, *Comparison of kaolinites from different sources*. Progressive Trends in Coordination, Bioinorganic and Applied Inorganic Chemistry: Monograph Series of the International Conferences on Coordination and Bioinorganic Chemistry, 2019.

Conference participations related to the PhD dissertation:

E. Kása, I. Petri, M. Szabados, B. Kutus, P. Sipos, Modified sodalite with O-type additives for efficient removal of basic fuchsine dye from aqueous solutions, 18th European Student Colloid Conference, Szeged, 2022.

E. Kása, M. Szabados, B. Kutus, P. Sipos, Neutralization of tricalcium aluminate hydrates with hydrochloric acid, 20th International Symposium on Solubility Phenomena and Related Equilibrium Processes, Instituto Politécnico de Bragança, Portugália, 2022.

E. Kása, B. Kutus, P. Sipos, The synthesis and neutralization of hydroxysodalite, 28th International Symposium on Analytical and Environmental Problems, Szeged, 2022.

Kása E., Szabó Y., Szabados M., Kutus B., N. Bellahsen, Sipos P., A trikalcium-aluminát előállítása ipari körülmények között és semlegesítési folyamatainak feltérképezése, 55. Komplexkémiai Kollokvium, Debrecen, 2022.

E. Kása, M. Szabados, P. Sipos, Mechanochemical activation of kaolinite to manipulate the dissolution kinetics of the solid, 27th International Symposium on Analytical and Environmental Problems, Szeged, 2021.

E. Kása, Zs. Kása, M. Szabados, P. Sipos, Neutralization of tricalcium aluminate with various acids, Interdisciplinary Doctoral Conference, Pécs, 2021.

All conference participations:

Co-author of 15 lectures presented in international and Hungarian conferences.

Co-author of 7 posters presented in international conferences.

11. AKNOWLEDGEMENTS

First, I need to express my gratitude to my supervisors, Prof. Dr. Pál Sipos, Dr. Márton Szabados Dr. Bence Kutus, who provided me the opportunity to work in the research group since 2017 and always found time to help me through the bumps on the road. I also wish to thank Prof. Dr. István Pálinkó, who is not part of our life anymore, for supervising my work and being there for me regarding every problem as a student.

Many thanks for EGA for the financial and material support and for the industrial and environmental insights. Thanks to them, my work was not only a theoretical study, but it also had industrial connections and real-life goals.

I must express my gratitude also for Dr. Zoltán Kónya and Dr. Ákos Kukovecz for giving us the opportunity to use many of the measuring equipment. I cannot thank enough to Dr. András Stirling for the theoretical calculations and modelling. I am grateful to everyone who helped this work with analytical instrumental measurements, and to Ilona Halasiné Varga for the help during the laboratory work and to every member of the Materials and Solution Structure Research group who helped me during my work.

Many thanks to my family and friends, for always supporting me in hard times. Finally, I wish to thank my husband, Zsolt Kása for the emotional support, the constant motivation and encouragement. He was my muse. This dissertation would have never been born without you.

12. SUPPLEMENTARY INFORMATION

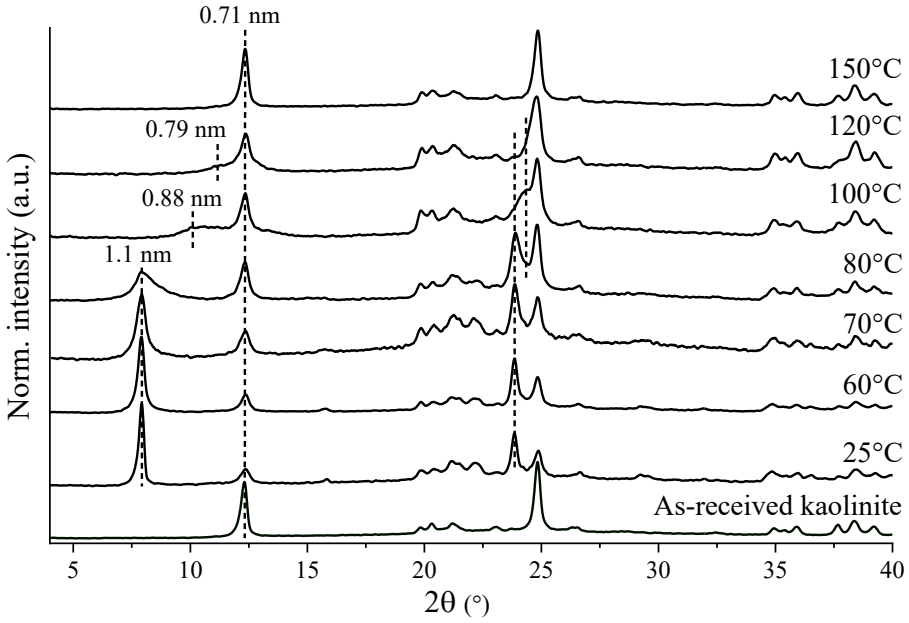

SI. 1 Powder XRD traces of the as received and DMSO intercalated kaolinites, latters dried at various temperatures for 2 h after the intercalation procedure. The 1.10 nm basal distance is the indirect proof of the successful DMSO intercalation, according to literature. Symbols show new phases forming upon neutralization. Measured data were normalized such that the highest value is unity [111].

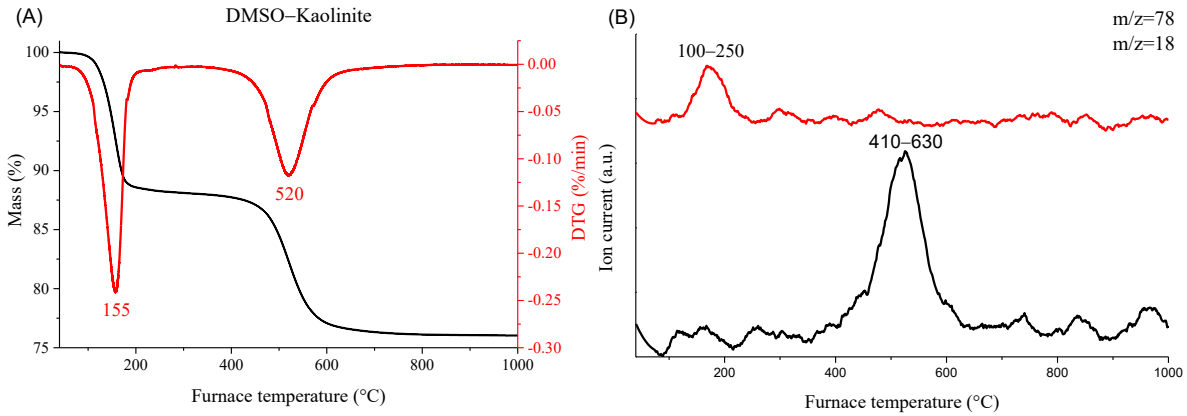

SI. 2 Thermogravimetric curves (A) and mass spectroscopy signals (B) of the DMSO intercalated kaolinite sample. The DMSO departure is visible at 520°C with m/z = 78 [111].

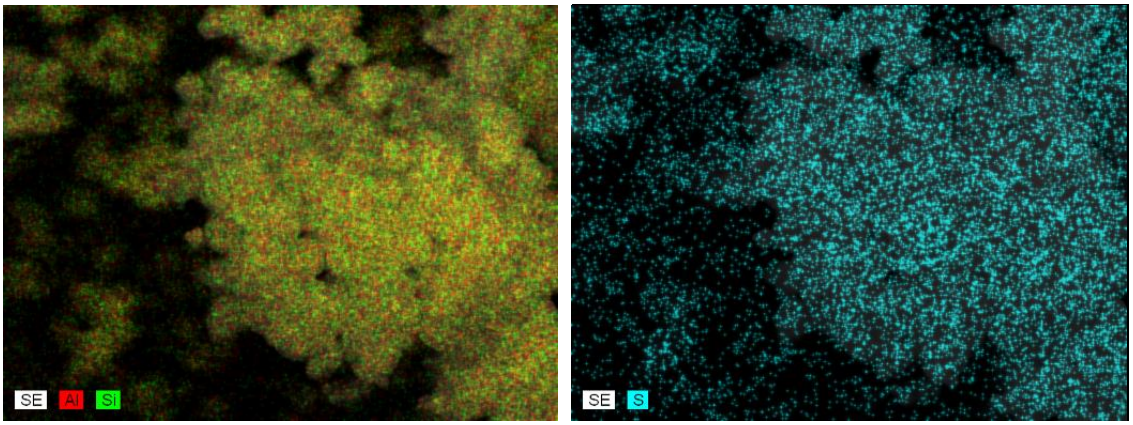

SI. 3 SEM images and the corresponding elemental distribution maps of the energy dispersive X-ray analysis of the sodalites synthesised from the DMSO intercalated kaolinites, proving that the DMSO is part of the final product (in some form) [111].

SI. 4 Specific surface area (SSA), average pore diamater (d_{pore}), and total carbon (TC) content for sodalites synthesized in the absence or presence of different organic additives [124].

Sample name	Additive type	SSA / m^2 g^{-1}	d_{pore} / nm	TC / mg g^{-1}
SOD	no additive	20	7.8	3.76
Sorb	sugar-type	15		5.4
Man	sugar-type	12	9.5	
Fruc	sugar-type	7		4.10
Suc	sugar-type	18		
Gluc	sugar-type	8		3.23
Hpgl	sugar-type	18	7.9	4.00
CTAB	cationic surfactant	9	10.9	22.8 25.5
HDPCl	cationic surfactant	2		113
BACl	cationic surfactant	5	10.2	8.13
SDS	anionic surfactant	9		7.7
SDBS	anionic surfactant	4		34
SDSS	anionic surfactant	20	9.3	8.7
SPAC	anionic surfactant	9	8.1	
TrX100	non-ionic	17	8.3	
PVP	non-ionic	7		76.71 94
PEG	non-ionic	18	7.7	
DMSO	non-ionic	18		3.88

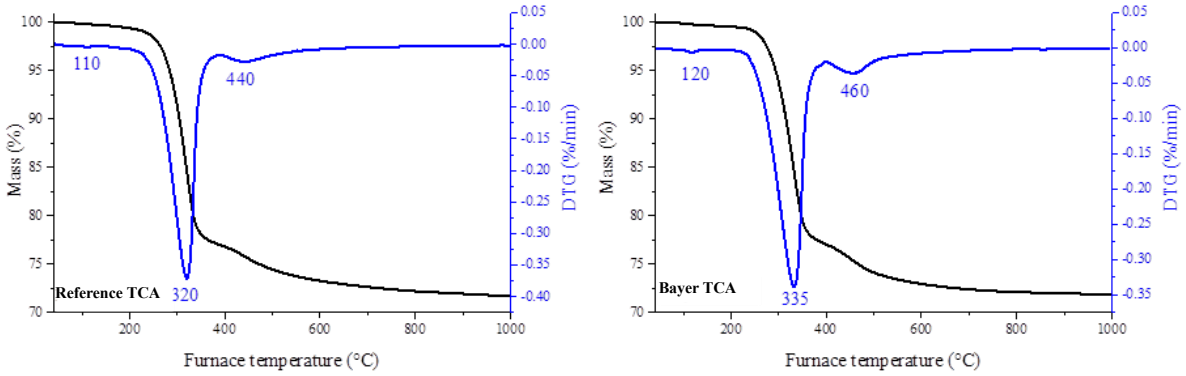

SI. 5 Thermogravimetric analyses of the two tricalcium aluminate hydrates with their characteristic weight losses [134].

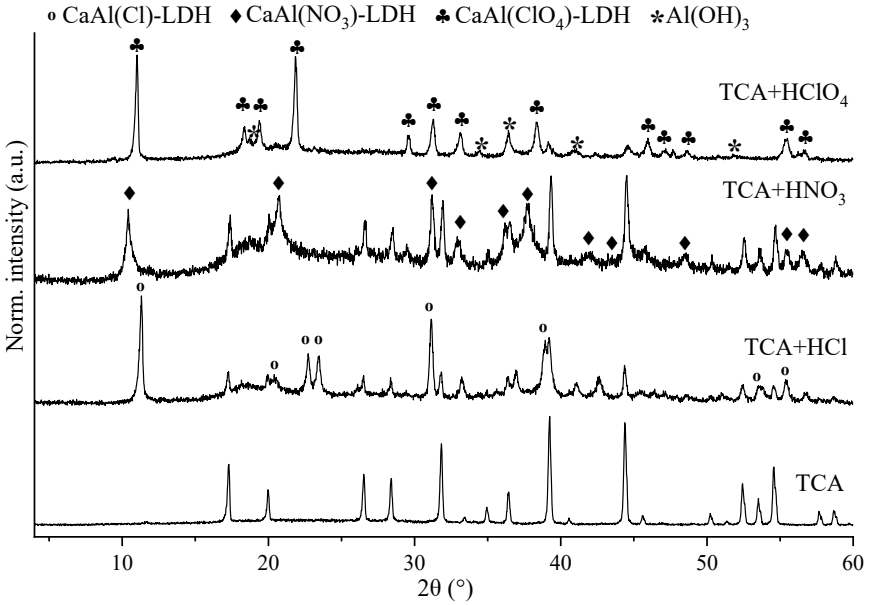

SI. 6 Powder XRD traces of the Bayer TCA after the addition of different acids in H_2O. Symbols show new phases forming upon neutralization. Measured data were normalized such that the highest value is unity [134].